

# 1

## Introduction

### 1.1 Evidence for Dark Matter

Today, the amount of evidence in support of dark matter's existence is overwhelming. This evidence comes from astrophysical and cosmological observations that are inconsistent with a universe composed entirely of visible matter. This section reviews this evidence.

#### 1.1.1 Astrophysical Observations

##### Galaxy Clusters

Some of the first hints for the existence of dark matter came from observations of galaxy clusters. Perhaps the most famous analysis was performed by Fritz Zwicky [1], who was puzzled by the high rotational velocities of galaxies within the Coma Cluster. By applying the virial theorem, equating the cluster's kinetic and gravitational potential energies, he found that the cluster would need to contain a much more significant amount of *dunkle materie* (dark matter) than visible matter to accommodate these high velocities.

##### Rotation Curves of Spiral Galaxies

The anomalous rotational velocities observed in galaxy clusters can also be observed at the galactic scale. The rotation curves of spiral galaxies, which relate

the rotational velocities of stars to their distance from the galactic centre, were observed to be flat at large distances. From the observed distribution of visible matter, Newtonian mechanics predicts that the orbital velocity of a star a distance  $r$  from the galactic centre,  $v_*(r)$ , is related to the mass contained within a radius  $r$ ,  $M(r)$ , through

$$v_*(r) = \sqrt{\frac{GM(r)}{r}}, \quad (1.1)$$

indicating that the velocity should fall off as  $1/\sqrt{r}$  at the outer regions of the galaxy where  $M(r)$  is constant. Instead, observations of many spiral galaxies indicate that this velocity remains constant out to the galaxy's edge.

A simple way to produce such a rotation curve is to introduce a spherically symmetric distribution of dark matter surrounding the galaxy,

$$\rho_{\text{DM}}(r) = \frac{v_0^2}{4\pi G r^2}, \quad (1.2)$$

which results in a constant rotational velocity of  $v_0$  out to the galaxy edge. Detailed simulations of structure formation in a Cold Dark Matter (CDM) Universe indicate that the true distribution is better represented by distribution functions such as the Navaro-Frenk-White (NFW) profile [2, 3] or Einasto [4] profiles, which are commonly used in the literature.

An example rotation curve for galaxy NGC 6503 is presented in Fig. 1.1, with the contributions from each of the matter components to the rotational velocity shown [5, 6]. As can be seen, the visible matter constituting disk and gas components does not explain the observed rotational velocity.

## Gravitational Lensing

As described by General Relativity, the curvature of space-time around massive entities causes light to travel along curved paths. As such, the mass of astrophysical structures can be deduced from the extent to which they distort the images of objects in the background. The extent of the distortions depends on how massive the foreground object is, ranging from the shearing of the background image (weak lensing), to multiple copies of the background object appearing (strong lensing) [7]. The disparity between the mass obtained from gravitational lensing and the mass of visible matter in the system is further evidence of dark matter's existence [8, 9].

## The Bullet Cluster

Galaxy cluster 1E 0657-56, commonly referred to as the “bullet cluster”, was formed by the collision of two separate galaxy clusters. The baryonic matter in these

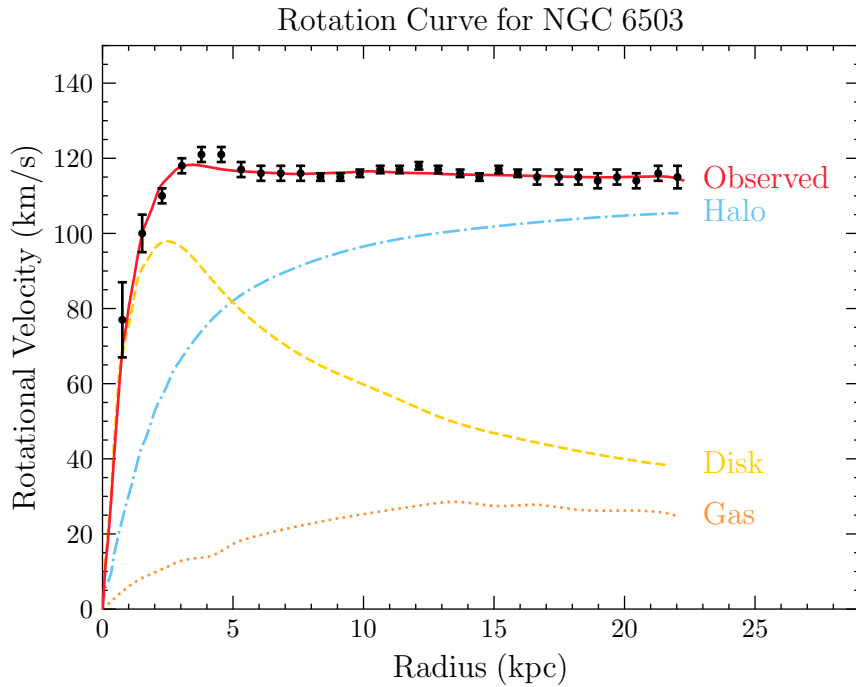


**Figure 1.1:** Galaxy rotation curve for NGC 6503, showing the contributions to the total velocity (red) from the DM halo (blue), disk (yellow), and gas components. Data used in making this plot was obtained from [5, 6].

clusters is mostly composed of a strongly interacting gas and, as expected, produced a significant amount of X-rays during the collision. These X-rays were imaged by the Chandra X-Ray telescope [10], providing information on the resulting distribution of the visible matter. This is shown by the red regions of Fig. 1.2, where it can be seen how the visible matter has been smeared due to the collision. However, when the gravitational potential was mapped using gravitational lensing, it was clear that the majority of the mass was displaced relative to the visible matter. This mass is attributed to the dark matter components of the original clusters. As indicated by the purple regions in Fig. 1.2, the dark matter halos seem to have passed through each other mostly unperturbed. This tells us that not only is the majority of the mass comprised of dark matter, but that the dark matter has extremely weak interactions with both the visible matter and itself.

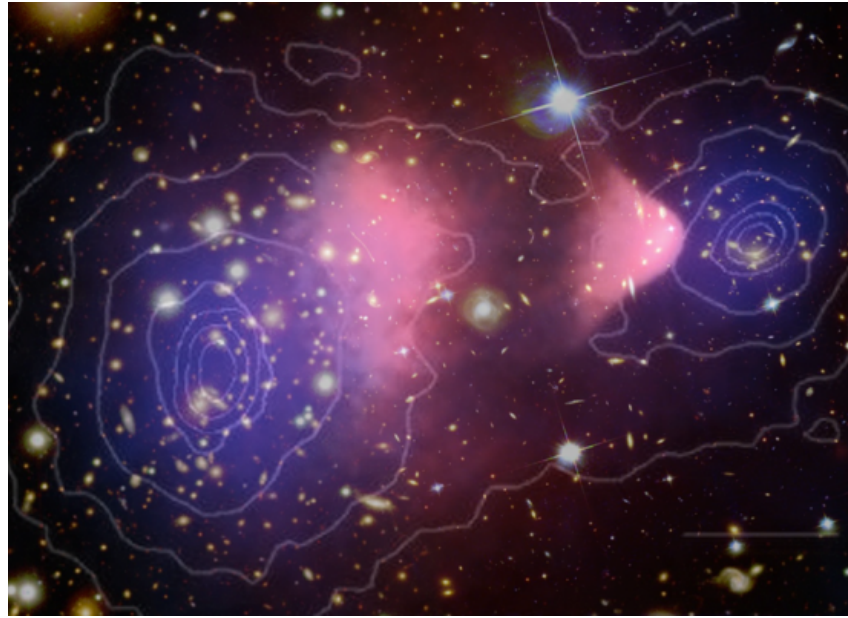


**Figure 1.2:** Image of the Bullet Cluster with contours of the gravitational potential superposed. The red regions indicate the baryonic matter after the collision, while the purple regions are the expected DM components deduced from gravitational lensing. [10, 11]

### 1.1.2 Cosmological Evidence

The current best cosmological model is the  $\Lambda$ -Cold Dark Matter model ( $\Lambda$ CDM), in which  $\Lambda$  refers to the cosmological constant associated with dark energy, and as the name suggests, cold (i.e. non-relativistic) dark matter plays a prominent role. The key components of this model are the aforementioned dark energy and dark matter, along with baryonic matter, and it assumes that gravity is described by Einstein's General Relativity. The total energy density of the universe,  $\rho_{\text{Univ.}}$ , can be broken down into three components based on how their density redshifts with the expansion of the Universe. In the  $\Lambda$ CDM model, these components are matter, radiation, and the vacuum energy  $\Lambda$ . The cosmological abundances of each component, ( $\Omega_m$ ,  $\Omega_r$ ,  $\Omega_\Lambda$  respectively), are expressed as a fraction of the critical density,  $\rho_{\text{crit}}$ ,

$$\rho_{\text{crit}} = \frac{H^2}{8\pi G_N}, \quad (1.3)$$

$$\Omega_i = \frac{\rho_i}{\rho_{\text{crit}}}, \quad (1.4)$$

where  $H$  is the Hubble parameter, such that the total energy density of the Universe satisfies

$$\Omega_m + \Omega_r + \Omega_\Lambda = \frac{\rho_{\text{Univ.}}}{\rho_{\text{crit}}}.$$
 (1.5)

The ratio  $\rho_{\text{Univ.}}/\rho_{\text{crit}}$  determines the curvature of the universe, with values greater than 1 corresponding to a closed universe, less than 1 to an open universe, and equal to 1 to a spatially flat universe. Current observations are consistent with a spatially flat universe, and so we have  $\sum_i \Omega_i = 1$ .

The  $\Lambda$ CDM model has seen huge success as it provides explanations for observed the power spectrum of the Cosmic Microwave Background (CMB), the large-scale structure of the Universe, the abundances of light elements (hydrogen, deuterium, helium, and lithium), and the accelerated expansion rate of the Universe. These observations constrain the parameters of the model and hence provide a complementary probe of the properties of dark matter to the astronomical observations discussed above.

## The Cosmic Microwave Background

One of the strongest probes of cosmological models is the Cosmic Microwave Background (CMB), relic photons from the time epoch of last scattering. This occurred after recombination, at a temperature of around  $\sim 3000$  K, once the photons had decoupled from the baryonic matter and could freely propagate through the universe. The photons observed today have been redshifted by the expansion of the Universe and are well described by a blackbody spectrum with a temperature of  $T_{\text{CMB}} = 2.73 \pm 0.0006$  K. Observations of the CMB temperature reveal that it is not exactly isotropic, with anisotropies at the level of  $\delta T_{\text{CMB}}/T_{\text{CMB}} \sim 10^{-5} - 10^{-6}$  seen on a range of angular scales in the sky. These anisotropies were seeded by the primordial density perturbations that arise during inflation. These perturbations evolve due to the acoustic oscillations of the photon-baryon plasma driven by the interplay between the pressure from the photons and the gravitational attraction of the matter. The oscillations cease once the photons decouple, freezing in their temporal phases that are observed as peaks in the angular power spectrum of the temperature anisotropies.

Measurements of the CMB power spectrum provide information on many of the cosmological parameters. The locations of the acoustic peaks depend on the spatial geometry of the Universe and hence constrains  $\Omega_{\text{tot}}$ . The total matter density,  $\Omega_m$ , affects how the CMB spectrum is gravitationally lensed. The relative amplitudes of the peaks probe the baryon-to-photon ratio and hence the baryon density,  $\Omega_b$ . Finally, the density of dark matter,  $\Omega_{\text{DM}}$ , is obtained by fitting the cosmological parameters to the exact shape of the spectrum [5, 12].

The Planck collaboration most recently performed a precise measurement of the CMB power spectrum in 2018, obtaining best-fit parameters [12, 13]

$$\Omega_m = 0.311 \pm 0.006, \quad \Omega_\Lambda = 0.689 \pm 0.006, \quad (1.6)$$

for the matter and dark energy densities. They obtained a total energy density of  $\Omega_{\text{tot}} = 1.011 \pm 0.006$  at 68% confidence level, providing strong evidence for a spatially flat Universe. The breakdown of the matter density into the dark and baryonic components is determined by combining the CMB results with constraints from Big Bang Nucleosynthesis (BBN)<sup>1</sup> giving

$$\Omega_{\text{DM}} h^2 = 0.1193 \pm 0.0009, \quad \Omega_b h^2 = 0.02242 \pm 0.00014, \quad (1.7)$$

where  $h$  is the dimensionless Hubble constant such that the Hubble parameter today is  $H_0 = 100 h \text{ km s}^{-1} \text{ Mpc}$ .

### Large Scale Structure

After recombination, the pressure on the baryonic matter from photons began to decrease, eventually allowing the small density perturbations to grow. This led to the growth of stars, galaxies, and the large-scale structure we observe today [14]. N-body simulations of the Universe's evolution require a cold dark matter component for this structure to form. While a small component of the dark matter can be warm, hot dark matter would wash out small-scale structures [15].

## 1.2 Potential Models of Dark Matter

Given that baryonic matter is composed of particles described by the Standard Model (SM) of particle physics, it is a fair assumption that dark matter will also have a particle nature. Therefore, models of particle dark matter are built by extending the SM in a way consistent with its symmetries. Such models may be as simple as introducing a single new field into the SM, or there may be a more extensive hidden sector with a complicated symmetry structure. Additionally, there are compelling theories in which dark matter is not a fundamental particle, such as primordial black holes (PBHs) formed in the early universe. Given the few details we know about dark matter, there exists an enormous library of viable dark matter candidates. However, there are generic properties a good dark matter candidate must satisfy, namely:

---

<sup>1</sup>BBN is the process that produced the light elements ( $D$ ,  $^3\text{He}$ ,  $^4\text{He}$ , and  $^7\text{Li}$ ) were produced in the early universe. This process is highly sensitive to the physical condition of the universe at that time, allowing for strong constraints to be placed on physics beyond the Standard Model.

- **Stable on Cosmological Timescales:** Dark matter must either be stable or have a lifetime significantly longer than the age of the Universe to be present in its current abundance.
- **Neutral or milli-charged under Electromagnetism:** Dark matter, as its name suggests, does not significantly interact with light. Requiring that dark matter be completely decoupled from the Standard Model plasma by the time of recombination yields an upper bound on the electric charge of dark matter [16]

$$q_{\text{DM}}/e < \begin{cases} 3.5 \times 10^{-7} \left(\frac{m_{\text{DM}}}{1 \text{ GeV}}\right)^{0.58}, & m_{\text{DM}} > 1 \text{ GeV} \\ 4.0 \times 10^{-7} \left(\frac{m_{\text{DM}}}{1 \text{ GeV}}\right)^{0.35}, & m_{\text{DM}} < 1 \text{ GeV} \end{cases} \quad (1.8)$$

- **Small Self-Interactions:** The standard  $\Lambda$ CDM cosmology assumes that the dark matter is collisionless. However, small dark matter self-interactions can help resolve existing small-scale structure issues [17, 18]. Current limits on the self-interaction cross-section are  $\sigma_{\text{DM-DM}}/m_{\text{DM}} < 0.48 \text{ cm}^2/\text{g}$  come from merging galaxy clusters [11] and the ellipticity of galaxies obtained from X-ray observations [19].
- **Cold:** Dark matter is required to be non-relativistic at the time of structure formation. At most, a small component of the dark matter can be warm (semi-relativistic).

A selection of the more prominent dark matter candidates is shown in Fig. 1.3. The key features of a few of these models are discussed below.

## WIMPs

Weakly Interacting Massive Particles (WIMPs) are a class of dark matter candidates that generically have masses and interaction strengths around the weak scale. Many extensions of the SM naturally predict the existence of such a particle, with famous examples being the lightest supersymmetric particle in supersymmetric theories [21], or the lightest stable Kaluza-Klein mode in theories with extra dimensions [22].

Nowadays, WIMP dark matter is used almost synonymously to mean thermal relic, referring to a species whose relic abundance is produced thermally in the early universe through the freeze-out mechanism [23]. In this paradigm, the WIMP is initially in thermal equilibrium with the Standard Model bath. This equilibrium is maintained as long as the interaction rates of the WIMP with the bath, denoted  $\Gamma$ , remain faster than the Hubble expansion of the universe,  $H$ . As the universe continues to expand, the temperature of the bath drops, slowing down the interaction

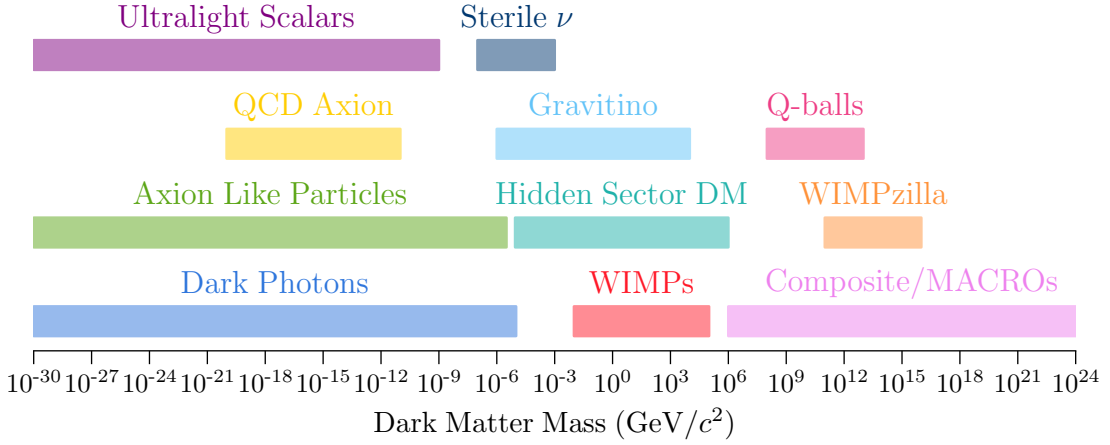


**Figure 1.3:** Illustrative landscape of dark matter models and the mass range for which they predict a valid candidate. Details can be found in the Dark Matter chapter of the PDG [20].

rates. Eventually, the expansion rate overtakes the interaction rates,  $\Gamma/H \lesssim 1$ , and the interactions “freeze out” causing the WIMP to fall out of equilibrium with the bath. At this point, the WIMPs can no longer efficiently annihilate, and their abundance gets “frozen-in” to the value it had at freeze-out, leading to the abundance observed today.

A cold thermal relic, such as dark matter, will freeze out after it has become non-relativistic. In this scenario, the interaction rates become Boltzmann suppressed<sup>2</sup>, and the species rapidly freezes out. The relic density is therefore sensitive to the annihilation cross-section of the species,  $\langle\sigma_{\text{ann}}v\rangle$ . More efficient annihilations correspond to larger cross-sections, resulting in the species remaining in equilibrium for longer times. This allows the number density to continue following the exponentially decreasing Boltzmann distribution and yield a smaller relic abundance. The evolution of the abundance of a Majorana fermion WIMP of mass  $m_{\text{WIMP}} = 100 \text{ GeV}$  is shown in Fig. 1.4 for three values of the annihilation cross-section. A simple expression relating the annihilation cross-section and the

<sup>2</sup>The number density of a non-relativistic species in thermal equilibrium with the bath will follow  $n \propto (m T_{\text{bath}})^{3/2} \exp(-m/T_{\text{bath}})$ . Once the temperature falls below the mass of the species, the number density becomes exponentially suppressed. This is what is known as “Boltzmann suppression”.

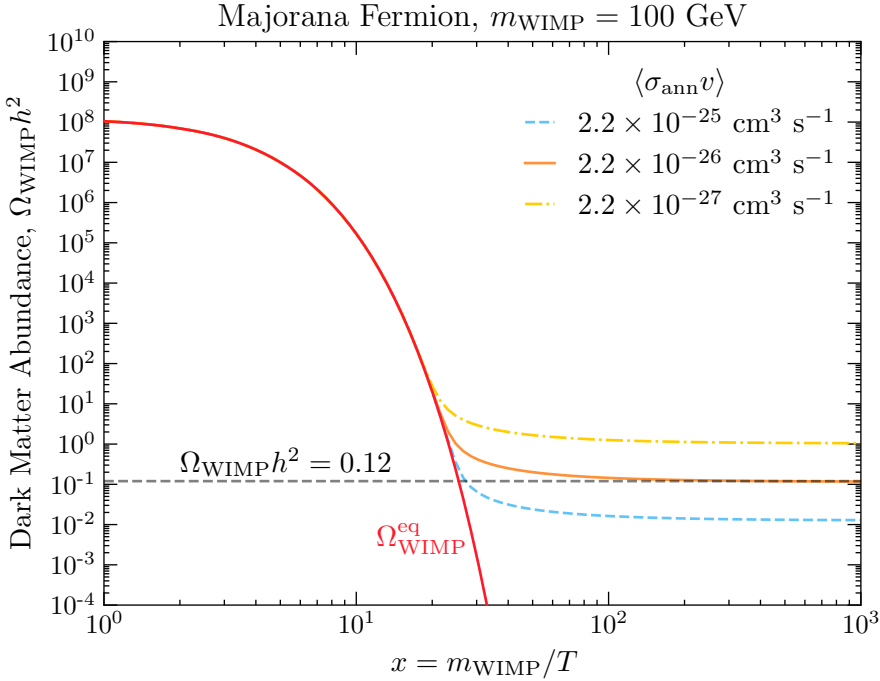


**Figure 1.4:** Evolution of the DM abundance as a function of  $x = m_{\text{DM}}/T$ . The red line tracks the abundance of the WIMP if it remains in equilibrium with the bath. The relic abundance for three different annihilation cross-sections is shown in blue, orange, and yellow for  $\langle \sigma_{\text{ann}} v \rangle = 2.2 \times 10^{-25}$ ,  $2.2 \times 10^{-26}$ , and  $2.2 \times 10^{-27} \text{ cm}^3 \text{s}^{-1}$  respectively.

abundance that is correct to  $\sim 5\%$  can be obtained [24]

$$\Omega_{\text{DM}} h^2 = \frac{10^{-27} \text{ cm}^3 \text{s}^{-1}}{\langle \sigma_{\text{ann}} v_\chi \rangle} \frac{x_*}{g_*^{1/2}} \quad (1.9)$$

$$\sim 0.12 \left( \frac{2.2 \times 10^{-26} \text{ cm}^3 \text{s}^{-1}}{\langle \sigma v \rangle} \right), \quad m_\chi \gtrsim 10 \text{ GeV}, \quad (1.10)$$

where  $x_* = m_{\text{WIMP}}/T_*$  is evaluated at an intermediate temperature between equilibrium and freeze-out, with  $g_*$  the effective number of relativistic degrees of freedom present at this time.

The allowed mass range for a thermal WIMP is between  $10 \text{ MeV} \lesssim m_{\text{WIMP}} \lesssim 100 \text{ TeV}$ . Lighter WIMPs will make non-negligible contributions to the effective number of neutrinos at the time of Big Bang Nucleosynthesis, measured to be  $N_{\text{eff}}^{\text{BBN}} = 3.044$  [25], altering the observed abundances of the light elements. The CMB offers an additional probe of  $N_{\text{eff}}$  at the later time of recombination and can be combined with the BBN result leading to the value  $N_{\text{eff}} = 2.99 \pm 0.17$  [12].

Given the Standard Model predicts a value of  $N_{\text{eff}} = 3.044$ , contributions from additional relativistic degrees of freedom must be less than  $\Delta N_{\text{eff}} < 0.28$  [25]. At the high end of this range, masses larger than  $\sim 100 \text{ TeV}$  are excluded from partial wave unitarity [26].

## Axions

The axion originally arose from the Peccei-Quinn solution to the Strong CP problem. This refers to the lack of observed CP-violation in the QCD sector of the Standard Model that arises from the topological term in the Lagrangian

$$\mathcal{L}_{\theta_{\text{QCD}}} = \frac{g_s^2}{32\pi} \theta_{\text{QCD}} G_{\mu\nu} \tilde{G}^{\mu\nu}, \quad (1.11)$$

where  $g_s$  is the QCD coupling constant,  $G_{\mu\nu}$  is the gluon field strength tensor and  $\tilde{G}^{\mu\nu}$  is its dual. This term generates an electric dipole moment for the neutron (nEDM) that has yet to be observed experimentally. The current upper bound on the nEDM is  $|d_n| < 0.18 \times 10^{-26} \text{ e cm}$  [27] and can be translated to an upper bound on the CP-violating QCD  $\theta$ -parameter such that  $|\theta_{\text{QCD}}| \lesssim 10^{-10}$ , raising questions as to why this value seems to be fine-tuned to such a small value.

The Peccei-Quinn solution to this problem introduces a new, anomalous, global  $U(1)_{\text{PQ}}$  symmetry and promotes  $\theta_{\text{QCD}}$  to be a dynamical field. Wilczek [28] and Weinberg [29] showed that the axion emerges as the pseudo-Goldstone boson associated with the breaking of  $U(1)_{\text{PQ}}$ . Though the original axion was quickly out, many modern extensions of the SM predict the existence of a QCD axion. Two of the most prominent UV completions of the axion are the KSVZ [30, 31] and DFSZ [32, 33] models. In these models, the axion produced in the early Universe can serve the role of cold dark matter today. This makes it a very compelling dark matter candidate, as it solves two of the biggest mysteries of physics in one neat package.

However, solving the Strong CP problem can be rather restrictive on the model parameters. For example, the QCD axion's coupling to the photon,  $g_{a\gamma\gamma}$ , is not a free parameter and depends on the scale at which the PQ symmetry is broken. Many models introduce a light pseudoscalar particle, say  $a$ , that couples to the photon in the same way as the QCD axion,

$$\mathcal{L}_{a\gamma\gamma} = -\frac{g_{a\gamma\gamma}}{4} a F_{\mu\nu} \tilde{F}^{\mu\nu}, \quad (1.12)$$

but is not associated with a solution to the Strong CP problem. Such pseudoscalars are known as “Axion Like Particles” (ALPs) and can make a good dark matter candidate.

## Primordial Black Holes

Primordial black holes (PBHs) are formed during the early Universe through various mechanisms. The simplest mechanism predicts that PBHs are produced from the gravitational collapse of superhorizon density fluctuations seeded during inflation [34–36]. Unlike black holes that originate from stellar collapse, which have masses  $\gtrsim 3M_\odot$ , the mass of a PBH can be arbitrary. PBHs can also make a good dark matter candidate, satisfying all the criteria points outlined above. In fact, PBHs with a mass between  $\sim (10^{-17} - 10^{-12}) M_\odot$ , dubbed “asteroid mass PBHs”, can account for 100% of the dark matter content in the Universe [37]. Outside this range, PBHs can still make up a small fraction of dark matter [38].

### 1.2.1 Dark Matter in an Effective Field Theory Framework

For a dark matter candidate to be truly compelling, it should be able to be embedded into an ultraviolet (UV) complete theory. Such theories are renormalisable<sup>3</sup> and gauge invariant under the SM gauge group  $SU(3)_{\text{colour}} \otimes SU(2)_L \otimes U(1)_Y$ . This allows them to be predictive up to arbitrarily high energies. These theories are typically quite complex, requiring the introduction of multiple new fields and many more free parameters. As an example, consider the phenomenological Minimal Supersymmetric Standard Model (pMSSM) [38] in which the lightest neutralino<sup>4</sup> can be a thermal WIMP dark matter candidate. In this theory, 19 free parameters are introduced on top of the free parameters in the SM, requiring 38 independent experimental observations to fully constrain the model. Given that at this time, all good dark matter candidates are equally likely to be the correct one, a model-independent approach to interpreting experimental results is desirable. This is achieved by describing the interactions of dark matter with the SM through an effective field theory (EFT).

### 1.2.2 Overview of Effective Field Theory

Modern physics can be thought of as a ladder of theories that are designed to describe the physics present at a given energy (or length) scale. For example, Newtonian mechanics is a sufficient description of the physics experienced in our everyday lives. However, in situations where the energy is comparable to the mass of the system, Newtonian mechanics breaks down, and Special Relativity must be

---

<sup>3</sup>In a renormalisable theory, the infinities that arise from UV divergences can be absorbed by fixing a finite number of parameters to experimentally observed values.

<sup>4</sup>The neutralinos are the mass eigenstates of the supersymmetric partners of the neutral gauge bosons and the higgsino.

used to describe the physics. In particle physics, the Standard Model provides an excellent description of particle interactions up to the energies reached at LHC, 13.6 TeV, and perhaps even further beyond. However, even it is expected to break down at higher energy scales, in particular at the Planck scale, where a quantum theory of gravity is required. Hence, both Newtonian mechanics and the SM are low-energy, effective descriptions of a more complete theory.

This philosophy based on only describing the physics relevant below some energy scale,  $\Lambda$ , is the core principle of EFTs. The Lagrangian for the effective theory only contains the degrees of freedom that can be produced below the scale  $\Lambda$ , i.e. fields that have masses less than this scale. This low-energy regime described by the EFT is often called the infrared (IR) regime.

In general, the EFT Lagrangian will contain renormalizable terms,  $\mathcal{L}_{\text{renorm.}}$ , built out of operators that have mass dimension  $\leq 4$ , as well as operators with mass dimension  $n > 4$ ,  $\mathcal{O}_i^{(n)}$ , that encapsulate the contributions from the UV physics. Each of these higher dimensional operators will be suppressed by the scale of new physics,  $\Lambda^{4-n}$ . The effective Lagrangian can then be written as

$$\mathcal{L}_{\text{EFT}} = \mathcal{L}_{\text{renorm.}} + \sum_{n>4} \sum_{i=1}^{j_n} \frac{C_i^{(n)}(\tilde{\mu})}{\Lambda^{n-4}} \mathcal{O}_i^{(n)}, \quad (1.13)$$

where we sum over all  $j_n$  operators present at mass dimension  $n$ . The expansion coefficients,  $C_i^{(n)}$ , are the Wilson coefficients that contain the effects of the UV physics. In general, the Wilson coefficients run with the energy scale they are evaluated at,  $\tilde{\mu}$ , described by the renormalisation group equations (RGEs). The sum over the mass dimension of the operators is typically terminated at some sensible value, as higher dimensional operators get increasingly suppressed by the cutoff scale  $\Lambda$ .

The series of operators in Eq. 1.13 can be constructed in two different ways. First, we assume some prior knowledge of the underlying UV theory. Then, for a given energy scale  $\Lambda$ , the heavy degrees of freedom are known, and can be explicitly integrated out. There are various methods for performing this process, the simplest being expanding the propagator of the heavy fields in powers of the momenta over the heavy mass,  $(p/M)^2$ . For the simple case of a heavy scalar, this corresponds to

$$\frac{i}{p^2 - M^2} = \frac{-i}{M^2} \left( \frac{1}{1 - (p/M)^2} \right) \approx \frac{-i}{M^2} \left( 1 + \left( \frac{p}{M} \right)^2 + \mathcal{O} \left( \left( \frac{p}{M} \right)^4 \right) \right). \quad (1.14)$$

An alternate method is to replace the heavy fields in the Lagrangian with their classical equations of motion. The resulting effective Lagrangian will contain all the operators generated by the UV theory at tree level. Constructing an EFT in this way is called the *top-down* method.

The second method of constructing an EFT is to be agnostic to the UV physics and write down all possible operators that can be constructed from the IR degrees of freedom. These operators must obey the symmetries of the IR theory, as well as any other constraints one wishes to impose<sup>5</sup>. This is the *bottom-up* approach, offering a more model-independent approach than the top-down method. The Wilson coefficients, in this case, will be arbitrary functions of the energy scale determined by solving the RGEs.

In general, the parameter space of the EFT will be lower dimensional than those of the corresponding UV models. This allows for an easier comparison with experimental results, as fewer parameters need to be fit to the data. Once the Wilson coefficients have been constrained at the low energy scale of the experiments, they can be matched to the coefficients generated by some UV theory at another scale, thereby constraining the UV parameters.

### 1.2.3 Dimension 6 EFT Operators for Dirac Fermion Dark Matter

This work will focus on dimension 6 EFT operators that describe the interactions of Dirac fermion dark matter with standard model fermions. These operators will have a structure

$$\mathcal{L}_{\text{EFT}}^{(6)} \sim \frac{1}{\Lambda^2} (\bar{\chi} \Gamma_{\text{DM}} \chi) (\bar{f} \Gamma_{\text{SM}} f), \quad (1.15)$$

where the  $\Gamma_i$  determines the Lorentz structure of the interaction by taking appropriate combinations from the set

$$\Gamma_i \in \{1, i\gamma_5, \gamma^\mu, i\gamma^\mu\gamma^5, \sigma^{\mu\nu}, i\sigma^{\mu\nu}\gamma^5\}. \quad (1.16)$$

For example, the case of  $\Gamma_\chi = \Gamma_{\text{SM}} = 1$  yields scalar currents for both the DM and SM fermions and would correspond to integrating out a heavy scalar mediator in the UV theory. Under the assumption of minimal flavour violation (MFV)<sup>6</sup> are ten such operators at dimension six that form a linearly independent basis. These are given in Table 1.1, along with spin-averaged squared matrix element for dark matter scattering with a fermion. The operators are classified based on the Lorentz nature of the SM fermion bilinear; D1-2: Scalar (S), D3-4: Pseudoscalar (P), D5-6: Vector (V), D7-8: Axial-vector (A), and D9-10: tensor (T). The coupling constant,  $g_f$ , for operators that involve the S and P fermion bilinears (operators D1-4) are

---

<sup>5</sup>For example, one might require that no flavour changing processes are present at dimension 5, despite such operator being allowed by the symmetries.

<sup>6</sup>MFV is the assumption that the only source of flavour violation in the quark sector comes from the SM Yukawa matrices and not from any new physics introduced at a higher scale.

Name	Operator	$g_f$	$ \overline{M}(s, t, m_i) ^2$
D1	$\bar{\chi}\chi \bar{f}f$	$\frac{y_f}{\Lambda_f^2}$	$g_f^2 \frac{(4m_\chi^2 - t)(4m_\chi^2 - \mu^2 t)}{\mu^2}$
D2	$\bar{\chi}\gamma^5\chi \bar{f}f$	$i \frac{y_f}{\Lambda_f^2}$	$g_f^2 \frac{t(\mu^2 t - 4m_\chi^2)}{\mu^2}$
D3	$\bar{\chi}\chi \bar{f}\gamma^5 f$	$i \frac{y_f}{\Lambda_f^2}$	$g_f^2 t (t - 4m_\chi^2)$
D4	$\bar{\chi}\gamma^5\chi \bar{f}\gamma^5 f$	$\frac{y_f}{\Lambda_f^2}$	$g_f^2 t^2$
D5	$\bar{\chi}\gamma_\mu\chi \bar{f}\gamma^\mu f$	$\frac{1}{\Lambda_f^2}$	$2g_f^2 \frac{2(\mu^2 + 1)^2 m_\chi^4 - 4(\mu^2 + 1)\mu^2 s m_\chi^2 + \mu^4(2s^2 + 2st + t^2)}{\mu^4}$
D6	$\bar{\chi}\gamma_\mu\gamma^5\chi \bar{f}\gamma^\mu f$	$\frac{1}{\Lambda_f^2}$	$2g_f^2 \frac{2(\mu^2 - 1)^2 m_\chi^4 - 4\mu^2 m_\chi^2 (\mu^2 s + s + \mu^2 t) + \mu^4(2s^2 + 2st + t^2)}{\mu^4}$
D7	$\bar{\chi}\gamma_\mu\chi \bar{f}\gamma^\mu\gamma^5 f$	$\frac{1}{\Lambda_f^2}$	$2g_f^2 \frac{2(\mu^2 - 1)^2 m_\chi^4 - 4\mu^2 m_\chi^2 (\mu^2 s + s + t) + \mu^4(2s^2 + 2st + t^2)}{\mu^4}$
D8	$\bar{\chi}\gamma_\mu\gamma^5\chi \bar{f}\gamma^\mu\gamma^5 f$	$\frac{1}{\Lambda_f^2}$	$2g_f^2 \frac{2(\mu^4 + 10\mu^2 + 1)m_\chi^4 - 4(\mu^2 + 1)\mu^2 m_\chi^2 (s + t) + \mu^4(2s^2 + 2st + t^2)}{\mu^4}$
D9	$\bar{\chi}\sigma_{\mu\nu}\chi \bar{f}\sigma^{\mu\nu} f$	$\frac{1}{\Lambda_f^2}$	$8g_f^2 \frac{4(\mu^4 + 4\mu^2 + 1)m_\chi^4 - 2(\mu^2 + 1)\mu^2 m_\chi^2 (4s + t) + \mu^4(2s + t)^2}{\mu^4}$
D10	$\bar{\chi}\sigma_{\mu\nu}\gamma^5\chi \bar{f}\sigma^{\mu\nu} f$	$\frac{i}{\Lambda_f^2}$	$8g_f^2 \frac{4(\mu^2 - 1)^2 m_\chi^4 - 2(\mu^2 + 1)\mu^2 m_\chi^2 (4s + t) + \mu^4(2s + t)^2}{\mu^4}$

**Table 1.1:** Dimension 6 EFT operators [39] for the coupling of Dirac DM to fermions (column 2), together with the squared matrix elements DM-fermion scattering (column 5), where  $s$  and  $t$  are Mandelstam variables,  $\mu = m_\chi/m_T$ , and  $m_T$  is the target mass.

normalised by the corresponding Yukawa couplings. This is because, in a UV complete theory, these bilinears would couple to the new scalar/pseudoscalar field that mediates the interactions with the dark matter. In many models, this new field will mix with the SM Higgs field, leading to couplings that depend on the fermion masses. The remaining bilinears have coupling constants that depend only on the cutoff scale,  $\Lambda_f$ .

### 1.2.4 From DM-Quark to DM-Nucleon Interactions

The operators in Table 1.1 describe dark matter interactions at the quark level, as these are the degrees of freedom most models are formulated with. However, we will primarily be interested in dark matter scattering with baryons, which requires taking the matrix element of the quark operators between baryon states, i.e.  $\langle \mathcal{B} | \bar{q} \Gamma_q q | \mathcal{B} \rangle$ . These matrix elements can be calculated through the application of Chiral Perturbation Theory (ChPT), giving a baryon level EFT. The operators of this EFT will have the same form as those in Table 1.1, with the obvious re-

placement of  $f \rightarrow \mathcal{B}$ , as well as additional form factors that take into account the structure of the baryons.

The required form factors for each operator have been calculated at zero momentum transfer in Ref. [40] and are given by

$$c_{\mathcal{B}}^S(0) = \frac{2m_{\mathcal{B}}^2}{v^2} \left[ \sum_{q=u,d,s} f_{T_q}^{(\mathcal{B})} + \frac{2}{9} f_{T_G}^{(\mathcal{B})} \right]^2, \quad (1.17)$$

$$c_{\mathcal{B}}^P(0) = \frac{2m_{\mathcal{B}}^2}{v^2} \left[ \sum_{q=u,d,s} \left( 1 - 3 \frac{\bar{m}}{m_q} \right) \Delta_q^{(\mathcal{B})} \right]^2, \quad (1.18)$$

$$c_{\mathcal{B}}^V(0) = 9, \quad (1.19)$$

$$c_{\mathcal{B}}^A(0) = \left[ \sum_{q=u,d,s} \Delta_q^{(\mathcal{B})} \right]^2, \quad (1.20)$$

$$c_{\mathcal{B}}^T(0) = \left[ \sum_{q=u,d,s} \delta_q^{(\mathcal{B})} \right]^2, \quad (1.21)$$

where  $v = 246$  GeV is the vacuum expectation value of the SM Higgs field,  $\mathcal{B}$  is the baryonic species,  $\bar{m} \equiv (1/m_u + 1/m_d + 1/m_s)^{-1}$  and  $f_{T_q}^{(\mathcal{B})}$ ,  $f_{T_G}^{(\mathcal{B})} = 1 - \sum_{q=u,d,s} f_{T_q}^{(\mathcal{B})}$ ,  $\Delta_q^{(\mathcal{B})}$  and  $\delta_q^{(\mathcal{B})}$  are the hadronic matrix elements, determined either experimentally or by lattice QCD simulations. The specific values of these matrix elements for various baryons are provided in Appendix B.

The assumption of zero-momentum transfer is valid when considering interactions with momentum transfers  $\lesssim 1$  GeV, such as in direct detection experiments. Once the momentum transfer exceeds this, the internal structure of the baryon begins to be resolved, and an additional momentum-dependent form factor is required to account for this [41],

$$F_{\mathcal{B}}(t) = \frac{1}{(1 - t/Q_0^2)^2}, \quad (1.22)$$

where  $t$  is the Mandelstam variable, and  $Q_0$  is an energy scale that depends on the hadronic form factor. For simplicity, we will conservatively take  $Q_0 = 1$  GeV for all operators. Putting everything together, the squared coupling constants for dark matter-baryon interactions are obtained by making the replacement

$$g_f^2 \rightarrow \frac{c_{\mathcal{B}}^I(t)}{\Lambda_q^4} \equiv \frac{1}{\Lambda_q^4} c_{\mathcal{B}}^I(0) F_{\mathcal{B}}^2(t), \quad I \in S, P, V, A, T, \quad (1.23)$$

in the matrix elements in the final column of Table 1.1.

## 1.3 Current Status of Dark Matter Constraints

In broad terms, there are three main ways that we can search for evidence of dark matter, often termed “make it, shake it, or break it”. “Make it” refers to the production of dark matter at colliders; “break it” to dark matter annihilation signals; and “shake it” to dark matter scattering. This section discusses the current status of these detection methods.

### 1.3.1 Collider Bounds

If dark matter is produced in a collider, it will simply leave the detector without depositing any energy. To determine if such an invisible particle was produced, conservation of energy-momentum is used to determine if any events are missing energy. In practice, what is searched for is missing momentum that is transverse to the beamline.

Currently, dark matter has not been observed to be produced in particle colliders. This non-observation has instead been used to constrain the dark matter mass and production cross-sections or couplings of various models. These limits are typically interpreted in a model-dependent manner, as different dark matter - Standard model couplings can significantly alter the production rates.

The ATLAS and CMS experiments at the LHC have performed analyses on various dark matter production mechanisms, including the exchange of a  $Z/Z'$  or Higgs, EFTs and heavy mediators, and mono-jet searches [42]<sup>7</sup>. Collider searches also offer complimentary probes of the dark matter-nucleon scattering cross-Section [43] as they probe the same underlying coupling of dark matter to quarks.

It is important to note that an observation of an invisible massive particle at a collider is not enough to infer that it is dark matter. Such an observation will only tell us that such a particle exists. On its own, it does not determine the abundance of the species or if it is stable in cosmological times. As such, it could be just a sub-component of a larger dark sector. To measure enough of the model parameters and determine these important properties, complimentary observations from direct or indirect detectors are often required.

---

<sup>7</sup>These searches refer to a single jet being produced alongside a pair of dark matter particles. This jet could be of Standard Model or dark sector origin, with the latter commonly referred to as “mono-X” searches.

### 1.3.2 Direct Detection Searches

In colliders, dark matter with mass below the collision energy can be produced as long as it couples to the electroweak or colour sectors of the SM. Direct detection experiments, on the other hand, must employ different experimental techniques to probe different mass ranges. For ALP dark matter that is wavelike, haloscope experiments such as ADMX [44] and MADMAX [45] attempt to convert ALPs to photons via the Primakoff effect. Searches for WIMP-like dark matter look for the dark matter scattering with some detector material, causing it to recoil and deposit energy into the detector. Given that our focus is on WIMP-like dark matter, this section will review the status of these experiments.

The differential rate at which the incoming flux of dark matter will scatter within a detector with  $N_T$  targets, as a function of the recoil energy,  $E_R$ , is given by

$$\frac{dR(E_R, t)}{dE_R} = N_T \frac{\rho_{\text{DM}}}{m_{\text{DM}}} \int_{v > v_{\min}}^{v_{\text{esc}}} v f(\vec{v} + \vec{v}_E) \frac{d\sigma}{dE_R} d^3v, \quad (1.24)$$

and depends on the quantities:

- $v_{\min}$  is the minimum dark matter velocity required by kinematics for a scattering event to occur;
- $v_{\text{esc}} = 528 \text{ km s}^{-1}$  is the Milky Way escape velocity;
- $\vec{v}_E$  is the velocity of the Earth through the dark matter halo<sup>8</sup>;
- $f(\vec{v} - \vec{v}_E)$  is the dark matter velocity distribution in the Earth's frame;
- $d\sigma/dE_R$  is the differential scattering cross-section.

Given the low interaction rate of dark matter, the expected event rate in detectors is very low, around one event per day, per kilogram of target material, per kiloelectronvolt deposited. To contend with such a low event rate, as much of the background noise needs to be reduced as possible. This is achieved by placing the detectors deep underground in laboratories that are naturally shielded from the majority of the cosmic rays incident on the surface.

The particle physics input into the scattering rate is encapsulated within the differential cross-section,  $d\sigma/dE_R$ . It is common to separate the cross-section into contributions from spin-dependent (SD) and spin-independent (SI) interactions such

---

<sup>8</sup>This accounts for the orbit of the Earth around the Sun, which induces an annual modulation in the flux of DM.

that

$$\frac{d\sigma}{dE_R} = \frac{(m_{\text{DM}} + m_T)^2}{m_T m_{\text{DM}}^2 v^2} (\sigma^{\text{SI}} |F_{\text{SI}}(E_R)|^2 + \sigma^{\text{SD}} |F_{\text{SD}}(E_R)|^2), \quad (1.25)$$

$$\sigma^{\text{SI}} \approx \sigma_0^{\text{SI}} A_T^2 \left( \frac{m_T}{m_p} \right)^2 \left( \frac{m_{\text{DM}} + m_p}{m_{\text{DM}} + m_T} \right)^2, \quad (1.26)$$

$$\sigma^{\text{SD}} \approx \sigma_0^{\text{SD}} \left( \frac{4(J_T + 1)}{3J_T} |\langle S_p \rangle + \langle S_n \rangle|^2 \right) \left( \frac{m_T}{m_p} \right)^2 \left( \frac{m_{\text{DM}} + m_p}{m_{\text{DM}} + m_T} \right)^2, \quad (1.27)$$

where  $m_T$ ,  $A_T$ ,  $J_T$  are the target mass, atomic mass number, and atomic spin,  $m_p$  is the mass of the proton,  $\langle S_{p,n} \rangle$  are the expectation values of the protons and neutrons in the nucleus. The  $\sigma_{p,0}^{\text{SI/SD}}$  are reference DM-proton scattering cross-sections evaluated in the zero-momentum transfer limit, with the form factors  $F_{\text{SI/SD}}(E_R)$  depending on the recoil energy accounting for the finite size of the nucleus being probed at high momentum transfer. We have assumed that dark matter interacts the same with neutrons and protons for simplicity.

The SI interactions do not couple to the spin of the target and as such the nuclear cross-section is a coherent sum over all the nucleons. This results in an  $A_T^2$  enhancement compared to the dark matter-nucleon cross-section. Experiments searching for SI interactions take advantage of this by using heavy noble gases as the target material, such as Xenon and Argon. On the other hand, the SD interactions do couple to the spin of the target. As the total cross-section is the sum of all the nucleon contributions, the result is expected to average out to zero unless there is an unpaired nucleon present. Chemicals that contain  $^{19}\text{F}$  are the favourable targets as it contains an unpaired proton.

The current leading constraints on the dark matter-nucleon scattering cross-section are shown in Fig. 1.5, with SI in the top panel and SD in the bottom. The SI limits are set by liquid noble gas experiments (LZ [46], XENON-1T [47], PandaX-II [48], and DarkSide-50 [49]), solid-state cryogenic detectors (CRESST-III [50], CDMSlite [51], with projected DARWIN sensitivities [52]), and room temperature crystals (DAMA/LIBRA [53], and COSINE-100 [54]).

The constraints on the SD dark matter-proton scattering cross-section are shown in the bottom panel of Fig 1.5. Superheated liquid experiments such as the PICO-60 [55] as well as PICASSO [56] provide the leading constraints. These interactions are also constrained by many of the same experiments that focus on SI interactions, as they will inevitably contain isotopes with non-zero spin, such as  $^{129}\text{Xe}$  and  $^{131}\text{Xe}$  in XENONnT.

The orange dashed line represents the neutrino floor<sup>9</sup>, providing a lower limit on the cross-section that can be probed by conventional direct detection experiments. Below this line, detectors will become sensitive to the irreducible background from

---

<sup>9</sup>Calling this the “neutrino fog” rather than floor has been gaining traction in recent years [57]

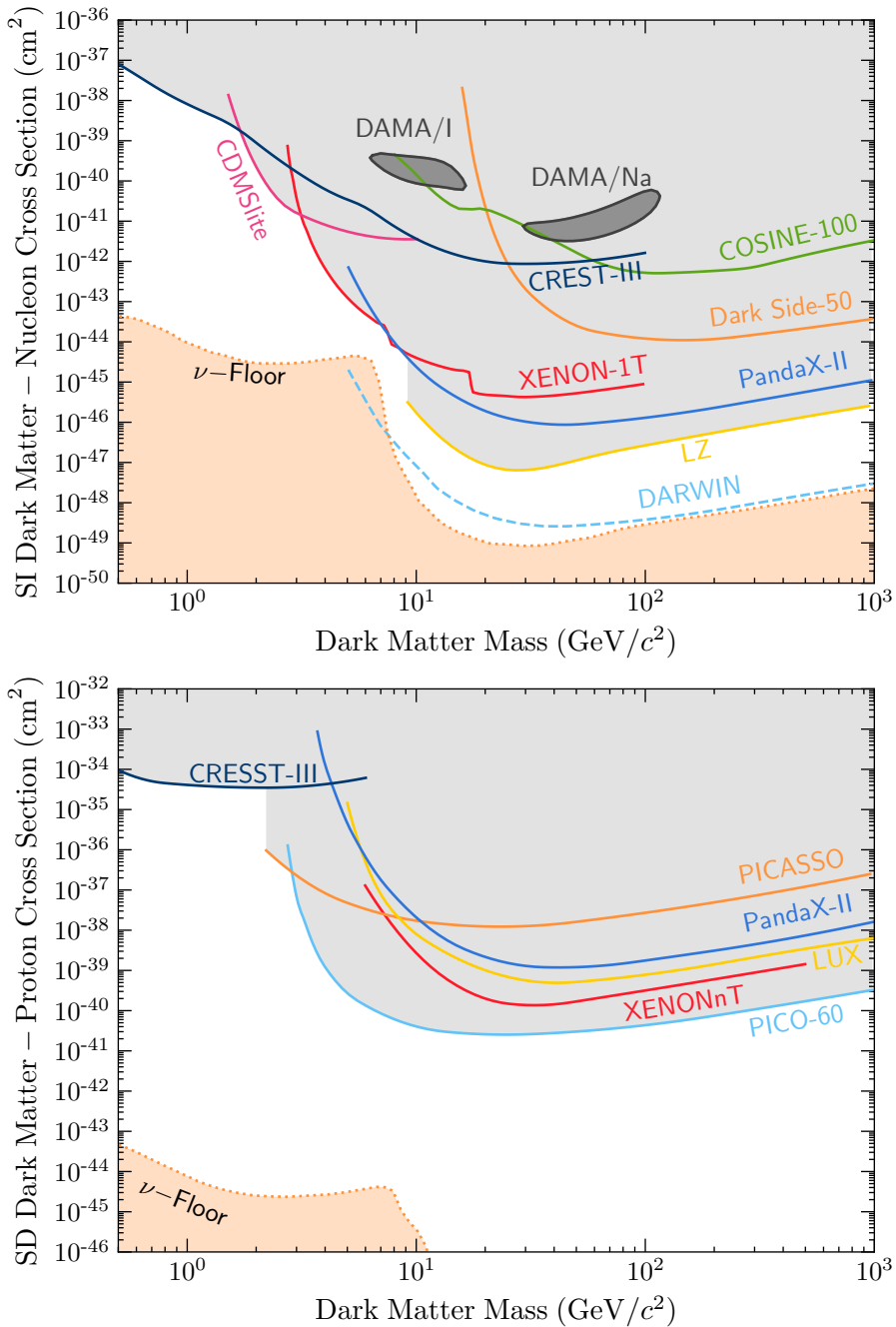


**Figure 1.5:** Current status of direct detection searches for dark matter. **Top:** Spin-independent dark matter-nucleon scattering. **Bottom:** Spin-dependent dark matter-proton scattering. Shaded regions above the coloured lines are excluded. Data was taken from the sources cited in the text.

Coherent Elastic Neutrino-Nucleus Scattering (CE $\nu$ NS). For dark matter masses  $\lesssim 10\text{ GeV}$  the solar neutrino flux is the main background source, while the atmospheric neutrino flux becomes the dominant background for masses  $\gtrsim 20\text{ GeV}$ . A significant amount of effort is being put toward overcoming this limitation, with the main strategy being to take advantage of the directionality of dark matter flux [58]. Such experiments attempt to resolve the direction of the nuclear recoil event, giving information about the direction the incident particle came from. This could allow discrimination between dark matter events, that are expected to be from the direction of the Cygnus constellation, and the background solar and atmospheric neutrinos coming from the Sun and sky respectively.

Many experiments begin to lose sensitivity to low-mass dark matter ( $m_{\text{DM}} \lesssim 10\text{ GeV}$ ) as the recoil energy of the targets falls below the threshold energy resolution of the detector. Current detectors can reach thresholds as low as  $\sim \mathcal{O}(100\text{ eV})$ , which is on the same order of magnitude as the recoil energy due to a 1 GeV dark matter collision.

On the other hand, above  $\sim 10\text{ GeV}$  the sensitivities of the experiments all decrease at a rate inversely proportional to the dark matter mass. This is due to the interaction rate in Eq. 1.24 being proportional to the number of dark matter particles that pass through the detector,  $N_{\text{DM}} = \rho_{\text{DM}}/m_{\text{DM}}$ . As the local dark matter density is observed to be  $\rho_{\text{DM}} = 0.4\text{ GeV cm}^{-3}$ ,  $N_{\text{DM}}$  decreases as the dark matter mass increases, and hence so do the detector sensitivities.

Direct detection limits also assume that the scattering cross-section is independent of the dark matter velocity and momentum transfer in the interaction. Given that the local dark matter dispersion velocity is predicted to be  $v_d = 270\text{ km s}^{-1} \approx 10^{-3}c$ , a back-of-the-envelope estimation for the momentum transfer gives  $q_{\text{tr}} \lesssim 100\text{ MeV}$ . Therefore, cross-sections proportional to  $v_{\text{DM}}$  or  $q_{\text{tr}}$  will result in significantly lower event rates and hence much weaker limits than the unsuppressed interactions.

### 1.3.3 Indirect Detection

This leads us to indirect detection methods, which can provide complementary probes to direct detection while also exploring interactions that are difficult, if not impossible, for terrestrial-based detectors to observe. Indirect detection experiments aim to infer the presence of dark matter through its annihilation or decay into Standard Model states. These searches look for dark matter annihilation products from astrophysical sources, including:

- Gamma-rays at terrestrial-based telescopes such as HESS [59–61], VERITAS [62–64], MAGIC [65, 66] and HAWC [67–70] as well as the Fermi-LAT [71–75] satellite;

- Neutrino signals at IceCube [76, 77], ANTARES [78–80], Super-K [81–83], and will be searched for at the upcoming Hyper-K [84–86], JUNO [87] experiments.
- Cosmic-Ray antimatter excess observed by the AMS-02 experiment [88, 89]

Signals from dark matter annihilation are best searched for by looking at regions where the dark matter density is expected to be high, boosting the annihilation rate. Natural places to look include the Galactic Centre [90, 91], dwarf-spheroidal galaxies [92], and celestial bodies where dark matter can accumulate over time. The latter scenario is central to this work and was pioneered by considering the effects of dark matter being captured within the Sun.

## 1.4 Dark Matter Signals from the Sun

Stars have a rich history of being used as astrophysical laboratories to help in the search for dark matter. Depending on the type of dark matter being searched for, there are various signals one can look for. Light bosonic dark matter, such as ALPs and dark photons, can be produced within the plasma of stars, altering the energy transport properties within them. This can ultimately lead to deviations in the evolution of the star, which can be used to place some of the strongest constraints on these models [93–95]. WIMP-like dark matter in the halo that couples to visible matter can scatter within the stars as they pass through. If the dark matter loses enough energy in these interactions, it can become gravitationally bound to the object and a population of dark matter will be accumulated within the star over time [23, 96–99].

This idea of WIMPs accumulating within the cores of stars has been applied extensively to the star closest to us, the Sun. The formalism for stellar capture of dark matter was set up by Gould [97, 98, 100] in the late 80’s, and has remained quite successful to this day, with many authors continuing to build upon these foundations over time [99, 101, 102].

Once the dark matter is captured, it will continue to scatter with the stellar constituents until it thermalises within the core of the Sun, collecting with an isothermal sphere. The radius of this sphere can be found by applying the virial theorem, with the gravitational potential given by

$$\Phi(r) = - \int_r^\infty \frac{GM_\odot(r')}{r'^2} dt', \quad (1.28)$$

$$\approx \frac{2}{3}\pi G\rho_{\odot,c}r^2, \quad (1.29)$$

assuming the density of the Sun within this region is constant,  $\rho_{\odot,c}$ . The resulting radius is

$$r_{\text{iso}}^2 = \frac{3T_{\odot}}{2\pi G m_{\text{DM}} \rho_{\odot}}. \quad (1.30)$$

The dark matter number density will follow a Gaussian profile,

$$n_{\text{iso}}(r) = n_0 \exp\left(-\frac{m_{\text{DM}}\Phi(r)}{T_{\odot}}\right), \quad (1.31)$$

$$= n_0 \exp(-r^2/r_{\text{iso}}^2), \quad (1.32)$$

where  $n_0$  is a normalisation constant fixed by requiring that the total number of dark matter particles is

$$N_{\text{DM}} = \int d^3r n_{\text{iso}}(r). \quad (1.33)$$

In addition, dark matter velocity will follow a Maxwell-Boltzmann distribution,

$$f_{\text{MB}}(v) = 4\pi \left(\frac{m_{\text{DM}}}{4\pi T_{\odot}}\right)^{3/2} v^2 \exp\left[-\frac{m_{\text{DM}}v^2}{4T_{\odot}}\right]. \quad (1.34)$$

The time evolution of the total number of dark matter particles within the Sun is governed by three processes. Capture acts to increase the number over time, while annihilation and evaporation will reduce this number over time. This is described by the differential equation

$$\frac{dN_{\text{DM}}}{dt} = C - EN_{\text{DM}} - AN_{\text{DM}}^2, \quad (1.35)$$

where  $C$  and  $E$  are the capture and evaporation rates respectively, with  $A$  being related to the annihilation rate,  $\Gamma_{\text{ann}}$  through

$$\Gamma_{\text{ann}} = \frac{1}{2} \int dr^3 n_{\text{iso}}^2(r) \langle \sigma_{\text{ann}} v \rangle \quad (1.36)$$

$$\equiv \frac{1}{2} A N_{\text{DM}}^2, \quad (1.37)$$

where the factor of 1/2 accounts for each annihilation removing two dark matter particles from the Sun.

In this context, evaporation refers to the process in which dark matter can be ejected back out of the Sun by up-scattering<sup>10</sup> off an energetic constituent. This

---

<sup>10</sup>Up-scattering refers to the interactions in which the dark matter gains rather than loses energy.

becomes increasingly important for lighter dark matter masses, as less energy will be required to boost the dark matter above the local escape velocity. Below a certain mass, the capture and evaporation come into equilibrium, and a net-zero amount of dark matter is contained within the Sun. This critical mass places a lower bound on the dark matter mass that can be probed through stellar capture and is named the evaporation mass,  $m_{\text{evap}}$ .

There are three regimes we are interested in solving this equation for. The simplest case is when evaporation and annihilation are both negligible, then the solution is simply,

$$N_{\text{DM}}(t) = Ct, \quad (1.38)$$

indicating that the dark matter will simply continue to grow over time.

Next, assume that annihilations are negligible ( $A = 0$ ), while capture and evaporation are present. The result is

$$N_{\text{DM}}(t) = Ct \left( \frac{1 - e^{-Et}}{Et} \right), \quad (1.39)$$

where the first factor is the number of captured dark matter if evaporation is negligible. From this, we can estimate the evaporation mass by asking when the evaporation rate is large enough to cause a significant reduction in the number of captured dark matter particles relative to the  $E = 0$  case. This can be expressed formally as [101]

$$\frac{1}{N_{\text{DM}}(m_{\text{evap}})} \left| N_{\text{DM}}(m_{\text{evap}}) - \frac{C(m_{\text{evap}})}{E(m_{\text{evap}})} \right| = \alpha, \quad (1.40)$$

where  $\alpha$  is the fraction of evaporated dark matter, taken to be  $\sim 10\%$ .

Finally, consider the case in which evaporation can be neglected,  $m_{\text{DM}} \gtrsim m_{\text{evap}}$ . The solution in this regime is

$$N_{\text{DM}}(t) = \sqrt{\frac{C}{A}} \tanh(\sqrt{CA}t) \xrightarrow{t \rightarrow \infty} \sqrt{\frac{C}{A}}, \quad (1.41)$$

that reaches an equilibrium state between capture and annihilation for times longer than the characteristic scale,  $t_{\text{eq}} = 1/\sqrt{CA}$ . This state is known as capture-annihilation equilibrium.

The signals searched for depend on whether the dark matter can annihilate or not. If the dark matter is asymmetric, it cannot annihilate, and we can set  $A = 0$  in Eq. 1.35. This leads to the population continuing to grow over time, with  $N_{\text{DM}}(t) = Ct$  if evaporation is negligible. A large enough population of captured dark matter can alter the energy transport within the Sun, leading to the modifications of the solar neutrino flux, or even the solar structure itself [87, 103–105].

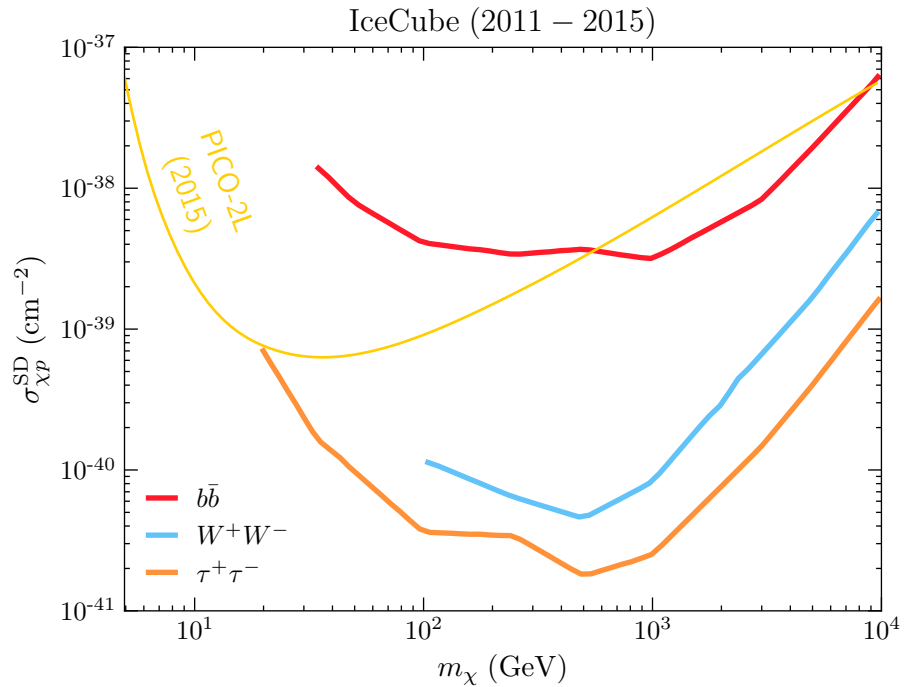


**Figure 1.6:** Limits on the SD dark matter-proton cross-section from the IceCube collaboration assuming 100% branching fraction to  $b\bar{b}$  (red),  $W^+W^-$  (blue) or  $\tau^+\tau^-$  (orange) final states. Also shown is the result from the PICO-2L DD experiment. This plot was recreated with data taken from Ref. [76].

Instead, if the dark matter can annihilate an equilibrium will eventually be reached between the capture and annihilation rates, and the total number of dark matter particles will be constant. If the annihilation products can escape the Sun, they can be searched for by various experiments depending on the nature of the final states. These could be neutrinos produced from the decays of other charged annihilation products [79–81, 106, 107], or to some other long-lived state that can escape the Sun and decay into visible states [108–112].

In comparison to DD searches, interpretation of indirect detection data will require additional model-dependent assumptions, namely the relevant annihilation channels of the dark matter. The most general limits can be placed by assuming that the dark matter only has a single annihilation channel, i.e. annihilation to a  $\tau^+\tau^-$  final state 100% of the time. Under these assumptions, limits on the SD dark matter-proton cross-section have been placed that exceed current DD constraints, due to the rather large abundance of Hydrogen within the Sun. Constraints from the IceCube collaboration are shown in Fig. 1.6.

As stated above, the range of dark matter masses that can be probed by Solar

capture is limited by the evaporation mass of  $\sim 3$  GeV. Additionally, as with direct detection, interactions that are suppressed by the momentum transfer/velocity of the dark matter will result in a significantly smaller capture rate and hence a smaller flux of annihilation products, resulting in weaker limits. These constraints also rely on the annihilation rate being sufficiently fast such that capture-annihilation equilibrium is reached within the lifetime of the Sun. If the annihilation cross-section is  $p$ -wave suppressed by the velocity of the annihilating dark matter, then this equilibrium may not be achieved. Should this be the case, then no limits can be placed as no flux of annihilation products to detect.

Overcoming the first of these issues requires either a colder star or one that is much heavier to decrease the evaporation mass. The second requires dark matter to scatter with the constituent material at relativistic energies to overcome the suppression in the cross-sections. Finally, the  $p$ -wave suppression can be alleviated if the dark matter annihilates within a very small volume in the core of the star, boosting the annihilation rate. Fortunately, there exist objects that can achieve all of these requirements, allowing for a wider variety of dark matter models to be explored than direct detection or traditional indirect detection experiments. These objects are known as compact objects, namely neutron stars and white dwarfs.

## 1.5 Compact Objects as Dark Matter Probes

The main goal behind this work is to explore how compact objects can be used to probe a wide variety of dark matter interactions that terrestrial direct detection experiments are insensitive to. By compact objects, we are referring to Neutron Stars (NSs) and White Dwarfs (WDs), and not Black Holes that also fall into this category.

Compact objects offer a unique laboratory for studying dark matter and its interactions with the Standard Model in environments unachievable anywhere else in the Universe. They generate strong gravitational fields and are composed of incredibly dense matter, with NSs reaching super-nuclear densities in their central cores. The capture rate within these objects is therefore enhanced due to these properties, with benefits over solar capture including:

- **Gravitational focusing of the DM flux:** The strong gravitational field will increase the impact parameter of the infalling dark matter. This increases the effective size of the capturing body, increasing the flux of dark matter passing through it.
- **Relativistic Interaction Energies:** In general, the infalling dark matter will be accelerated to (semi-)relativistic velocities ( $\sim 0.2 - 0.7c$ ). Moreover,

the stellar constituents will also have relativistic energies. As such, interactions that are momentum/velocity dependent will suffer far less suppression than in DD experiments.

- **Large Number of Targets:** The extremely high densities of these objects correspond to a considerable number of targets for scattering to occur. This allows these objects to probe very small scattering cross-sections, with NSs in particular expected to reach as low as  $\sim 10^{-45} \text{ cm}^2$ .
- **Low Evaporation Masses:** Relative to the Sun, the evaporation mass in compact objects can be quite low, on the order of keV in some cases. This is due in part to the increased gravitational strength, but mainly to the significantly lower temperatures in old compact objects.

In the past, capture in NSs has been applied primarily in the context of seeding gravitational collapse into black holes [113–119], and the modifications of NS merger rates as well as the gravitational wave signatures of these mergers [120–123]. Capture in WDs has also been considered, with a variety of different applications of the capture process [124–129].

In recent years, dark matter induced heating of NSs has reemerged as a potential detection frontier [130–137]. It was shown that dark matter could reheat old, isolated NSs in our local neighbourhood<sup>11</sup> back up to temperatures that would cause them to radiate as blackbody peaked in the near-infrared. The aim is to locate the NSs with radio telescopes such as the Square-Kilometer-Array (SKA), and determine their age through their spin-down rate. Once located, the star's temperature can be determined through observations from infrared telescopes such as the James Webb Space Telescope (JWST). Knowing the age of the star allows us to compare its observed temperature to that predicted by models of neutron star cooling. A discrepancy between these two temperatures can indicate whether an additional heating source is present within the star.

This heating occurs in two stages. The dark matter will first kinetically heat the star through the scattering events that result in both its capture and thermalisation. We define *kinetic heating* to have been achieved once the dark matter has deposited 99% of its initial kinetic energy into the star. If the dark matter can annihilate, and assuming these annihilation products remain trapped within the star, its mass energy will be transferred to the star, further increasing the temperature of the star. In order for this *annihilation heating* to be efficient, capture-annihilation equilibrium must be achieved on a timescale shorter than the age of the star. These processes are illustrated in Fig. 1.7, with the temperatures shown assuming a NS in our local neighbourhood.

---

<sup>11</sup>Local neighbourhood refers to the region within  $\sim 1 \text{ kpc}$  of the Sun.

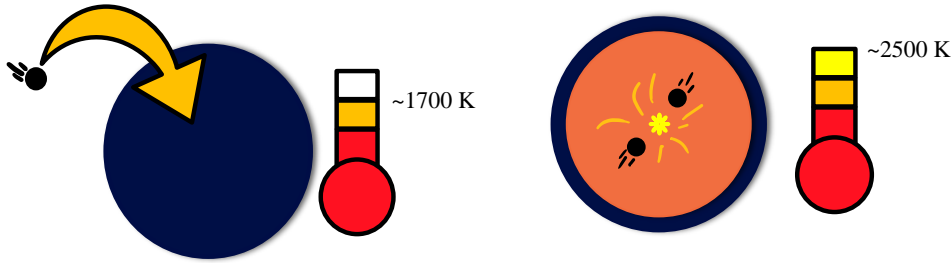


**Figure 1.7:** Illustration of DM-induced heating of compact objects. **Left:** kinetic heating due to DM scattering, raising the temperature to  $\sim 1700$  K. **Right:** Annihilation heating contributes an additional  $\sim 800$  K. This image is inspired by Ref. [130].

It is important to keep track of all the timescales involved in the heating process so that we can accurately determine the full extent of dark matter-induced heating. These timescales are the age of the star,  $t_*$ , the kinetic heating time,  $t_{\text{kin}}$ , and the capture-annihilation heating timescale,  $t_{\text{eq}}$ . In order for maximal heating to be achieved, we require  $t_{\text{kin}} + t_{\text{eq}} < t_*$ .

To accurately project how sensitive neutron star heating to dark matter interactions, one first requires an accurate calculation of the capture rate. However, existing calculations have relied on the formalism set up by Gould for capture in the Sun without fully accounting for the extreme physics present in these objects. Developing a consistent formalism for dark matter capture in compact objects, based on the Gould formalism, and applying this to dark matter induced heating is at the heart of this thesis.

## 1.6 Thesis Outline

Following this introduction, Chapter 2 covers the prerequisite knowledge of compact objects required for the remainder of this work. This includes a detailed overview of the general structure equations of relativistic stars, followed by details of the internal structure of both white dwarfs and neutron stars.

Chapters ?? and ?? of this thesis are devoted to reformulating Gould's capture formalism to account for the physics specific to compact objects in a self-consistent manner. These include a relativistic treatment of the kinematics, using General Relativity to calculate the correct dark matter flux passing through the star, and accounting for Pauli blocking of the final state target using Fermi-Dirac statistics for the stellar constituents. In addition, we incorporate the internal structure of these objects by calculating the radial profiles for the relevant microscopic quantities (e.g.,

chemical potentials and number densities) via the adoption of a realistic equation of state.

Further considerations are required when considering dark matter interactions with the baryonic matter inside NSs. Due to the high density of the NS interior, the baryons undergo strong self-interactions and should not be treated as a free Fermi gas. Instead, adopting an equation of state that accounts for these interactions is required. These interactions modify the mass of the baryons, leading them to obtain an effective mass smaller than their value in vacuum. Furthermore, as we will see, the dark matter may interact with the baryons with momentum transfers on the order of 10 GeV. This is high enough that the dark matter will begin to resolve the internal structure of the baryon. To account for this, the momentum dependence of the baryon form factors that are typically neglected in direct detection and solar capture must be reintroduced.

This formalism is made in preparation for a thorough analysis of the timescales involved in the dark matter heating of compact objects, covered in Chapter ???. The energy deposited in both the kinetic and annihilation heating stages does not occur instantaneously, and the timescales involved in them need to be compared to the age of the star in question. We will define kinetic heating timescale as the time required for dark matter to deposit 99% of its initial kinetic energy into the star. For annihilation heating to occur, the dark matter must reach a state of capture-annihilation equilibrium within the stellar core. In standard calculations of this timescale, the dark matter must first become thermalised with the star. Only then can annihilations occur efficiently enough to heat the star.

We will work with the EFT operators in Table 1.1 that describe Dirac fermion dark matter interacting with Standard Model fermions. Each operator will be studied in isolation, i.e., by considering a Lagrangian that contains only one of the operators rather than a linear superposition of multiple. This way, we can analyse specific types of interactions independently, allowing us to take as model-independent an approach to the phenomenology as possible.

We present our concluding remarks on this thesis in Chapter ??.

# 2

## A Primer on Compact Objects

Within the cores of stars, there exists a delicate balance between the gravitational forces pulling the matter inward, and the outward pressure generated by the thermonuclear fusion of light elements. This process begins as hydrogen is fused to form helium. Eventually, the hydrogen is depleted, allowing gravity to temporarily overcome the outward pressure, leading to the core to begin contracting. As this occurs, the gravitational potential energy is converted to thermal energy and the core eventually becomes hot enough to facilitate helium burning.

This cycle can continue as heavier and heavier elements are formed within the ever-increasingly hot stellar core. Lighter stars cannot reach the temperatures required to fuse light elements such as helium and carbon. If the star is heavy enough, iron will eventually be formed from the burning of silicon. As the fusion of iron nuclei is an endothermic process, it will not occur spontaneously, ending the cycle in heavy stars. Without a fuel source, the core will collapse under its gravity, leading to the death of the star.

What comes after this collapse depends on the mass of the progenitor star. Very light stars,  $\lesssim 0.5M_{\odot}$ , have lifetimes much longer than the age of the universe, and so are uninteresting to our current discussion. Moderately heavy stars,  $1M_{\odot} \lesssim M_{\star} \lesssim 8M_{\odot}$ , will continue burning fuel until the outer layers of the star are dispersed as it expands, leaving a core comprised of helium, carbon, and oxygen with small abundance of heavier elements. In this case, the core will begin to collapse until the Fermi degeneracy of the ultrarelativistic electrons is great enough to reestablish equilibrium, resulting in a White Dwarf (WD) [138].

Heavy stars,  $\gtrsim 8M_{\odot}$ , spectacularly end their lives in a type-II supernova event. This occurs when the core of the star exceeds the Chandrasekhar mass of  $1.4M_{\odot}$ , which cannot be supported by electron degeneracy pressure. The core itself will then collapse, leading to a shockwave that ejects the majority of the mass of the

star. All that will remain is an extremely dense core supported by neutron degeneracy pressure: a Neutron Star (NS) [139]. If the star was so massive that the gravitational forces overcome even the neutron degeneracy pressure, then the core collapses into a black hole.

These stellar corpses, white dwarfs, neutron stars, and black holes, are collectively known as compact objects. They have masses similar to or larger than the Sun, which is compressed into much smaller bodies with significantly larger surface gravities. These objects do not have a source of fuel, and spend the rest of their lives cooling through the emission of photons and neutrinos. For the remainder of this thesis, we will only be interested in white dwarfs and neutron stars and will collectively refer to these as compact objects, excluding black holes from this term.

This chapter is dedicated to discussing the aspects of the structure, composition, and observational status of compact objects relevant to this work

## 2.1 Structure Equations from General Relativity

Being comprised of matter in a highly dense state, the gravitational fields produced by neutron stars and white dwarfs are extremely strong. As such, modeling the structure of these objects falls into the domain of General Relativity (GR). Here we review the structure of static, spherically symmetric, compact objects, adapting the discussions in Refs. [140–142].

First, the static nature of the star means that the components of the metric are functions only of the spatial coordinates and not of time. Together with the assumption that the mass distribution of the star is spherically symmetric, this leads to a Schwarzschild-like metric of the form

$$ds^2 = -d\tau^2 = -B(r)dt^2 + A(r)dr^2 + r^2d\Omega^2, \quad (2.1)$$

with  $d\tau$  the proper time interval. The functions  $A(r)$ ,  $B(r)$  depend only on the radial coordinate, and are often written as

$$A(r) = e^{2\Lambda(r)}, \quad B(r) = e^{2\Phi(r)}. \quad (2.2)$$

These functions are subject to the condition that at distances far from the star,  $r \rightarrow \infty$ , space-time must become flat, which translates to the boundary conditions

$$\lim_{r \rightarrow \infty} A(r) = \lim_{r \rightarrow \infty} B(r) = 1. \quad (2.3)$$

The matter within the star can be modeled as a perfect fluid, meaning we are neglecting any shear stresses and energy transport within the star. Such a fluid is

described by its pressure  $P(r)$ , density  $\rho(r)$ , and baryonic number density,  $n_b(r)$ , as well as the 4-velocity of the fluid  $u^\mu(r)$ . Being static, the only non-zero component of this velocity is the  $\mu = 0$  component, which is fixed by the normalisation condition  $g_{\mu\nu}u^\mu u^\nu = -1$  to be  $u^0 = 1/\sqrt{B(r)}$ . These quantities are used to construct the stress-energy tensor of the star, which takes the form

$$T^{\mu\nu} = (\rho + P)u^\mu u^\nu + Pg^{\mu\nu}. \quad (2.4)$$

The physics describing the underlying microscopic interactions within matter are encoded in an equation of state (EoS) that describes the relationship between the various thermodynamic quantities. This is typically expressed by providing the pressure as a function of the density,  $P(\rho)$ . It is often more convenient to parameterise the EoS by the number density of baryons  $n_b$ , and the entropy per baryon  $s$ , such that

$$P = P(n_b, s), \quad \rho = \rho(n_b, s). \quad (2.5)$$

The dependence on  $s$  turns out to be trivial in most scenarios involving compact objects, such as those considered throughout this work. The pressure in these stars arises from the degeneracy of the nucleons in NSs or the electrons in WDs, rather than from the thermal motion of the constituents as in main sequence stars. These thermal degrees of freedom will be frozen out at temperatures lower than the Fermi energy of the system, which is typically around  $E_F \sim 10$  MeV in NSs or  $\sim 1$  MeV in WDs, and correspond to temperatures of  $T_* \sim 10^{11}$  K and  $\sim 10^{10}$  K respectively. As these objects are expected to cool well below these temperatures quickly after formation [143–145], the entropy can be taken to be zero throughout the star. This allows us to reduce the two-parameter EoS to a simpler one-parameter one,

$$P = P(n_b, s = 0) = P(n_b), \quad \rho = \rho(n_b, s = 0) = \rho(n_b). \quad (2.6)$$

The structure of the star is therefore dictated by the quantities  $A(r)$ ,  $B(r)$ ,  $P(r)$ ,  $\rho(r)$ , and  $n_b(r)$ . This system is determined by applying the Einstein field equations,  $G^{\mu\nu} = 8\pi T^{\mu\nu}$ , together with the energy-momentum conservation,  $T^{\mu\nu}_{;\nu} = 0$ , the EoS relations Eqs. 2.6, and the appropriate boundary conditions. The structure equations that come out of this analysis were first discovered concurrently by Tolman [146] and by Oppenheimer and Volkoff [147], and so are known as the TOV equations. They take the form

$$\frac{dP}{dr} = -\rho(r)c^2 \left[ 1 + \frac{P(r)}{\rho(r)c^2} \right] \frac{d\Phi}{dr}, \quad (2.7)$$

$$\frac{d\Phi}{dr} = \frac{GM(r)}{c^2 r^2} \left[ 1 + \frac{4\pi r^3 P(r)}{M(r)c^2} \right] \left[ 1 - \frac{2GM(r)}{c^2 r} \right]^{-1}, \quad (2.8)$$

$$\frac{dB}{dr} = 2B(r) \frac{d\Phi}{dr}, \quad (2.9)$$

where  $M(r)$  is related to the metric factor  $A(r)$  through

$$A(r) = \left[ 1 - \frac{GM(r)}{c^2 r} \right]^{-1}, \quad (2.10)$$

and is interpreted as the mass contained within a radius  $r$ . It obeys the mass equation

$$\frac{dM}{dr} = 4\pi r^2 \rho(r), \quad M(0) = 0, \quad (2.11)$$

which arises from the  $\mu = \nu = 0$  component of the Einstein field equations. These equations are the general relativistic versions of the hydrostatic equilibrium equations of regular stellar structure, with Eq. 2.7 reducing to the familiar

$$\frac{dP}{dr} = -\frac{GM(r)}{r^2} \rho(r), \quad (2.12)$$

in the Newtonian limit,  $GM(r)/c^2 r \ll 1$ .

The radius of the star,  $R_\star$ , is identified as the point at which the pressure and density vanish,  $P(R_\star) = \rho(R_\star) = 0$ . In the region outside the star,  $r > R_\star$ , the total mass remains constant at the total mass of the star,  $M(r \geq R_\star) = M_\star$ , and so the only non-trivial structure functions in this region are the metric factors. Solving Eq. 2.9 for  $B(r)$  with  $P(r) = 0$  and constant  $M(r) = M_\star$  leaves us with

$$A(r) = \left[ 1 - \frac{GM_\star}{c^2 r} \right]^{-1}, \quad B(r) = 1 - \frac{GM_\star}{c^2 r}, \quad \text{for } r > R_\star, \quad (2.13)$$

and the metric reduces to the familiar Schwarzschild metric outside the star. Continuity of the metric at  $r = R_\star$  enforces a second boundary condition for  $B(r)$ ,

$$B(R_\star) = 1 - \frac{GM_\star}{c^2 R_\star}. \quad (2.14)$$

The final boundary condition required is the central pressure  $P(0) = P_c$  or, equivalently the central density/baryon number density. This is the only free parameter in the system and hence, for a given EoS, uniquely determines the stellar structure. Therefore, all the stars that are predicted by solving the coupled TOV + EoS system can be represented by a one-parameter sequence, represented by the mass-radius relation for the EoS model.

Given all the above, we can write a simple recipe for constructing a model of a compact object:

1. Model the constituent matter with an appropriate EoS.

2. Specify the central pressure of the star,  $P_c$ .
3. Integrate the coupled system of differential equations 2.7, 2.8, 2.11 from the centre of the star outward until the pressure vanishes.
4. Use the boundary condition Eq. 2.14 to normalise the metric function  $B(r)$ .

In general, additional quantities will be present in the EoS, such as chemical potentials and the speed of sound, which may be subject to additional constraints. These quantities will need to be calculated at each step of the integration alongside the other structure functions.

## 2.2 White Dwarfs

The fate of main sequence stars of mass below  $M_\star \lesssim 8M_\odot$  is to end their lives as a white dwarf. Consequently, these compact stellar remnants, which are supported against gravitational collapse by electron degeneracy pressure, are the most abundant stars in the Galaxy ( $\gtrsim 90\%$ ). They are born at very high temperatures and cool down over billions of years. Observations of the coldest WDs therefore contain information about the star formation history of the Galaxy.

The vast majority of observed WDs are composed primarily of carbon and oxygen, plus small traces of elements heavier than helium. At the extremely high densities found in WDs,  $\rho_\star \sim 10^6 - 10^{10} \text{ g cm}^{-3}$ , electrons are strongly degenerate and determine the WD equation of state (EoS) and internal structure. The stellar core resembles a Coulomb lattice of ions surrounded by the degenerate electron gas, implying that the WD core is isothermal and a very good thermal conductor. The degenerate core is enclosed by a thin envelope that accounts for  $\lesssim 1\%$  of the total mass [148].

The outer layers form an atmosphere that is rich in lighter elements such as hydrogen or helium, where the exact composition depends on the evolution of the WD progenitor and changes as the WD cools. This atmosphere is non-degenerate and extremely opaque to radiation, with an EoS that is subject to finite temperature effects. We limit our discussion to the core region of the WD, which accounts for the vast majority of its mass.

### 2.2.1 The FMT Equation of State

In the limit of zero temperature, the simplest way to obtain the WD EoS is to assume an ideal Fermi gas of degenerate electrons, for a WD that is primarily composed of a single element. Corrections to the non-interacting electron picture

were introduced early by Salpeter [149]. By introducing the Wigner-Seitz (WS) cell approximation and assuming point-like nuclei, Salpeter obtained an analytical EoS that accounts for interactions between electrons and ions as well as other Coulomb corrections. These corrections, in general, depend on the chemical composition of the star.

More recently, it has been shown that the treatment of matter at high pressures presented by Feynman, Metropolis and Teller [150] can be extended to consistently take into account weak interactions and relativistic effects [151, 152], and incorporates Coulomb corrections in a more natural manner than the Salpeter EoS. The resulting Feynman-Metropolis-Teller (FMT) EoS is obtained by considering a relativistic Thomas-Fermi model within Wigner-Seitz cells of radius  $R_{\text{WS}}$ . For degenerate, relativistic, electrons, the equilibrium condition is that the Fermi energy,  $E_e^F$ , is constant within the cell,

$$E_e^F = \sqrt{(p_e^F)^2 + m_e^2} - m_e - eV(r) = \text{constant}, \quad (2.15)$$

where  $V(r)$  is the Coulomb potential inside the cell,  $p_e^F$  is the electron Fermi momentum,  $m_e$  is the electron mass and  $e$  is the electric charge. To obtain an integrable solution for the energy density near the origin, it is necessary to introduce a finite size for the nucleus, with radius  $R_c = \Delta\lambda_\pi Z^{1/3}$ , where  $\lambda_\pi$  is the pion Compton wavelength,  $\Delta \approx (r_0/\lambda_\pi)(A/Z)^{1/3}$ ,  $Z$  is the proton number,  $A$  is the atomic mass, and  $r_0$  is an empirical constant  $\sim 1.2$  fm. The proton and electron number densities inside the cell are then given by

$$n_p = \frac{(p_p^F)^3}{3\pi^2} = \frac{3Z}{4\pi R_c^3} \theta(R_c - r) = \frac{3}{4\pi} \left( \frac{1}{\Delta\lambda_\pi} \right)^3 \theta(R_c - r), \quad (2.16)$$

$$n_e = \frac{(p_e^F)^3}{3\pi^2} = \frac{1}{3\pi^2} \left[ \hat{V}^2(r) + 2m_e \hat{V}(r) \right]^{3/2}, \quad (2.17)$$

$$\hat{V}(r) = eV(r) + E_e^F. \quad (2.18)$$

The Coulomb potential satisfies the Poisson equation

$$\nabla^2 V(r) = -4\pi e[n_p(r) - n_e(r)], \quad (2.19)$$

with the requirement of global charge neutrality of the cell enforcing the boundary conditions

$$\left. \frac{dV}{dr} \right|_{r=R_{\text{WS}}} = V(R_{\text{WS}}) = 0. \quad (2.20)$$

In practice, it is beneficial to work with dimensionless quantities, and so we define  $x = r/\lambda_\pi$  and  $\chi(r) = r\hat{V}(r)$ , such that  $x_c = R_c/\lambda_\pi$  and  $x_{\text{WS}} = R_{\text{WS}}/\lambda_\pi$ . Using

these expressions results in the relativistic Thomas-Fermi equation

$$\frac{1}{3x} \frac{d^2\chi}{dx^2} = -\frac{\alpha_{\text{EM}}}{\Delta^3} \theta(x_c - x) + \frac{4\alpha_{\text{EM}}}{9\pi} \left[ \frac{\chi^2(x)}{x^2} + 2 \frac{m_e}{m_\pi} \frac{\chi(x)}{x} \right]^{3/2}, \quad (2.21)$$

with the boundary conditions

$$\chi(0) = 0, \quad \left. \frac{d\chi}{dx} \right|_{x_{\text{WS}}} = \frac{\chi(x_{\text{WS}})}{x_{\text{WS}}}. \quad (2.22)$$

By solving these equations, we can obtain the relevant thermodynamic quantities, namely the electron and proton number densities, electron chemical potential, and the energy and pressure of the cell. The electron chemical potential is obtained by evaluating Eq. 2.15 at the cell radius, noting that the Coulomb potential must vanish there, which results in the usual expression<sup>1</sup>

$$\varepsilon_{F,e} = \sqrt{(p_e^F)^2 + m_e^2} - m_e. \quad (2.23)$$

The energy and pressure of the cell can then be obtained following the analysis presented in ref. [152]. The cell energy gains contributions from the nuclear mass, electron kinetic energy, and Coulomb interactions, such that

$$E_{\text{tot}} = M_N + E_k + E_C, \quad (2.24)$$

$$E_k = \int_0^{R_{\text{WS}}} 4\pi r^2 [\mathcal{E}_e(r) - m_e n_e(r)] dr, \quad (2.25)$$

$$E_C = \frac{1}{2} \int_{R_c}^{R_{\text{WS}}} 4\pi r^2 e [n_p(r) - n_e(r)] V(r) dr, \quad (2.26)$$

where

$$\mathcal{E}_e(r) = \frac{1}{\pi^2} \int_0^{p_e^F} p^2 \sqrt{p^2 + m_e^2} dp, \quad (2.27)$$

is the electron energy density, and  $M_N$  is the mass of the nucleus. The energy density of the cell is then simply

$$\rho_{\text{WS}} = \frac{E_{\text{tot}}}{V_{\text{WS}}}, \quad (2.28)$$

where  $V_{\text{WS}} = 4\pi R_{\text{WS}}/3$  is the volume of the WS cell. The only contribution to the internal cell pressure comes from the electrons,

$$P_e(r) = \frac{1}{3\pi^2} \int_0^{p_e^F} \frac{p^4}{\sqrt{p^2 + m_e^2}} dp, \quad (2.29)$$

---

<sup>1</sup>We use the symbol  $\varepsilon_{F,i}$  to represent the chemical potential minus the mass of a particle species  $i$ , reserving  $\mu_{F,i}$  for the full chemical potential.

<b>EoS</b>	<b>WD<sub>1</sub></b>	<b>WD<sub>2</sub></b>	<b>WD<sub>3</sub></b>	<b>WD<sub>4</sub></b>
$\rho_c$ [g cm <sup>-3</sup> ]	$1.47 \times 10^6$	$3.84 \times 10^7$	$3.13 \times 10^8$	$2.31 \times 10^{10}$
$M_\star$ [ $M_\odot$ ]	0.440	1.000	1.252	1.384
$R_\star$ [km]	$9.39 \times 10^3$	$5.38 \times 10^3$	$3.29 \times 10^3$	$1.25 \times 10^3$
$v_{\text{esc}}(R_\star)$ [km/s]	$3.72 \times 10^3$	$7.03 \times 10^3$	$1.01 \times 10^4$	$1.71 \times 10^4$

**Table 2.1:** Four configurations for white dwarfs composed of carbon, with an FMT EoS. Shown are the central densities,  $\rho_c$ , stellar mass  $M_\star$  and radius  $R_\star$ , and escape velocity at the edge of the WD,  $v_{\text{esc}}$ .

with the total pressure of the cell being  $P_{\text{tot}} = P_e(R_{\text{WS}})$ . Finally, the EoS is then obtained by solving Eq. 2.21 for various cell radii, yielding a relation between  $E_{\text{tot}}(R_{\text{WS}})$  and  $P_{\text{tot}}(R_{\text{WS}})$  parameterised by the radius of the Wigner-Seitz cell.

Different WD configurations can be obtained, assuming a non-rotating spherically symmetric star, by solving the Tolman-Oppenheimer-Volkoff (TOV) equations [146, 147] coupled to the FMT EoS with different initial conditions for the pressure at the centre of the star. In Fig. 2.1 we show radial profiles for  $n_e$  (top left),  $\varepsilon_{F,e}$  (top right), and escape velocity  $v_{\text{esc}}$  (bottom) for the carbon WDs in Table 2.1. Note that the difference in radius between the lightest and heaviest WD in Table 2.1 spans almost one order of magnitude, while the electron number densities in the core can vary up to 4 orders of magnitude (see top left panel). As expected, electrons are more degenerate in more compact WDs and become relativistic (see top right panel). The escape velocity can reach  $\mathcal{O}(0.1 c)$  at the interior of the most compact WDs, while for very low mass WDs it can be as low as  $\sim 0.003 c$ .

The mass-radius relations obtained from a zero-temperature EoS begin to deviate from observations for low-mass WDs. To address this discrepancy, finite temperature effects can be introduced to the EoS [153]. The extension to finite temperatures is made by reintroducing the temperature dependence in the Fermi-Dirac distributions. Now, the electron chemical potential is no longer simply the Fermi energy of the system due to thermal corrections. Define the finite temperature Fermi-Dirac integrals of degree  $s$  as

$$F_s(\eta, \beta) = \int_0^\infty \frac{t^s \sqrt{1 + (\beta/2)t}}{1 + e^{t-\eta}} dt, \quad (2.30)$$

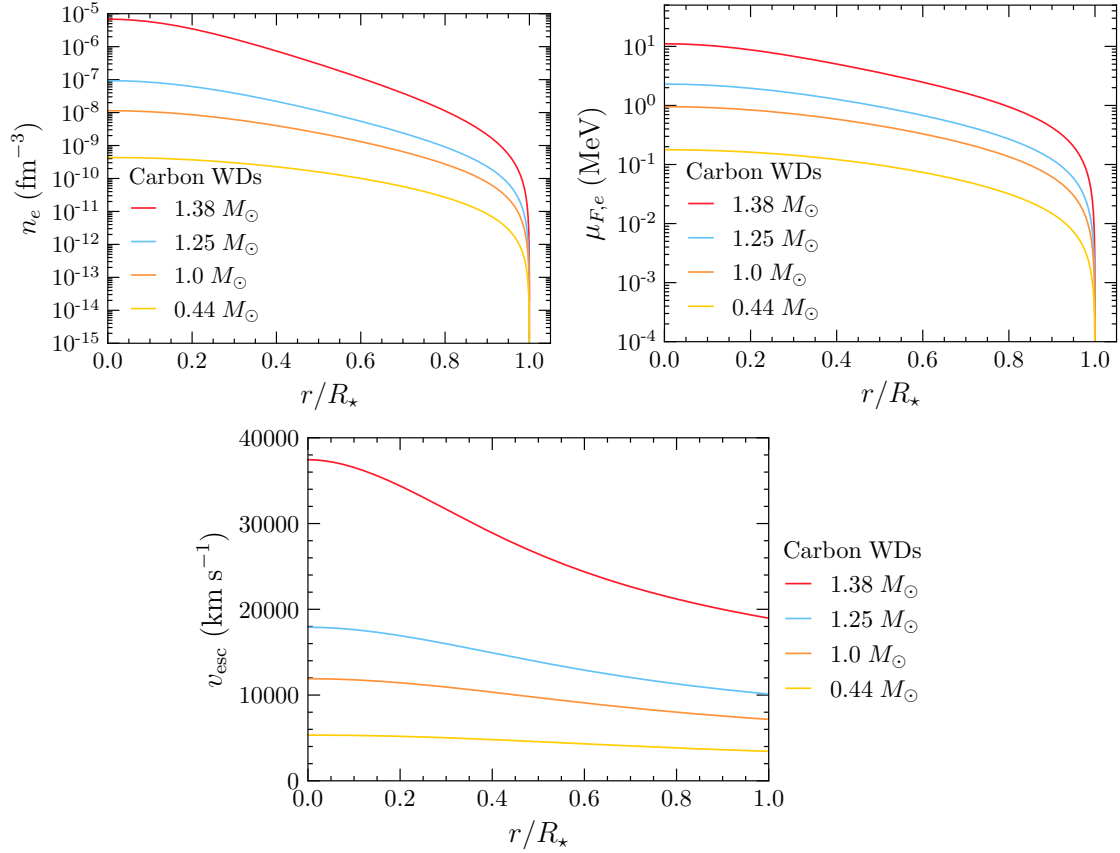


**Figure 2.1:** Electron number density (top left), chemical potential (top right), and escape velocity (bottom) radial profiles for the carbon WDs with FMT EoS in Table 2.1. The radial distance of each profile has been normalised to the radius of the star.

where we define the dimensionless quantities

$$t = \frac{E_e - m_e}{T_\star}, \quad (2.31)$$

$$\eta = \frac{\varepsilon_{F,e}}{T_\star}, \quad (2.32)$$

$$\beta = \frac{T_\star}{m_e}, \quad (2.33)$$

for a star at temperature  $T_\star$ . The Thomas-Fermi equilibrium condition within the WS cell is now given by

$$\varepsilon_{F,e}(r) - eV(r) = T_\star\eta(r) - eV(r) = \text{constant}, \quad (2.34)$$

with the Coulomb potential vanishing at the boundary of the cell as before. We now make the change of variables into the dimensionless quantities  $\chi/r = \varepsilon_{F,e}/(\hbar c)$  and  $x = x/x_{\text{WS}}$  so that the Poisson equation 2.19 becomes

$$\frac{d^2\chi}{dx^2} = -4\pi\alpha_{\text{EM}}x \left( \frac{3}{4\pi\Delta^3}\theta(x_c - x) - \frac{\sqrt{2}}{\pi^2} \left( \frac{m_e}{m_\pi} \right)^2 [F_{1/2}(\eta, \beta) + \beta F_{3/2}(\eta, \beta)] \right), \quad (2.35)$$

$$\eta(x) = \left( \frac{1}{\lambda_\pi T_\star} \right) \frac{\chi(x)}{x}, \quad (2.36)$$

with the same boundary conditions as in Eq. 2.22.

The total energy of the cell remains very similar to the zero-temperature case, with the main differences being that it gains a contribution from the thermal motion of the nucleus,

$$E_{\text{th}} = \frac{3}{2}T_\star, \quad (2.37)$$

and that the electron energy density is now given by

$$\mathcal{E}_e = m_e n_e + \frac{\sqrt{2}}{\pi^2} m_e^4 \beta^{5/2} [F_{3/2}(\eta, \beta) + \beta F_{5/2}(\eta, \beta)]. \quad (2.38)$$

The pressure of the cell will now gain contributions from the motion of the nucleus as well as the electron, such that the total pressure is

$$P_{\text{tot}} = P_N + P_e, \quad (2.39)$$

$$P_N = \frac{2}{3} \frac{E_{\text{th}}}{V_{\text{WS}}} = \frac{T_\star}{V_{\text{WS}}}, \quad (2.40)$$

$$P_e = \frac{2^{3/2}}{3\pi} m_e^4 \beta^{5/2} [F_{3/2}(\eta(x_{\text{WS}}), \beta) + \beta F_{5/2}(\eta(x_{\text{WS}}), \beta)]. \quad (2.41)$$

In Fig. 2.2 we show the Mass-Radius relations obtained from the zero temperature FMT EoS together with several finite temperature configurations. As can be seen, the deviations from the zero temperature approximation begin at rather high temperatures,  $T_\star \gtrsim 10^7$  K, for masses  $\lesssim 0.6M_\odot$ . Additionally, we show a random selection of 20,000 WDs presented in the Gaia early data release 2 (EDR2) report [154] as the yellow-red dots. The colour of the dot represents the internal temperature of the corresponding WD. The core temperature must be determined from the observed effective surface temperature of the star<sup>2</sup>, with the relation between the two depending on the composition of the WD atmosphere. To obtain the central temperature from the reported effective temperatures, we use the WD cooling sequences generated in Ref. [145]<sup>3</sup> assuming a thin hydrogen atmosphere. In general, there is good agreement between the mass-radius relations derived from the finite temperature FMT EoS and the observed internal temperatures of the WDs.

Given the non-linear nature of the differential equations that describe the FMT EoS (both at zero and finite temperatures), solving the system is a numerically challenging task. As there are no publically available resources to help solve these systems, a significant amount of time was put into solving this problem. As such, we have outlined in Appendix ?? the method employed in numerically solving the differential equations.

### 2.2.2 Observational Status

The rate at which the energy of the WD core is radiated away is determined by the outer non-degenerate layers of the atmosphere. Spectroscopic observations shed light on the composition of these layers and can be used to classify WDs in terms of  $\sim$  six spectral types. Most of the observed WDs lie in the DA (hydrogen-rich) and DB (helium-rich) categories. Note that as WDs slowly cool, they undergo spectral evolution. There is a well-defined relation between their luminosity and age (cooling time) that, together with recent breakthroughs in theory and observations, allow us to estimate the age of the stars within the solar neighbourhood and to date the nearest star clusters [155–159].

Over the past few decades, WDs have been extensively observed using photometry and spectroscopy. Most of the WDs have been discovered by large area surveys, such as the Sloan Digital Sky Survey (SDSS) [160]. However, these lo-

---

<sup>2</sup>The effective temperature is the temperature that characterises the surface of the star. Assuming that WDs are perfect blackbody emitters, the luminosity will be  $L_\gamma = 4\pi\sigma_{SB} R_\star^2 T_{\text{eff}}^4$ , where  $\sigma_{SB}$  is the Stefan–Boltzmann constant.

<sup>3</sup>The cooling sequence data can be obtained from  
<http://www.astro.umontreal.ca/bergeron/CoolingModels>.

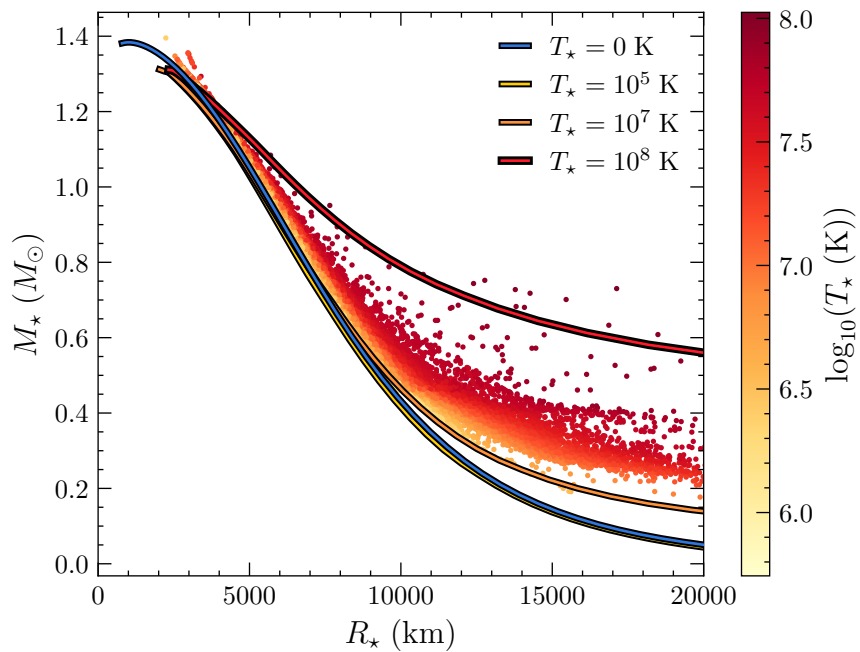


**Figure 2.2:** Mass-Radius relation of WDs calculated from the FMT EoS in the zero-temperature approximation (dark blue), at  $10^5$  K (yellow),  $10^7$  K (orange), and  $10^8$  K (red), together with observed WDs from Gaia EDR2 observations [154] (yellow-red dots). The colour of the dots represents the surface temperature of the WD inferred from cooling models [145].

cal samples are dominated by young WDs with relatively high effective temperatures ( $T_{\text{eff}} \gtrsim 10^4$  K) [161–165]. Recently, the local volume sample of nearby stars within  $\sim 100$  pc has been catalogued by the Gaia spacecraft [166, 167], an astrometric mission. New WD candidates have been identified [154], followed by dedicated spectroscopic observations [168, 169], increasing the local sample of cool WDs ( $T_{\text{eff}} \lesssim 5000$  K).

On the other hand, globular clusters (GCs) are the oldest known stellar systems in the Galaxy. Among them is Messier 4 (M4), also classified as NGC 6121, which is the closest globular cluster to Earth being  $\sim 1.9$  kpc away [170–172]. The age of M4, 11.6 Gyr, has been estimated using observations of faint cold WDs with the Hubble Space Telescope (HST) [155, 157]. This HST data, corrected for reddening and extinction, was converted into luminosities and effective temperatures in ref. [126]. From these calculations, it is possible to infer WD radii and their corresponding masses by assuming a mass-radius relation.

## 2.3 Neutron Stars

Being the end product of massive,  $\gtrsim 8M_{\odot}$ , stars, there are significantly fewer NSs than the WDs discussed above. As their name suggests, they are composed primarily of neutrons, which provide the degeneracy pressure required to prevent the gravitational collapse of the star. The internal structure of an NS is significantly more complicated than that of a WD. Broadly speaking, an NS can be divided into five main regions. We give an overview of the important features of each of these regions, and point the reader to Refs. [173–180] for more indepth discussions. Working from the outside in, these regions are:

### Atmosphere

The atmosphere is an extremely thin layer of plasma that makes up less than 1% of the NS mass. However, it plays an extremely important role as the observed spectrum radiation emitted by the star must pass through this region [174, 175].

### Outer Crust

The outer crust is the thin layer of ionized Iron-56 nuclei that extends down until the density reaches the neutron drip point,  $\rho_{\star} = \rho_{\text{ND}} \sim 4.3 \times 10^{11} \text{ g cm}^{-3}$ . This is the density at which neutrons begin to drip from the nuclei as their chemical potentials approach zero. The ionized electrons form a non-relativistic but degenerate gas,

with their chemical potentials increasing as the density increases. This leads to the “neutronisation” of the nuclei as the beta-capture of electrons by protons increases.

### Inner Crust

The density within the inner crust spans the range between  $\rho_{\text{ND}} \lesssim \rho_* \lesssim 0.5\rho_0$ , with  $\rho_0 \sim 2.8 \times 10^{14} \text{ g cm}^{-3}$  the nuclear saturation density (i.e. the density of nuclear matter) [174, 175, 181]. Here, the neutrons that have dripped from the nuclei will potentially form a superfluid. Towards the crust-core boundary, the nuclear lattice begins taking on interesting topological structures that are distinguished by the configuration of the voids in the lattice. These are known as the so-called *pasta phases* [182–184] of nuclear matter, which include 2D sheets (lasagna), cylindrical rods (spaghetti), or 3D clumps (gnocchi). Eventually, towards the crust-core interface the nuclear matter transitions into a uniform medium<sup>4</sup>.

### Outer Core

Once densities go above  $0.5\rho_0$ , the nuclear clusters will dissolve into a homogenous fluid that is composed of neutrons, protons, electrons, and muons known as *npeu* matter. The relative abundances of the species,  $Y_i = n_i/n_b$ , are dictated by the conditions of electrical neutrality and beta-equilibrium. Charge neutrality dictates that the abundances of the charged particles obeys

$$Y_p = Y_e + Y_\mu, \quad (2.42)$$

while beta-equilibrium refers to the balance between the weak decays of neutrons and the electron/muon capture by the protons,



with  $\ell = e, \mu$ . Muons will begin to replace electrons in these reactions once the electron chemical potential exceeds the mass of the muon,  $\mu_{F,e} \gtrsim m_\mu = 105.7 \text{ MeV}$ . As neutrinos are assumed to escape the NS once produced, the relation between the chemical potential of the leptons is simply

$$\mu_{F,e} = \mu_{F,\mu}. \quad (2.45)$$

The outer core region ends once the density reaches  $\rho_* \sim 2\rho_0$ , and we transition into the inner core.

---

<sup>4</sup>The nuclear minestrone, if you will.

### Inner Core

The densities within the inner cores of NSs extend between  $2\rho_0 \lesssim \rho_* \lesssim (10 - 15)\rho_0$  and are hence a mystery to this day. As the density greatly exceeds any material that can be produced in a laboratory, the exact composition of this region is unknown and depends on the equation of state one adopts to describe it. Some of the more well-known candidates are

- A hyperonic matter component, i.e. nucleons containing a valence strange quark. These appear once the neutron chemical potential equals that of the  $\Lambda^0$  hyperon, with the  $\Xi^-$  appearing once its chemical potential equals the sum of the chemical potentials of the neutrons and electrons [176, 185].
- Pion/Kaon condensates. These are Bose-Einstein condensates of pion/kaon-like excitations [186–191].
- A quark-gluon plasma comprised of deconfined  $u$ ,  $d$  and  $s$  quarks and gluons [192–194].

#### 2.3.1 Observational Status

Unlike the WDs discussed above, there are significantly fewer NS observations to constrain the EoS. However, recent years have seen significant strides in furthering our understanding of matter at super-nuclear densities, both from a theory and observational standpoint. On the theoretical side, these advances come from developments in chiral EFT allowing more detailed modelling of nuclear interactions [195–197]. The observational data has been bolstered thanks to the onset of gravitational wave astronomy due to the LIGO-VIRGO experiment [198–200] and the launch of the Neutron star Interior Composition Explorer (NICER) X-ray timing instrument.

Ultimately, what is needed to further constrain the NS EoS are more precise observations of NS masses and radii, which can be obtained from various observational techniques. NS masses have historically been much easier to measure than their radii. In particular, masses of NSs in binary systems can be precisely determined as the underlying gravitational theories are well-understood today [178, 179, 201–203]. The radii must be determined by assuming the NSs emit a blackbody spectrum, however, this method is only reliable for cool NSs where the atmospheric models are well understood [203].

The NICER experiment can provide much more precise measurements of NS radii than previous methods. This is achieved by measuring the X-ray pulse profiles of pulsars, that are sensitive to how light bends around the star. This provides information on the compactness of the star,  $GM_*/R_*c^2$ , that can be used to determine

$M_\star$  and  $R_\star$  given that the mass can usually be determined through other means. The heaviest NS observed to date, the millisecond pulsar PSR J0740+6620 [204, 205], had its mass determined by measuring the relativistic Shapiro time delay [206]<sup>5</sup> of the radio signal, allowing the radius to be obtained once the compactness was measured [207]. Refined analyses result in a mass of  $2.08 \pm 0.07 M_\odot$  [208] and a radius of  $12.39^{+1.30}_{-0.98}$  km [205] or  $13.71^{+2.61}_{-1.50}$  km [204] at 68% confidence levels.

Gravitational wave astronomy offers an alternative and independent determination of NS masses and radii to the electromagnetic observations above. The best candidate events for this analysis are NS binary mergers, though these are expected to be an uncommon occurrence. As the NSs inspiral toward each other, they will begin to deform due to the tidal forces they induce on one another [209]. This deformation will alter the waveform observed at the detectors, with the shift in the phase of the waveform depending on the mass ratio,  $q = M_2/M_1 < 1$ , the chirp mass of the system,  $\mathcal{M}_{\text{chirp}} = (M_1 M_2)^{3/5}/(M_1 + M_2)^{1/5}$ , and a combination of the tidal deformabilities,  $\tilde{\Lambda}$ . The latter refers to how susceptible the star is to deformation due to tidal forces acting upon it, with larger values corresponding to less compact objects. Comparing the observed waveform to that determined from precise numerical simulations allows constraints to be placed on these parameters, and ultimately on the masses and radii of the merging NSs.

Furthermore, the electromagnetic emission from the remnant object provides information about the maximum mass an NS can achieve. If the mass of the remnant object is too large, it will collapse into a black hole, and it is highly unlikely that a gamma-ray burst will occur. If the remnant does not immediately collapse, then its mass and how it is rotating determines whether it will be hydrodynamically stable, unstable, or metastable against gravitational collapse. A remnant that undergoes differential rotation<sup>6</sup> can support heavier masses than one that is uniformly rotating. Hence, the afterglow spectrum can inform us as to how the star is rotating. Comparing the maximum mass supported by this rotation to the initial mass after inspiral yields an upper bound on the maximum NS mass achievable.

To date, the only confirmed NS-NS merger is the merger event GW170817 observed at LIGO-VIRGO in 2017 [199, 200], with the gamma-ray burst counterpart signal observed at the Fermi Gamma-ray Burst Monitor and INTEGRAL satellite [198]. These observations led to the constraint that the radius of a  $1.4 M_\odot$  NS has an upper bound of  $R_{1.4} < 13.3$  km [210, 211], and that the maximum NS mass must be  $M_{\text{NS}}^{\text{MAX}} < 2.18 M_\odot$  [198]. These constraints on the neutron star mass-radius relation are shown as the shaded turquoise and red regions of Fig 2.3.

---

<sup>5</sup>This refers to the time it takes for light to move out of a gravitational well taking longer than the naive Newtonian prediction due to the curvature of space-time.

<sup>6</sup>This is when components of the star at different latitudes have different angular velocities.

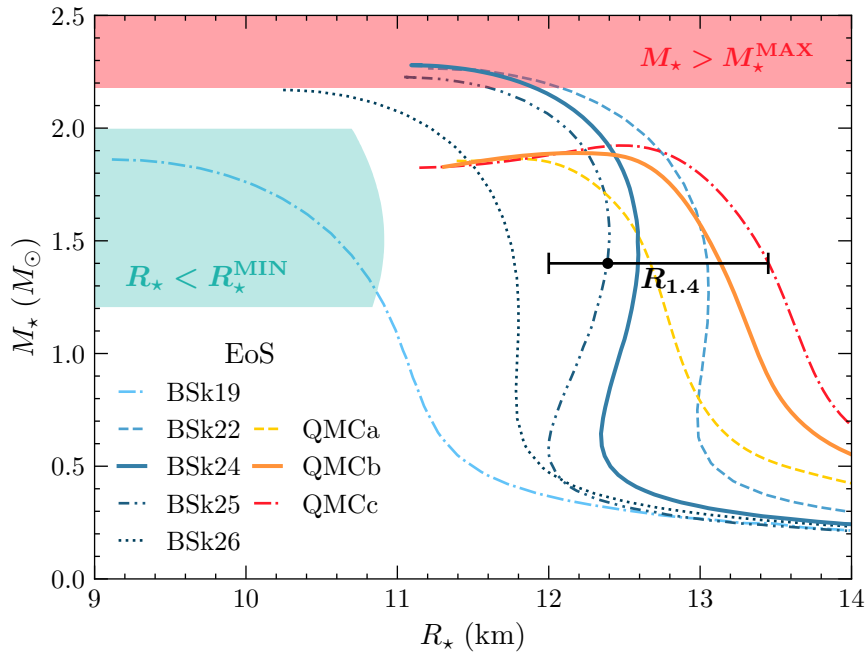


**Figure 2.3:** Neutron Star Mass-Radius relation predicted by the BSk (blue lines) and QMC (red lines) EoSs. Constraints obtained from the gravitational wave event GW170817 are shown as the shaded regions, with the lower bound on the radius in turquoise, and the maximum NS mass possible in red. The line band labeled  $R_{1.4}$  indicates the constraints on the radius of a  $1.4 M_\odot$  NS.

### 2.3.2 Neutron Star Equations of State

Given the scarce constraints that have been placed on the NS mass-radius relation, there are numerous equations of state in the literature that can be used to incorporate the internal structure into our calculations. In this work, we adopt two different EoSs, which we detail here.

#### The Brussels-Montreal EoS

The first family of EoSs adopted in this work are based on the Brussels-Montreal (BSk) energy density functionals [212–217], for cold, non-accreting NSs. In these models, the density-dependent nucleon interactions are accounted for via a mean-field approximation in either the Hartree-Fock (HF) or Hartree-Fock-Bogoliubov (HFB) formalism<sup>7</sup>, through effective Skyrme type forces [218, 219]. The BSk EoS family are unified EoSs, meaning they describe all the regions of the NS interior using the single effective Hamiltonian. Furthermore, the authors provide public FORTRAN subroutines that implement fits to the EoS quantities such as the pressure and density as functions of the baryon number density, allowing straightforward implementation of the EoS.

The authors provide these fits to eight configurations of the BSk EoS, labeled BSK19-26. Of these, the older BSK19-21 functionals were fitted to older atomic mass data that has since been updated in the newer models, BSk22-26. The mass-radius relation predicted by a selection of these models is shown in Fig. 2.3 by the blue lines. Missing are the BSk20 and 21 models, as they give very similar results to the 26 and 24 models respectively. The BSk19 EoS is partially ruled out from the lower bound on NS radii obtained from the electromagnetic counterpart of the GW170817 event [220], while BSk22 is ruled out from constraints on the tidal deformability from the same event [221]. Additionally, BSk22 does not support the presence of direct Urca<sup>8</sup> processes in NSs described by this EoS. These processes are required to explain observations of a small population of NSs that have cooled to temperatures below those predicted by the “minimal cooling paradigm” [222, 223]. On the other hand, the BSk26 functional predicts that all stable NSs will support direct Urac processes. This goes against the current observational evidence that a majority of NSs are well modeled by the minimal cooling paradigm, ruling the EoS out. Of the remaining two models, BSk24 and 25, we choose to adopt BSk24 as it gives slightly better fits to NS mass data than that of BSk25.

We use the BSk24 EoS to generate four benchmark NSs with masses of 1, 1.5, 1.9 and  $2.16 M_{\odot}$ , with the central density  $\rho_c$ , stellar mass, radius, metric factor

---

<sup>7</sup>The HF method accounts for the energy associated with nucleon pairings, while the HFB method neglects this contribution.

<sup>8</sup>This is another name given to the reactions in Eqs. 2.43, 2.44.

<b>EoS</b>	<b>BSk24-1</b>	<b>BSk24-2</b>	<b>BSk24-3</b>	<b>BSk24-4</b>
$\rho_c$ [g cm $^{-3}$ ]	$5.94 \times 10^{14}$	$7.76 \times 10^{14}$	$1.04 \times 10^{15}$	$1.42 \times 10^{15}$
$M_\star$ [ $M_\odot$ ]	1.000	1.500	1.900	2.160
$R_\star$ [km]	12.215	12.593	12.419	11.965
$B(R_\star)$	0.763	0.648	0.548	0.467
$c_s(0)$ [c]	0.511	0.628	0.734	0.835

**Table 2.2:** Benchmark NSs, for four different configurations of the equations of state (EoS) for cold non-accreting neutron stars with Brussels–Montreal functionals BSk24 [217]. EoS configurations are determined by the central mass-energy density  $\rho_c$ .

$B(R_\star)$  and central speed of sound  $c_s(0)$  in Table 2.2. Radial profiles of the baryon number density  $n_b(r)$ , metric factor  $B(r)$ , neutron chemical potential  $\varepsilon_{F,n}(r)$ , and neutron abundance  $Y_n(r)$ , are shown in Fig. 2.4.

While BSk24 and 25 lie well within current observational constraints, they are minimal models in that they only account for  $npe\mu$  matter, and do not incorporate any exotic species within the NS core. This is problematic as it is highly likely that hyperonic matter will appear in the cores of NS heavier than  $\sim 1.7 M_\odot$ . Additionally, the Skyrme forces that describe the nuclear interaction are treated non-relativistically, while the nucleons in heavier stars can become semi-relativistic. To address these concerns, later works [224, 225] adopted the Quark-Meson Coupling (QMC) EoS.

### The Quark-Meson Coupling EoS

The second EoS adopted is based on the QMC model of Refs. [226–229], in which baryons are described as bags of three valence quarks, with the bags themselves modeled by the MIT bag model [230]. The interactions among the baryons are described by the exchange of mesons between the valence non-strange quarks and are formulated within a relativistic mean-field Lagrangian. The exchange of the vector mesons acts as an overall shift to the energy of the baryons<sup>9</sup>. The scalar mean fields play a significantly more important role, modifying the effective mass of the baryons. The scalar (and also vector) couplings are density-dependent, leading to an effective mass of the baryons that varies throughout the NS. The density dependence of these couplings is equivalent to including repulsive three-body forces

---

<sup>9</sup>A simple analogy for this is how the force of an electron in an electromagnetic field is due to the exchange of photons, which are vector fields. The total energy of the electron is a shift relative to the free electron energy.

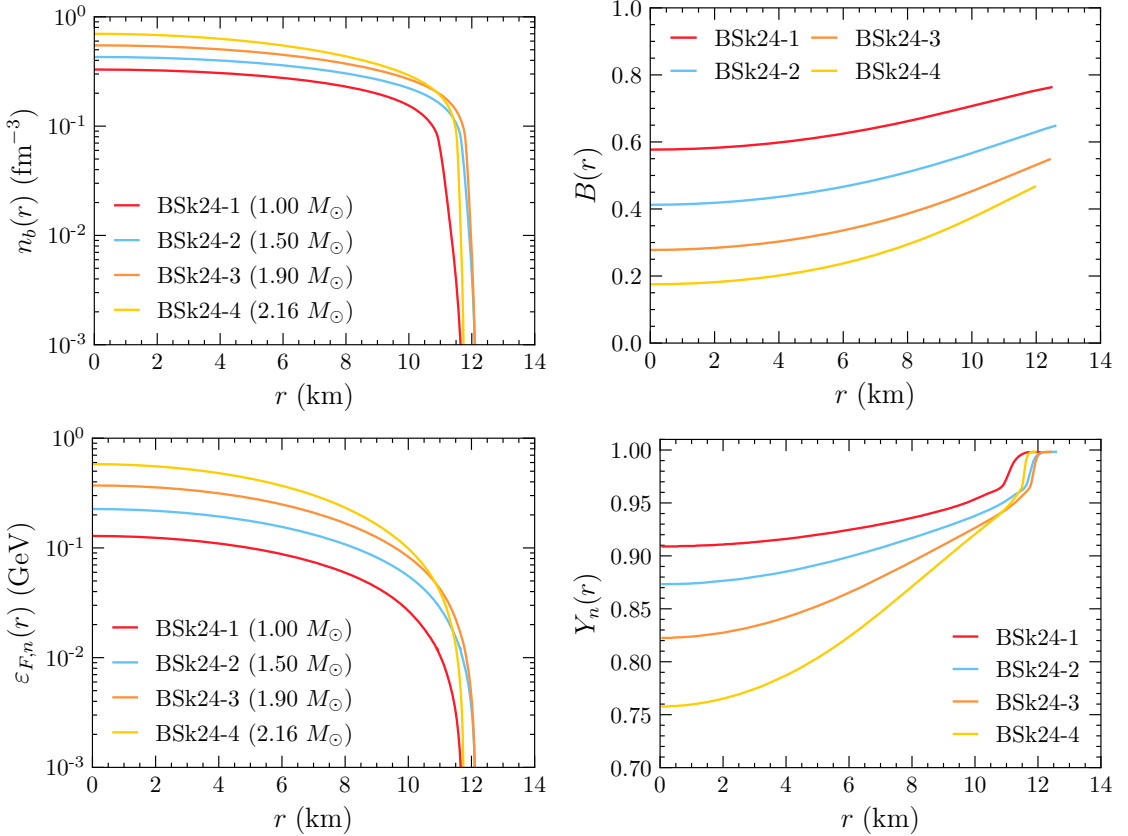


**Figure 2.4:** Radial profiles of the baryon number density (top left), metric factor  $B(r)$  (top right), neutron chemical potential (bottom left), and neutron abundance (bottom right) for the four benchmark NS of the BSk24 EoS in Table 2.2.

EoS	QMC-1	QMC-2	QMC-3	QMC-4
$n_B^c \text{ [fm}^{-3}\text{]}$	0.325	0.447	0.540	0.872
$M_\star \text{ [M}_\odot\text{]}$	1.000	1.500	1.750	1.900
$R_\star \text{ [km]}$	13.044	12.847	12.611	12.109
$B(R_\star)$	0.772	0.653	0.588	0.535

**Table 2.3:** Benchmark NSs for four different configurations of the QMC equation of state. EoS configurations are determined by the central number density  $n_B^c$ .

between the baryons and arises naturally in the QMC model through the in-medium modification of the baryonic structure [231, 232]. Additional details on the energy density and couplings of the QMC model adopted in this work are given in Appendix ??.

The mass-radius relation of three different configurations of the QMC EoS, namely three different choices of the isovector coupling constant, are shown as the red lines in Fig. 2.3, obtained from Ref. [233]. Of these, QMCb (orange solid line in Fig. 2.3) lies within the constraints on the radius of a  $1.4 M_\odot$  NS from GW170817, and can produce an NS of mass  $1.908 \pm 0.016 M_\odot$ , the currently preferred mass of PSR J1614-2230 obtained by the NANOGrav collaboration [234]<sup>10</sup>.

The QMCb EoS data was provided by the authors of Ref. [233] for use in this work and will be referred to as simply the QMC EoS from here on. From this, we calculate the internal structure of four benchmark QMC NSs, similar to the BSk models of Table 2.2, with the central baryon density replacing the central density and the speed of sound omitted. The relevant parameters are shown in Table 2.3. The top four plots in Fig. 2.5 show the radial profiles for the number densities of the neutrons and protons for each configuration on the left, with their effective masses shown on the right. The bottom two plots of the same figure show the number densities for each species within the heaviest star on the left, including leptons in dashed lines, with the effective masses for each of the baryons on the right. The replacement of high-momentum neutrons with low-momentum hyperons is clearly seen in the bottom left plot, as the neutron number density dips towards the centre of the massive star. As the densities are high enough for the charged hyperon  $\Xi^-$  to appear, the abundance of leptons decreases due to the requirement of charge neutrality, also seen in this plot.

---

<sup>10</sup>As mentioned above, the current heaviest NS has a mass of  $2.08 \pm 0.07 M_\odot$  though the implications of this on the QMC EoS are beyond the scope of this work.

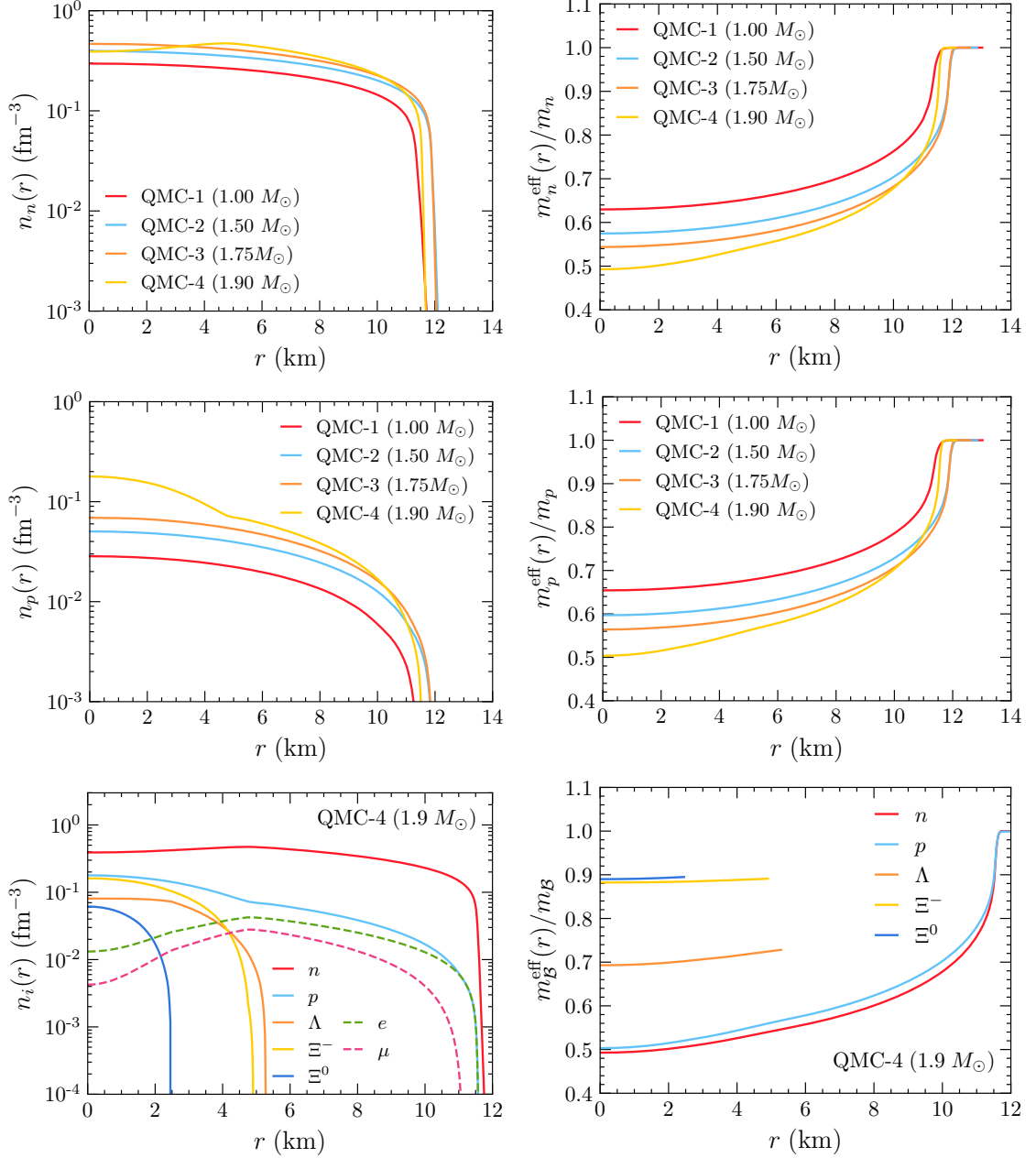


**Figure 2.5:** Number density profiles (left) and the ratio of the effective mass to the bare mass (right) for neutrons (top) and protons (middle) for benchmark configurations of the QMC EoS in Table 2.3. In the bottom panels, we show the same profiles for all species in the heaviest NS considered, QMC-4, which contains hyperonic matter.

# 3

## Improved Treatment of Dark Matter Capture in Compact Objects

*This chapter combines aspects of Refs. [224, 235, 236] to give a complete introduction to the formalism we have built for dark matter capture in compact objects. We begin by reviewing aspects of Gould’s formalism for capture in the Sun [97, 98]. We then build upon these results to incorporate relativistic corrections and the effects of Pauli Blocking due to scattering from a degenerate media in a self-consistent manner. Important aspects of both the interaction and capture rates are discussed, including Pauli blocking for low mass DM and the effects of multiple scattering in the high-mass regime. We then apply our results to the example DM scattering from neutron targets using the BSk24 EoS to model the neutron star.*

### 3.1 Dark Matter Capture in the Sun

Before jumping into the capture formalism relevant to compact objects, it will serve us well to review the formalism laid out by Gould for capture in the Sun [97, 98].

To begin, we consider the flux of dark matter particles that pass through a spherical shell a large distance  $R$  from the star, where the gravitational field is negligible. For this, we need to know the distribution function of the relative velocity between the DM and the stellar constituents. The velocity distribution function will be spatially isotropic, and so for simplicity we will assume that the

DM follows a Maxwell-Boltzmann distribution function,

$$f_\infty(\tilde{u}_\chi)d\tilde{u}_\chi = 4\pi \left( \frac{3}{2\pi} \right)^{3/2} \frac{\tilde{u}_\chi^2}{v_d^2} \exp\left(-\frac{3\tilde{u}_\chi^2}{2v_d^3}\right) d\tilde{u}_\chi, \quad (3.1)$$

where  $\tilde{u}_\chi$  is the DM velocity in the halo, and  $v_d$  is the DM halo velocity dispersion.

Taking into account the motion of the star through the halo and the thermal motion of the constituents, which are assumed to follow a Maxwell-Boltzmann distribution, gives the relative velocity between the DM and targets,  $u_\chi$ . The distribution function for the relative velocity can be expressed as [99]

$$f_{\text{MB}}(u_\chi, T_\star)du_\chi = \frac{u_\chi}{v_\star} \sqrt{\frac{3}{2\pi(v_d^2 + 3T_\star/m_i)}} \left( e^{-\frac{3(u_\chi - v_\star)^2}{2(v_d^2 + 3T_\star/m_i)}} - e^{-\frac{3(u_\chi + v_\star)^2}{2(v_d^2 + 3T_\star/m_i)}} \right) du_\chi, \quad (3.2)$$

where  $v_\star$  is the star's velocity in the halo rest frame<sup>1</sup>,  $T_\star$  is the temperature of the star, and  $m_i$  is the mass of the target.

Returning to the large spherical shell of radius  $R$ , given the velocity distribution function, we can obtain the flux of DM through this surface. The rate of DM particles passing through a surface element  $d\tilde{A}$  with velocity between  $u_\chi$  and  $u_\chi + du_\chi$ , with an angle to the normal of  $d\tilde{A}$  between  $\tilde{\theta}$  and  $\tilde{\theta} + d\tilde{\theta}$  and an azimuthal angle between  $\tilde{\phi}$  and  $\tilde{\phi} + d\tilde{\phi}$  is given by [96]

$$\frac{dN_\chi}{dt} = \frac{\rho_\chi}{m_\chi} f_{\text{MB}}(u_\chi, T_\star) \vec{u} \cdot d\vec{\tilde{A}} du_\chi \frac{d\tilde{\Omega}}{4\pi} \quad (3.3)$$

$$= \frac{\rho_\chi}{m_\chi} f_{\text{MB}}(u_\chi, T_\star) u_\chi \cos \tilde{\theta} d\tilde{A} du_\chi \frac{d\cos \tilde{\theta} d\tilde{\phi}}{4\pi} \quad (3.4)$$

$$= \frac{1}{4} \frac{\rho_\chi}{m_\chi} f_{\text{MB}}(u_\chi, T_\star) u_\chi d\tilde{A} du_\chi d\cos^2 \tilde{\theta}, \quad (3.5)$$

where we have integrated over the azimuthal angle  $\tilde{\phi}$  due to the isotropy of the system. The number density of the DM is included through the  $\rho_\chi/m_\chi$  factor. Integrating over the area of the sphere is trivial due to isotropy, leaving us with

$$\frac{dN_\chi}{dt} = \pi \frac{\rho_\chi}{m_\chi} f(u_\chi, T_\star) u_\chi du_\chi d\cos^2 \tilde{\theta}, \quad (3.6)$$

with the integration interval for  $\cos^2 \tilde{\theta}$  being  $(0, 1)$ .

---

<sup>1</sup>This is the frame where the DM has an average velocity of zero.

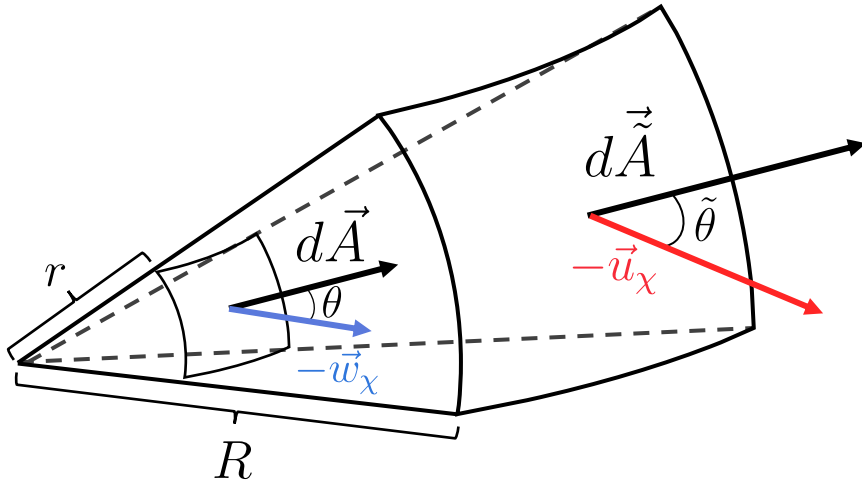


**Figure 3.1:** Geometry of the capture process, showing two elements of spheres with radii  $r$  close to the star

As the DM begins to infall from this large distance  $R$  to a closer distance  $r$ , the star's gravitational field will boost the velocity by the local escape velocity  $v_e(r)$  such that

$$w_\chi^2(r) = u_\chi^2 + v_e^2(r), \quad (3.7)$$

$$v_e^2(r) = \frac{2GM_\star}{R_\star} + \int_r^{R_\star} \frac{GM_\star(r')}{r'^2} dr'. \quad (3.8)$$

Due to the conservation of angular momentum, we can relate the angular momentum of the DM at the two distances  $R$  and  $r$  such that

$$J_\chi = m_\chi Ru_\chi \sin \tilde{\theta} = m_\chi rw_\chi(r) \sin \theta \leq m_\chi rw_\chi(r) \equiv J_{\max}, \quad (3.9)$$

where  $\theta$  is the incident angle of the DM at the closer distance  $r$ , and we have defined the maximum angular momentum  $J_{\max}$  corresponding to a linear DM trajectory.

Changing integration variables from  $\cos^2 \tilde{\theta}$  to  $J_\chi$  allows us to write the number of DM particles passing through the shell per unit volume as

$$\frac{dN_\chi}{dt} = 2\pi \frac{\rho_\chi}{m_\chi} \frac{f_{\text{MB}}(u_\chi, T_\star)}{u_\chi} r^2 w_\chi^2(r) \frac{J_\chi dJ_\chi}{J_{\max}^2} du_\chi. \quad (3.10)$$

The geometry of the system is shown in Fig. 3.1 for clarity.

The probability that the DM interacts with the constituents of the shell depends on the interaction rate,  $\Omega(w_\chi)$ , multiplied by the time spent in the shell,  $dt = dr/\dot{r}$ . Hence, the probability of scattering within the shell is

$$\Omega(w_\chi) \frac{dr}{\dot{r}} = 2\Omega(w_\chi) \frac{1}{w_\chi} \left(1 - \left(\frac{J_\chi}{rw_\chi}\right)^2\right)^{-1/2} \Theta(J_{\max} - J_\chi) dr, \quad (3.11)$$

where the factor of 2 is due to the DM having two opportunities to pass through the shell, once when incoming and another after turning around<sup>2</sup>. The step-function is put in to ensure the angular momentum does not exceed its maximum allowed value.

For a scattered DM to be considered captured, it must lose enough energy in the collision to become gravitationally bound. The rate at which a DM particle scatters from an initial velocity  $w_\chi$  to a final velocity  $v < v_e(r)$  is given by [97–99]

$$\Omega^-(w_\chi) = \int_0^{v_e} R^-(w_\chi \rightarrow v) dv, \quad (3.12)$$

$$R^-(w_\chi \rightarrow v) = \int n_T(r) \frac{d\sigma_{\chi T}}{dv} |\vec{w}_\chi - \vec{u}_T| f_T(u_T) d^3 \vec{u}_T, \quad (3.13)$$

with  $R^-(w_\chi \rightarrow v)$  being the differential interaction rate,  $n_T$  is the target number density,  $u_T$  is the target velocity and  $f_T(u_T)$  is the corresponding distribution function, and  $d\sigma_{\chi T}/dv$  is the differential cross-section. The minus superscript is used to signify that this is the down scattering rate, i.e. the rate of interactions leading to the DM losing energy.

Finally, we obtain the capture rate by multiplying Eqs. 3.10 and 3.11 and integrate over the angular momentum to give the result

$$C = \int_0^{R_*} dr 4\pi r^2 \int_0^\infty du_\chi \frac{\rho_\chi}{m_\chi} \frac{f_{\text{MB}}(u_\chi, T_*)}{u_\chi} w_\chi(r) \Omega^-(w_\chi). \quad (3.14)$$

This result is rather generic, as the choice of DM model will only dictate the form of the differential cross-section in Eq. 3.13. As written above, the distribution function for the relative velocity far from the star can be any isotropic distribution function. The MB form was chosen as it allows for a simple analytic form of the total capture rate.

---

<sup>2</sup>The radial velocity  $\dot{r}$  is a standard result in orbital mechanics and can be obtained from the central force Lagrangian.

## 3.2 Capture in Compact Objects

Having reviewed the capture process in non-relativistic stars, we can begin discussing the necessary modifications required when considering relativistic stars. In this section, we consider the two major modifications that need to be made:

- The corrections from General Relativity due to the extreme gravitational fields. This ultimately alters the flux of DM passing through the star, boosting it through gravitational focusing.
- Accounting for the relativistic and degenerate nature of the star's constituents in the interaction rate.

The former is generic to neutron stars and white dwarfs, while the latter is required for all NS constituents, but only the electrons in a WD are degenerate and relativistic. The ions of the WD are non-relativistic and non-degenerate and, hence, can the solar capture formalism can be applied in this case.

### 3.2.1 General Relativistic Corrections to the Capture Rate

Far from the star, the physics is the same as in the previous section. The deviations arise as the DM falls into the gravitational potential of the star. We begin by following the DM along its trajectory, moving from a distance  $R \gg R_\star$  to a closer distance  $r$ . Hence, we are working in the DM rest frame and calculating the rate at which the DM passes through the shell *per unit of proper time*,  $\tau$ . The proper time interval is related to the metric through

$$d\tau^2 = B(r)dt^2 - A(r)dr^2 - r^2d\Omega^2, \quad (3.15)$$

with  $B(r)$  and  $A(r)$  defined in Chapter 2.

Following the same arguments as in the non-relativistic case, the flux of DM passing through the shell is

$$\frac{dN_\chi}{d\tau} = 2\pi \frac{\rho_\chi}{m_\chi} \frac{f_{\text{MB}}(u_\chi)}{u_\chi} du_\chi \frac{J_\chi dJ_\chi}{m_\chi^2}, \quad (3.16)$$

which takes the same form as Eq. 3.10, with the physical difference being that this is the rate with respect to the proper time. Additionally, as we will be considering cold stars, we take the  $T_\star \rightarrow 0$  limit of the DM-target relative velocity distribution, such that

$$f_{\text{MB}}(u_\chi) = \lim_{T_\star \rightarrow 0} f_{\text{MB}}(u_\chi, T_\star) \quad (3.17)$$

$$= \frac{u_\chi}{v_\star} \sqrt{\frac{3}{2\pi(v_d^2 + 3T_\star/m_i)}} \left( e^{-\frac{3(u_\chi - v_\star)^2}{2(v_d^2 + 3T_\star/m_i)}} - e^{-\frac{3(u_\chi + v_\star)^2}{2(v_d^2 + 3T_\star/m_i)}} \right), \quad (3.18)$$

The probability that DM scatters within the shell and is captured is  $2\hat{\Omega}^-(r)d\tau$ , where  $\hat{\Omega}^-(r)$  is the interaction rate with respect to the proper time, and  $d\tau$  is the proper time taken to move from coordinate  $r$  to  $r + dr$ . The factor of 2 once again accounts for the DM crossing the shell twice per orbit. For calculation purposes, we need to relate this to the interaction rate seen by a distant observer,  $\Omega^-(r)$ , that is done through

$$\hat{\Omega}^-(r)d\tau = \frac{1}{\sqrt{g_{tt}}}\Omega^-(r)d\tau = \frac{1}{\sqrt{B(r)}}\Omega^-(r)d\tau. \quad (3.19)$$

Now, the proper time that the DM spends inside a shell of thickness  $dr$  will be<sup>3</sup>

$$d\tau = \left(\frac{d\tau}{dt}\right)dt = B(r)\frac{dr}{\dot{r}} = \frac{\sqrt{B(r)}dr}{\sqrt{\frac{1}{A(r)}\left[1 - B(r)\left(1 + \frac{J_\chi^2}{m_\chi^2 r^2}\right)\right]}}. \quad (3.20)$$

The differential capture rate can then be written as

$$dC = 2\pi \frac{\rho_\chi}{m_\chi} \frac{f_{\text{MB}}(u_\chi)}{u_\chi} du_\chi \frac{dJ_\chi^2}{m_\chi^2} \frac{\Omega^-(r)\sqrt{A(r)}dr}{\sqrt{1 - B(r)\left(1 + \frac{J_\chi^2}{m_\chi^2 r^2}\right)}}. \quad (3.21)$$

As the total number of targets in the star,  $N_T$ , needs to satisfy

$$N_T = \int_0^{R_*} 4\pi r^2 n_T(r) \sqrt{A(r)} dr, \quad (3.22)$$

where  $n_T(r)$  is the number density that appears in the interaction rate, we absorb the factor  $\sqrt{A(r)}$  into the definition of  $n_T(r)$ , such that  $\Omega^-(r)\sqrt{A(r)} \rightarrow \Omega^-(r)$ . This is due to the number densities obtained by solving the TOV equations already account for the  $\sqrt{A(r)}$  factor.

As before, we have  $w_\chi^2(r) = u_\chi^2 + v_e^2(r)$ , however as the escape velocity will be significantly larger than the ambient DM velocity far from the star, we can safely approximate  $w_\chi^2(r) \approx v_e^2(r)$ . In the relativistic case, the escape velocity can be defined as

$$v_e^2(r) = \left(\frac{dl}{d\tau}\right)^2 = A(r) \left(\frac{dr}{d\tau}\right)^2 + r^2 \left(\frac{d\phi}{d\tau}\right)^2 = 1 - B(r), \quad (3.23)$$

where  $dl$  is a length element. The large boost from the escape velocity also removes the  $u_\chi$  dependence in the kinematics of the interactions and allows us to perform the integration over the initial DM velocity, yielding an overall factor of

$$\int_0^\infty \frac{f_{\text{MB}}(u_\chi)}{u_\chi} du_\chi = \frac{1}{v_*} \text{Erf}\left(\sqrt{\frac{3}{2}} \frac{v_*}{v_d}\right). \quad (3.24)$$

---

<sup>3</sup>See Appendix ?? for the derivation of  $\dot{r} = \frac{dr}{dt}$ .

To integrate over  $J_\chi^2$ , we need the maximum angular momentum the DM can achieve as it passes through the shell. This can be obtained by requiring the argument of the radical above to remain positive, giving

$$J_{\max} = \sqrt{\frac{1 - B(r)}{B(r)}} m_\chi r. \quad (3.25)$$

The factor of  $1/\sqrt{B}$  arises due to the gravitational focusing of the incoming flux of DM [237].

Putting everything together, and integrating over the radius of the star, we are left with the final result for the capture rate of

$$C = \frac{4\pi}{v_\star} \frac{\rho_\chi}{m_\chi} \text{Erf} \left( \sqrt{\frac{3}{2}} \frac{v_\star}{v_d} \right) \int_0^{R_\star} r^2 \frac{\sqrt{1 - B(r)}}{B(r)} \Omega^-(r) dr. \quad (3.26)$$

All that remains is determining the form of the interaction rates for relativistic energies.

### 3.2.2 Geometric Limit and Threshold Cross-Section

In the previous section, we derived an expression for the capture rate assuming that the DM is captured after a single scatter, and that it only scatters once along its orbit through the NS. This first assumption is true for DM light enough to lose enough energy in this single interaction, which for nucleon targets turns out to be  $m_\chi \lesssim 10^6$  GeV. The latter assumption is a statement that we are working in the optically thin regime, such that the cross-section is much less than the “threshold cross-section”,  $\sigma_{\text{th}}$ . The value of the threshold cross-section is defined as the cross-section for which the capture rate evaluated in the optically thin regime is equal to the geometric limit [132],

$$C_{\text{geom}} = \frac{\pi R_\star^2 (1 - B(R_\star))}{v_\star B(R_\star)} \frac{\rho_\chi}{m_\chi} \text{Erf} \left( \sqrt{\frac{3}{2}} \frac{v_\star}{v_d} \right). \quad (3.27)$$

This is the capture rate for which the entire flux of DM passing through the surface of the star is captured at the surface. Hence, it serves as an upper bound to the capture rate, with cross-sections greater than  $\sigma_{\text{th}}$  saturating the capture rate to this value. Note the  $1/B(R_\star)$  factor in the equation above. In stars and planets where classical Newtonian mechanics can be applied, gravitational focusing would result in a factor  $v_{\text{esc}}^2/v_\star = (1 - B(R_\star))/v_\star$  in Eq. 3.27, where we have used Eqs. 3.23 and 2.14. In neutron stars, on the other hand, general relativity introduces an

additional factor of  $1/B(R_\star)$ , which can be obtained from the derivation of the flux of DM particles accreted to a NS with a Schwarzschild metric (Eq. 3.26) [237, 238].

For scattering on neutrons, the threshold cross-section is approximately

$$\sigma_{th} = \begin{cases} \sigma_{\text{ref}} \frac{\text{GeV}}{m_\chi}, & m_\chi \lesssim 1 \text{ GeV} \quad (\text{Pauli blocking regime}), \\ \sigma_{\text{ref}}, & 1 \text{ GeV} \lesssim m_\chi \lesssim 10^6 \text{ GeV}, \\ \sigma_{\text{ref}} \frac{m_\chi}{10^6 \text{ GeV}}, & m_\chi \gtrsim 10^6 \text{ GeV} \quad (\text{Multiscattering regime}), \end{cases} \quad (3.28)$$

where we take the canonical value of

$$\sigma_{\text{ref}} \sim 1.7 \times 10^{-45} \text{ cm}^2, \quad (3.29)$$

which assumes the NS is a solid sphere such that  $\sigma_{\text{ref}} \sim m_n \pi R_\star^2 / M_\star$  with  $m_n$  the neutron mass.

For scattering off other targets, Pauli blocking is relevant for  $q_0^{\text{MAX}} \lesssim \mu_{\text{target}}$  while multi-scattering is relevant for  $m_\chi \gtrsim q_0^{\text{MAX}} / v_\star^2$ , where  $q_0^{\text{MAX}}$  is the maximum energy transferred in a collision, as will be discussed later. In addition, because the other target species have a lower abundance than neutrons, the reference cross-section,  $\sigma_{\text{ref}}$ , will be higher. The values of  $\sigma_{th}$  in Eq. 3.28, and their regions of applicability, can thus be altered appropriately for other target species of interest.

### 3.2.3 Interaction Rate for Relativistic Energies and Degenerate Targets

Our next goal is to write down an interaction rate suitable for describing the interactions between relativistic particles and account for the degeneracy of the target species. This will be achieved by modifying the non-relativistic interaction rate of Eq. 3.12 through the use of relativistic kinematics and the use of Lorentz invariant quantities, and the correct distribution functions for degenerate fermion targets.

As shown in Eqs. 3.12 and 3.13, the interaction rate between non-relativistic, non-degenerate species  $i$  can be expressed as

$$\Omega^-(r) = \int dv \frac{d\sigma}{dv} |\vec{w}_\chi - \vec{u}_i| n_i(r) f_{\text{MB}}(u_i) d^3 u_i. \quad (3.30)$$

First, we address the degeneracy of the targets by exchanging the Maxwell-Boltzmann distribution function for a Fermi-Dirac (FD) distribution,  $f_{\text{FD}}(E_i, r)$ , via the replacement

$$n_i(r) f_{\text{MB}}(u_i) d^3 u_i \rightarrow \frac{g_s}{(2\pi)^3} f_{\text{FD}}(E_i, r), \quad (3.31)$$

where  $g_s = 2$  is the number of spin states of the target species,  $p$  is the 3-momentum of the incoming target, and  $E_i$  is its corresponding energy. The radial dependence of the FD distribution stems from its implicit dependence on the chemical potential of the target. Rewriting this expression in a more computationally friendly manner in terms of the relevant kinematic quantities results in

$$\frac{g_s}{(2\pi)^3} f_{\text{FD}}(E_i, r) = \frac{p E_i}{2\pi^2} f_{\text{FD}}(E_i, r) dE_i d\cos\theta_{uw}, \quad (3.32)$$

where we have expressed the angular component of the  $d^3p$  differential in terms of the angle between the incoming DM and target. This angle can be traded for the more useful quantity  $s$ , the centre of mass energy through

$$\frac{d\cos\theta_{uw}}{ds} = \frac{1}{2pp_\chi} = \frac{1}{2p\sqrt{E_\chi^2 - m_\chi^2}} = \frac{1}{2pm_\chi} \sqrt{\frac{B(r)}{1 - B(r)}}, \quad (3.33)$$

as the initial DM energy is  $E_\chi = m_\chi/\sqrt{B(r)}$ .

Next, we calculate the initial relative velocity,  $|\vec{w}_\chi - \vec{u}_i|$ , using relativistic kinematics, expressing it in terms of the Mandelstam  $s$ ,

$$|\vec{w}_\chi - \vec{u}_i| = \frac{\sqrt{s^2 - 2s(1 + \mu^2)m_i^2 + (1 - \mu^2)^2m_i^4}}{s - (1 + \mu^2)m_i^2}, \quad (3.34)$$

where  $\mu = m_\chi/m_i$ .

Given that it is most common to present the relativistic differential scattering cross-section  $d\sigma/d\cos\theta_{\text{cm}}$  as a function of the Mandelstam variables  $s$  and  $t$ , with  $\theta_{\text{cm}}$  the centre of mass frame scattering angle, we make the replacement

$$dv \frac{d\sigma}{dv} = dt \frac{d\sigma}{dt} = dt \frac{d\sigma}{d\cos\theta_{\text{cm}}} \frac{d\cos\theta_{\text{cm}}}{t}. \quad (3.35)$$

The final Jacobian factor can be expressed as

$$\frac{d\cos\theta_{\text{cm}}}{dt} = \frac{2s}{s^2 - 2s(1 + \mu^2)m_i^2 + (1 - \mu^2)^2m_i^4}, \quad (3.36)$$

for the elastic scattering we consider here.

Finally, we note that the first application of this capture formalism was for neutron targets, with the analysis completed before we had considered the additional effects from the form factors and strong interactions discussed in subSection 1.2.4. These effects will be incorporated into this formalism in a self-consistent way next chapter. The initial approach that was taken to account for the fact that we are

using realistic neutron number density profiles, despite the expression in Eq. 3.31 being for a free Fermi gas, is to introduce a correction factor as in Ref. [116],

$$\zeta(r) = \frac{n_i(r)}{n_{\text{free}}(r)}, \quad (3.37)$$

where  $n_{\text{free}}(r)$  is obtained by integrating Eq. 3.32 over all phase space. In the zero-temperature approximation, the result is

$$n_{\text{free}}(r) = \frac{1}{3\pi^2} [\varepsilon_{F,i}(r)(2m_i + \varepsilon_{F,i}(r))]^{3/2}. \quad (3.38)$$

Compiling everything together leads to the final expression for the interaction rate being

$$\Omega^-(r) = \int dt dE_i ds \zeta(r) \frac{d\sigma}{d \cos \theta_{\text{cm}}} \frac{E_i}{2\pi^2 m_i} \sqrt{\frac{B(r)}{1 - B(r)}} \frac{s}{\beta(s)\gamma(s)} \times f_{\text{FD}}(E_i, r)(1 - f_{\text{FD}}(E'_i, r)), \quad (3.39)$$

where we have introduced the helper functions

$$\beta(s) = s - (m_i^2 + m_\chi^2), \quad (3.40)$$

$$\gamma(s) = \sqrt{\beta^2(s) - 4m_i^2 m_\chi^2}. \quad (3.41)$$

We have also introduced the Pauli blocking factor,  $1 - f_{\text{FD}}(E'_i, r)$ , to account for the phase space available to the final state target. The energy of this final state particle,  $E'_i$ , is in general a messy function of  $E_i$ ,  $t$ ,  $s$ , and  $r$ , and can be obtained from the kinematics of the scattering. This result is presented in Appendix ??.

The integration intervals are

$$t_{\min} = -\frac{\gamma(s)}{s}, \quad (3.42)$$

$$t_{\max} = 0, \quad (3.43)$$

$$s_{\min} = m_i^2 + m_\chi^2 + 2\frac{E_i m_\chi}{\sqrt{B(r)}} - 2m_\chi \sqrt{\frac{1 - B(r)}{B(r)}} \sqrt{E_i^2 - m_i^2}, \quad (3.44)$$

$$s_{\max} = m_i^2 + m_\chi^2 + 2\frac{E_i m_\chi}{\sqrt{B(r)}} + 2m_\chi \sqrt{\frac{1 - B(r)}{B(r)}} \sqrt{E_i^2 - m_i^2}, \quad (3.45)$$

$$E_{i,\min} = m_i, \quad (3.46)$$

$$E_{i,\max} = \frac{m_i}{\sqrt{B(r)}}. \quad (3.47)$$

As we will be dealing with NSs at low temperatures, we can take the  $T_\star \rightarrow 0$  limit and replace the FD functions with step functions,

$$f_{\text{FD}}(E_i, r) \rightarrow \Theta(\varepsilon_{F,i}(r) + m_i - E_i), \quad (3.48)$$

$$1 - f_{\text{FD}}(E'_i, r) \rightarrow \Theta(E'_i - m_i - \varepsilon_{F,i}(r)). \quad (3.49)$$

The first step function can be used to further restrict the  $E_i$  integration interval to be  $[m_i, m_i + \varepsilon_{F,i}(r)]$ . In practice, we work with the kinetic energies of the targets rather than their total energy, as this is the quantity that directly changed in the interactions. Therefore, unless otherwise specified, we will take  $E_i$  to mean the target kinetic energy, with the integration range being  $0 \leq E_i \leq \varepsilon_{F,i}$ .

This expression resembles that of Ref. [116], but uses a relativistic formalism instead. In Appendix A.3, we show that Eq. 3.39 reduces to the classical expression for the interaction rate in the non-relativistic limit.

### 3.3 The Differential Interaction Rate

In the previous section, we have calculated the interaction rate,  $\Omega^-(r)$ , assuming the initial DM energy takes its pre-capture value,  $E_\chi = m_\chi/B(r)$ . However, we are also interested in an expression for the interaction rate valid for arbitrary DM energy. This will be required when we consider capture via multiple scatterings, and it will also be necessary to study the subsequent scattering interactions that follow capture and lead to the DM thermalising within the NS. In principle, it is possible to calculate this rate numerically by binning  $\Omega^-$ , Eq. 3.39, in the energy loss, i.e. multiplying  $\Omega^-$  by  $\frac{1}{E_i - E_j} \Theta(E_i + E_i - E'_i) \Theta(E'_i - E_i - E_j)$  and integrating over the bin  $[E_j, E_i]$ . However, it is possible to derive analytic expressions for the differential rate, valid in the zero-temperature approximation. To do so, we use the definition of the scattering rate in Ref. [118, 239]

$$\begin{aligned} \Gamma^-(E_\chi) = 2 \int \frac{d^3 k'}{(2\pi)^3} \int \frac{d^3 p}{(2\pi)^3} \int \frac{d^3 p'}{(2\pi)^3} \frac{|\bar{\mathcal{M}}|^2}{(2E_\chi)(2E'_\chi)(2E_i)(2E'_i)} \\ \times (2\pi)^4 \delta^4(k_\mu + p_\mu - k'_\mu - p'_\mu) f_{\text{FD}}(E_i)(1 - f_{\text{FD}}(E'_i)), \end{aligned} \quad (3.50)$$

where  $|\bar{\mathcal{M}}|^2$  is the squared matrix element,  $k^\mu = (E_\chi, \vec{k})$  and  $k'^\mu = (E'_\chi, \vec{k}')$  are the DM initial and final momenta, and  $p^\mu = (E_i, \vec{p})$  and  $p'^\mu = (E'_i, \vec{p}')$  are the target particle initial and final momenta, respectively. To see that  $\Gamma^-$  is indeed the same as  $\Omega^-$  in Eq. 3.39, multiply and divide by  $v_{\text{rel}} = |\vec{w} - \vec{u}_i|$  to reintroduce the quantum

field theoretic definition of differential cross-section,

$$d\sigma = \frac{|\mathcal{M}|^2}{2E_\chi 2E_i |\vec{w} - \vec{u}_i|} d^2\Pi_{\text{LIPS}}, \quad (3.51)$$

$$d^2\Pi_{\text{LIPS}} = \frac{1}{2E'_\chi} \frac{d^3k'}{(2\pi)^3} \frac{1}{2E'_i} \frac{d^3p'}{(2\pi)^3} (2\pi)^4 \delta^4(k_\mu + p_\mu - k'_\mu - p'_\mu), \quad (3.52)$$

$$\implies \frac{d\sigma}{d\cos\theta_{\text{cm}}} = \frac{1}{16\pi} \frac{\beta(s)}{2s\beta(s) - \gamma^2(s)} |\mathcal{M}|^2, \quad (3.53)$$

where  $d^2\Pi_{\text{LIPS}}$  is the 2-body Lorentz invariant phase space.

The advantage of Eq. 3.39 is that it can be used to calculate the capture rate for any interaction given the differential cross-section. The disadvantage is that this computation has to be evaluated numerically, which can be computationally intensive. For this reason, shall now use Eq. 3.50 to derive analytic expressions that will allow us to speed up computations and, in addition, calculate the shape of the interaction rate as a function of the energy loss.

The interaction rate for  $d\sigma \propto s^m t^n$  is

$$\begin{aligned} \Gamma^-(E_\chi) \propto & \sum_{n,m} \frac{(-1)^n}{128\pi^3 E_\chi k} \int_0^{E_\chi - m_\chi} dq_0 \int \frac{dt_E t_E^n}{(t_E + q_0^2)^{m+\frac{1}{2}}} \\ & \times \sum_{r=0}^m \mathcal{V}_{m,r} \sum_{j=0}^r \binom{r}{j} \varepsilon_{F,i}^{r-j} \frac{(-1)^j q_0^{j+1}}{j+1} h_j \left( \frac{E_i^{t^-} - \varepsilon_{F,i}}{q_0} \right), \end{aligned} \quad (3.54)$$

for elastic scattering with  $t_E = -t = q^2 - q_0^2$ , where  $q_0 = E'_i - E_i$  is the DM energy loss,

$$E_i^{t^-} = - \left( m_n + \frac{q_0}{2} \right) + \sqrt{\left( m_n + \frac{q_0}{2} \right)^2 + \left( \frac{\sqrt{q^2 - q_0^2}}{2} - \frac{m_n q_0}{\sqrt{q^2 - q_0^2}} \right)^2}, \quad (3.55)$$

is the minimum energy of the neutron before the collision, obtained from kinematics, and  $h_j(x)$  is a step function with a smooth transition,

$$h_j(x) = \begin{cases} 0, & x > 0 \\ (-x)^{j+1}, & -1 < x < 0 \\ 1, & x < -1 \end{cases}. \quad (3.56)$$

The full derivation of this interaction rate can be found in Appendix A. Our result for  $\Gamma^-$  is an extension of that presented in Ref. [118], where the interaction rate was calculated only in the case of low energy and a constant matrix element. It is valid at all energy ranges. The differential interaction rate  $\frac{d\Gamma}{dq_0}(E_\chi, q_0)$  is then

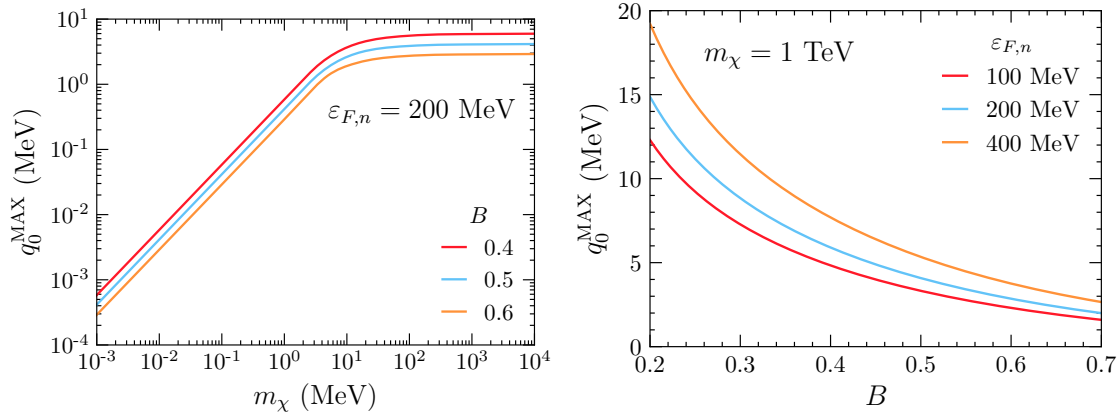


**Figure 3.2:** Left:  $q_0^{\text{MAX}}$  vs.  $m_\chi$  for  $\epsilon_{F,n} = 200 \text{ MeV}$  and different values of  $B$ . Right:  $q_0^{\text{MAX}}$  as a function of  $B$  for different values of  $\epsilon_{F,i}$  and  $m_\chi = 1 \text{ TeV}$ .

just the integrand of Eq. 3.54. We will use  $\frac{d\Gamma}{dq_0}$  to obtain normalised shapes for the differential interaction spectrum, while we will use  $\Omega^-$  when we need the total interaction rate, such as in the capture rate.

Kinematics, and the phase space allowed by  $h_j(x)$  in Eq. 3.54, determine the maximum energy that a DM particle can lose in a single scattering interaction,  $q_0^{\text{MAX}}$ . The details of how to obtain  $q_0^{\text{MAX}}$  are given in Appendix A.2.1. For DM capture, the value of  $q_0^{\text{MAX}}$  depends primarily on the DM mass, as is illustrated in the left panel of Fig. 3.2. We can see that for low  $m_\chi$ ,  $q_0^{\text{MAX}} \propto m_\chi$ , while, for  $m_\chi \gg m_n$ , it plateaus to values between  $q_0^{\text{MAX}} \sim 3 - 6 \text{ GeV}$ . Both  $q_0^{\text{MAX}}$  and  $\frac{d\Gamma}{dq_0}$  also depend on  $\epsilon_{F,n}$  and  $B$ . Changing  $\epsilon_{F,n}$  has a very mild effect on the value of  $q_0^{\text{MAX}}$  (see right panel of Fig. 3.2) and on the shape of the normalised spectrum (see Fig. 3.3). On the other hand, increasing  $B$  has the main effect of reducing  $q_0^{\text{MAX}}$  (see right panel of Fig. 3.2), but only a mild effect on the shape of the profile expressed as a function of the normalised energy loss

$$q_0^{\text{norm}} = \frac{q_0}{q_0^{\text{MAX}}}. \quad (3.57)$$

We apply our results for  $\frac{d\Gamma}{dq_0}$  to DM-neutron interactions, and in particular those with differential cross-sections that depend only on the transferred momentum  $t = (k^\mu - k'^\mu)^2$  and not on the centre of mass energy  $s = (p^\mu + k^\mu)^2$ .

In Fig. 3.3 we show the normalised differential rates as a function of  $q_0^{\text{norm}}$  for the four operators D1-D4. The left-hand panels are in the limit  $m_\chi \gg m_n$ . We can observe that D1 has a softer spectrum, while the D2 and D4 spectra peak towards higher values of  $q_0$ . Varying the chemical potential  $\epsilon_{F,n}$  has a very mild effect, shifting the spectrum to lower values of  $q_0$  with increasing values of  $\epsilon_{F,n}$ .

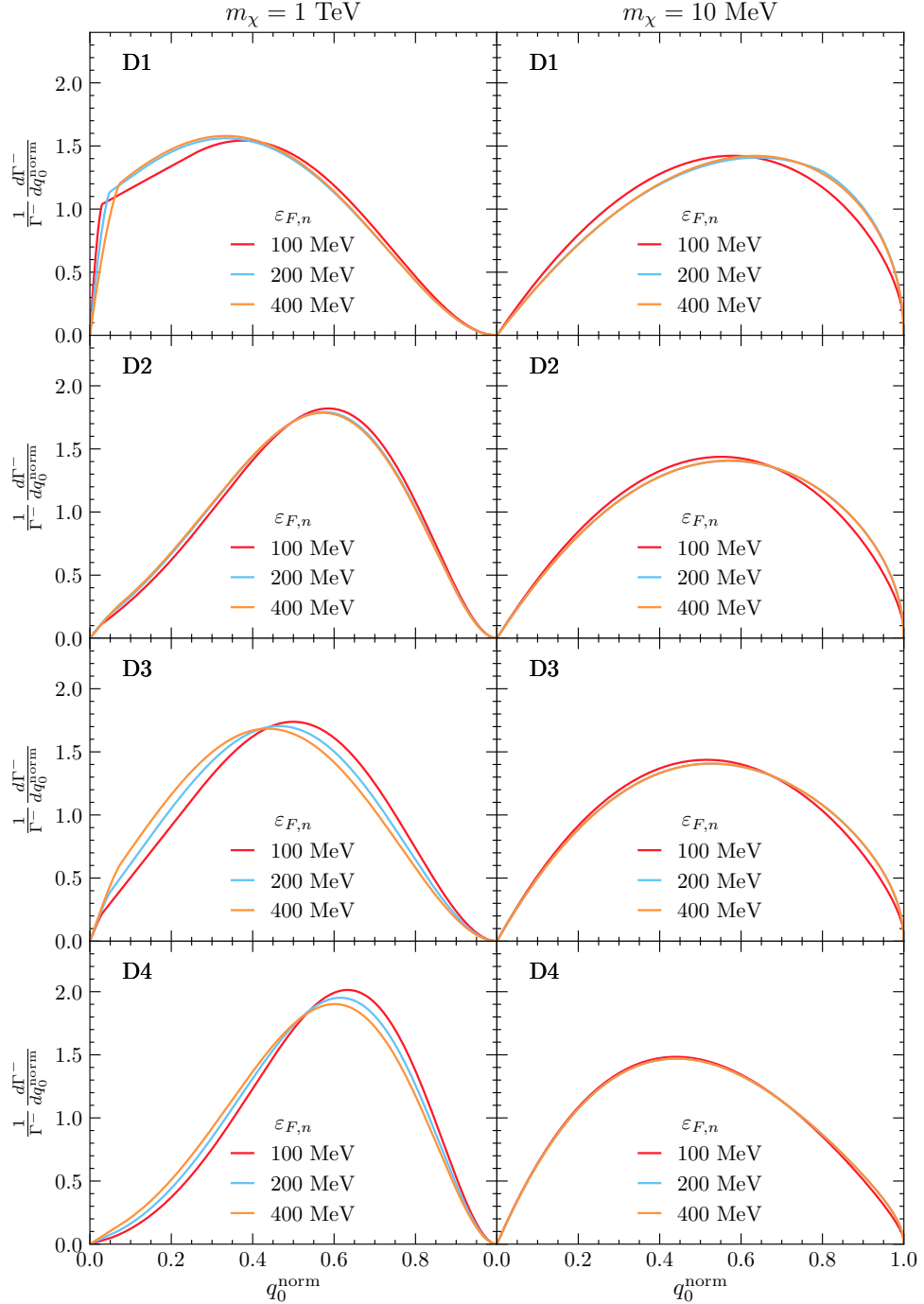


**Figure 3.3:** Normalised differential interaction rates  $\frac{1}{\Gamma} \frac{d\Gamma}{dq_0^{\text{norm}}}$  as a function of  $q_0^{\text{norm}}$  for different values of  $\varepsilon_{F,n}$ ,  $m_\chi = 1 \text{ TeV}$  (left) and  $m_\chi = 10 \text{ MeV}$  (right),  $B = 0.5$  and operators D1 (first row), D2 (second row), D3 (third row) and D4 (fourth row). Profiles do not depend on  $m_\chi$  in the limits  $m_\chi \gg m_n$  (left) and  $m_\chi \ll m_n$  (right).

Note that at small values of  $q_0^{\text{norm}}$  there is a sudden change in the slope of the normalised differential rate, which occurs for all operators but is more evident in D1 (top left panel). This is due to the zero temperature approximation, implicit in Eq. 3.54, where Heaviside functions were used to approximate FD distributions (see Appendix A.2.1); using a finite temperature would produce a smoother spectrum at small  $q_0^{\text{norm}}$ .

In the right-hand panels of Fig. 3.3, we explore the low DM mass region  $m_\chi \ll m_n$ . In this case, all operators give rise to similar profiles, the sole difference being that the peak of the profile is now shifted to lower  $q_0^{\text{norm}}$  for D4 in contrast to D1, with intermediate values for D2 and D3. This is a consequence of Pauli blocking, with this effect depending on the specific power of  $t$  that dominates the spectrum. Profiles with lower  $n$  ( $d\sigma \propto t^n$ ) peak at higher  $q_0^{\text{norm}}$  (see Fig. 3.3, right panels). For D4 we have  $|\bar{\mathcal{M}}|^2 \propto t^2$ , while the matrix elements of D2 and D3 are linear combinations of  $t$  and  $t^2$ , and D1 is a combination of all powers of  $t$ . Comparing the right panels of Fig. 3.3 with Fig. A.2, we observe that the lowest power of  $t$  determines the shape of the final differential interaction rate. Finally, varying  $\varepsilon_{F,n}$  has a very mild effect, this time shifting the spectrum mostly to higher values of  $q_0$  for higher  $\varepsilon_{F,n}$ .

The fact that the lowest power of  $t$  dictates the features of the differential interaction rate is true also for the interactions that have a dependence on  $s$ . As such, by understanding the properties of the interaction rates with  $|\bar{\mathcal{M}}|^2 \propto t^n$ , we can understand the rates for all the operators in Table 1.1.

### 3.3.1 Pauli Blocking

The DM interaction rate, Eq. 3.50, will be proportional to the number of target particles available to scatter off. Classically, this is the total number of targets within the star. However, the quantum degeneracy of the species within compact objects, due to the extreme densities, leads to a reduction in the number of available initial state target particles the DM can scatter off. To understand this, consider the  $T \rightarrow 0$  approximation, in which all initial states with energies  $E_i < \varepsilon_{F,i}$  are occupied. These states are known as the “Fermi sea”. In order for the DM to scatter off one of these states, it must impart enough energy to kick the target out of the Fermi sea, such that

$$E'_i = E_i + q_0 > \varepsilon_{F,i}, \quad (3.58)$$

imposing a lower limit on the energy transfer required for an interaction to take place. This effectively reduces the number of available targets to only those with kinetic energies between  $\varepsilon_{F,n} - q_0$  and  $\varepsilon_{F,i}$ . This suppression of the initial state phase space is known as Pauli blocking (PB), and is a completely quantum phenomenon.

In this limit, we necessarily have  $\Gamma^- \rightarrow 0$  for  $q_0 \rightarrow 0$ . It is also worth noting that Pauli blocking only affects the interaction rate when  $q_0 \leq \varepsilon_{F,n}$ .

To assess the impact of PB on the DM differential interaction rate, in Fig. 3.4 we compare the rate with (blue solid lines) and without (light blue dashed lines) Pauli blocking, for  $B = 0.5$  and constant DM-neutron cross-section. When Pauli blocking can be neglected, the interaction rate is obtained straightforwardly from Eq. 3.50 by stripping away the  $(1 - f_{FD}(E'_i))$  factor. The difference between the computations is shaded in light blue. In the top left panel, we see that the rate begins to be suppressed from PB at  $q_0 \sim \varepsilon_{F,i} = 100$  MeV for a 1 GeV DM. In the top right plot, we increase the neutron chemical potential from  $\varepsilon_{F,n} = 100$  MeV to  $\varepsilon_{F,n} = 400$  MeV. Given that in this case  $q_0^{\text{MAX}} \sim 0.4m_\chi \sim 400$  MeV, almost the whole energy range is affected by PB. The higher  $\varepsilon_{F,n}$  changes the spectra (both with and without PB) such that the unsuppressed rate is no longer flat at low  $q_0$ . The PB suppressed rate reaches a maximum at values of  $q_0$  slightly below  $q_0^{\text{MAX}}$ , and then decreases towards 0 at lower  $q_0$ . In the middle panels,  $m_\chi = 100$  MeV, and  $q_0^{\text{MAX}} \sim 40$  MeV  $\ll \varepsilon_{F,n}$ . In this case, it is evident that PB affects the spectrum over the full  $q_0 = q_0^{\text{MAX}}$  range. In the bottom row, we set  $m_\chi = 10$  MeV. As expected, for lighter DM, the effects of PB are even more pronounced.

To understand how the effect of PB varies throughout the star, we can analyse the radial profiles of the capture rates  $dC/dr$ . In Fig. 3.5 we plot the differential capture rate as a function of the NS radius, with and without Pauli blocking. We see that Pauli blocking is most significant at low DM mass, below about 1 GeV, and becomes insignificant for higher masses. Pauli blocking has a larger impact on the differential capture rate deeper into the NS interior and has a negligible effect at the surface. This is particularly apparent in the top left panel of Fig. 3.5. This is because the chemical potential is higher in the NS interior than it is near the crust, as seen in the radial  $\varepsilon_{F,i}$  profile in the bottom left panel of Fig. 2.4.

### 3.4 Capture in the Low, Intermediate and High Mass Regimes

Having assembled all the required machinery, we are ready to explore the properties of the capture rate in the three mass regimes outlined in Eq. 3.28. Given the computational load required to evaluate Eq. 3.26 in general, we aim to provide approximations that are numerically more efficient where possible. We also discuss the high DM mass regime where multiple scatterings are required for capture, and how this is affected by Pauli blocking.

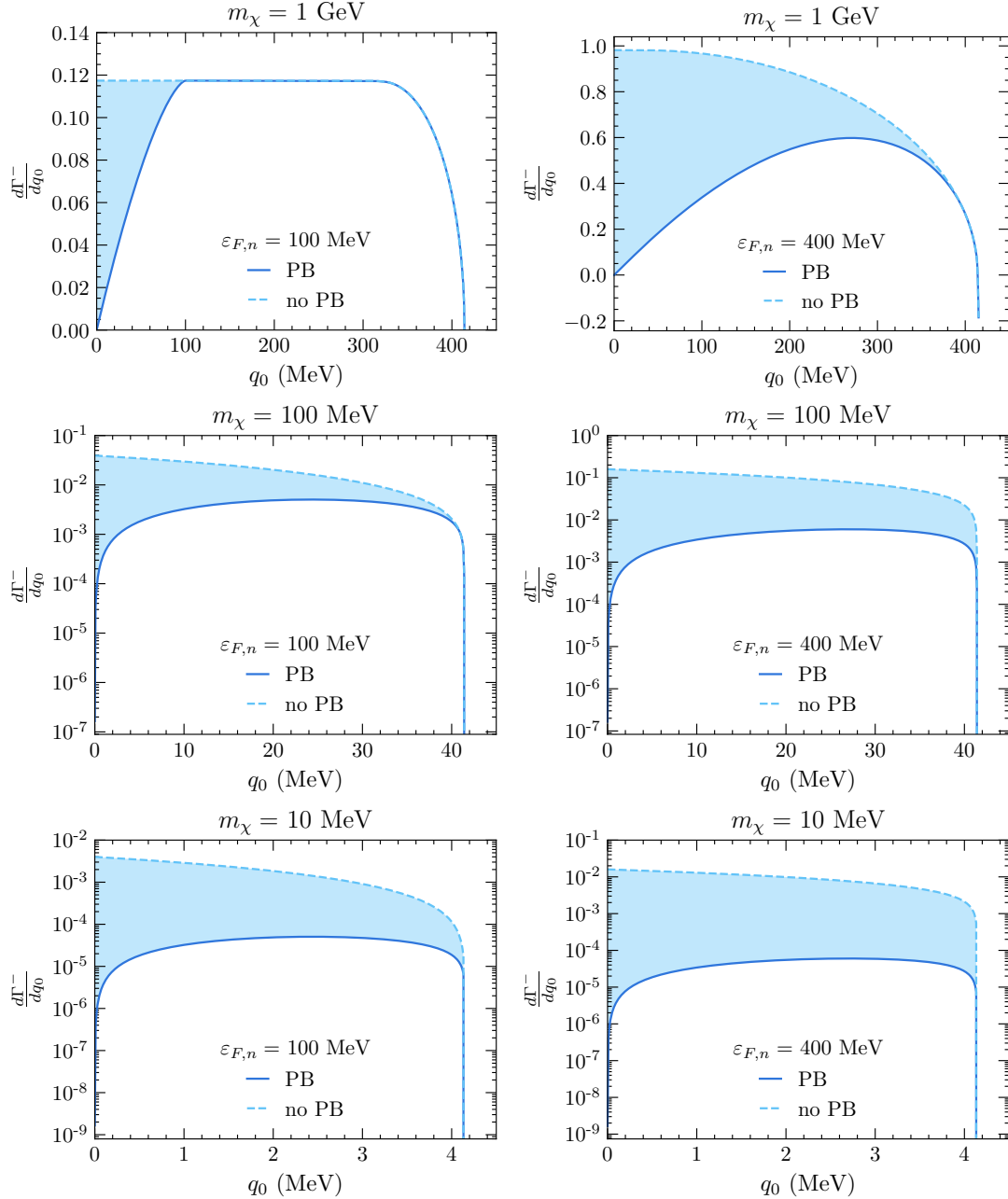


**Figure 3.4:** Differential interaction rates  $\frac{d\Gamma}{dq_0}$  as a function of the energy loss  $q_0$  for different values of  $m_\chi$  and  $\varepsilon_{F,n}$ , constant cross-section and  $B = 0.5$ . Blue lines refer to the result that includes Pauli blocking, while the light blue dashed lines refer to the result without PB. Left column:  $\varepsilon_{F,n} = 100 \text{ MeV}$ , right column:  $\varepsilon_{F,n} = 400 \text{ MeV}$ . Top:  $m_\chi = 1 \text{ GeV}$ , middle:  $m_\chi = 100 \text{ MeV}$ , bottom:  $m_\chi = 10 \text{ MeV}$ .

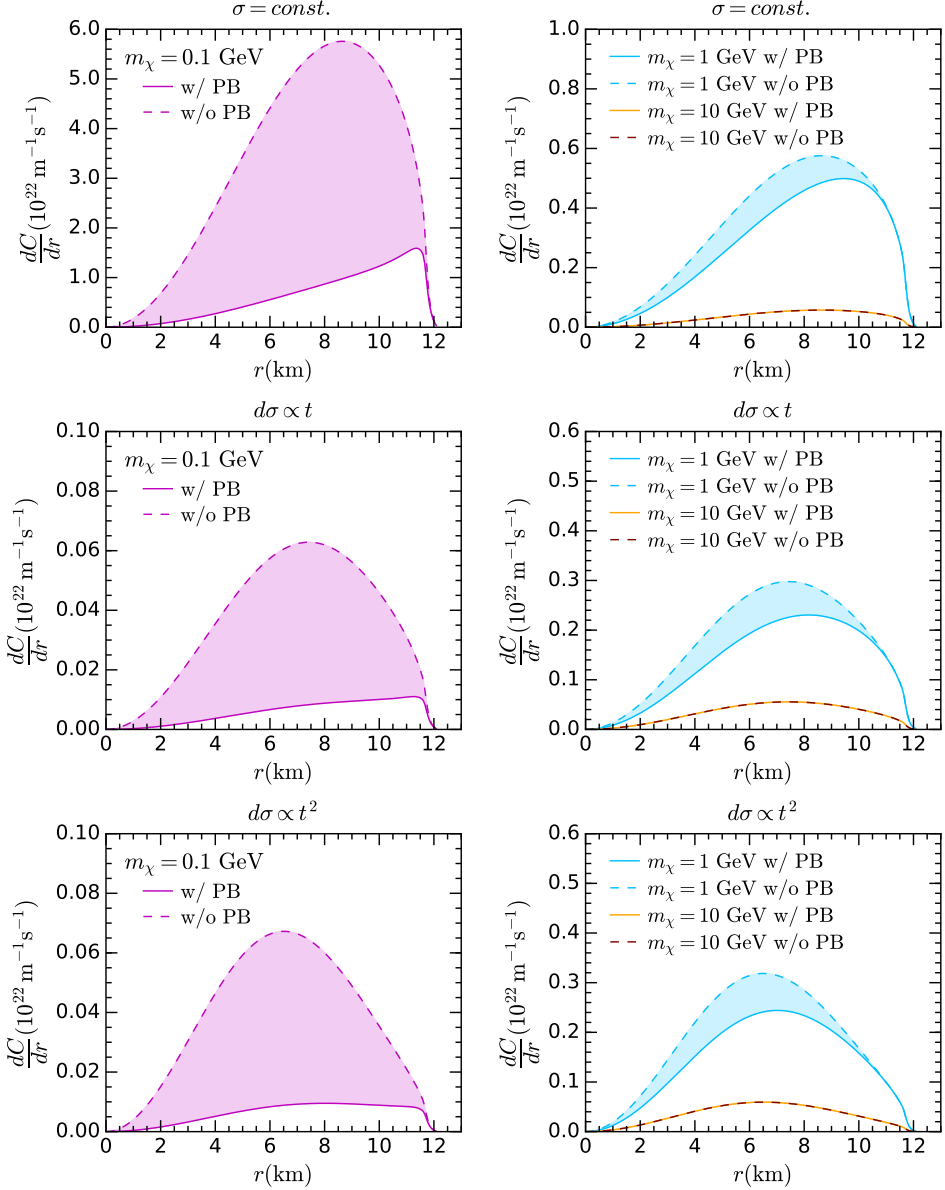


**Figure 3.5:** Differential capture rate as a function of the NS radius  $r$ , with (solid) and without (dashed) Pauli blocking, for the EoS benchmark BSk24-2. Top: constant cross-section, center:  $d\sigma \propto t$ , bottom:  $d\sigma \propto t^2$ .

### 3.4.1 Low and intermediate DM mass range

In sections 3.2 and 3.3, we have derived general expressions to numerically calculate the DM capture and interaction rates, Eqs. 3.26 and 3.39 respectively. Using these expressions, we can write the complete expression for the capture rate as a function of the differential DM-neutron cross-section

$$C = \frac{2\rho_\chi}{\pi v_\star m_\chi^2} \text{Erf} \left( \sqrt{\frac{3}{2}} \frac{v_\star}{v_d} \right) \int_0^{R_\star} dr \frac{r^2 \zeta(r)}{\sqrt{B(r)}} \int dt dE_i ds \frac{d\sigma}{d \cos \theta_{\text{cm}}} \frac{E_i s}{\beta(s) \gamma(s)} (3.59) \\ \times f_{\text{FD}}(E_i, r)(1 - f_{\text{FD}}(E'_i, r)),$$

where the functions  $\beta$  and  $\gamma$  were given in Section 3.2.3. Recall that in the limit  $T \rightarrow 0$ ,  $f_{\text{FD}}(E_i, r)$  and  $1 - f_{\text{FD}}(E'_i, r)$  reduce to the step functions,  $\Theta(\varepsilon_{F,i}(r) - E_i)$  and  $\Theta(E'_i - \varepsilon_{F,i}(r))$ , respectively.

Exchanging the differential cross-section for the squared matrix allows for easier examination of the operators in Table 1.1, and so we write the capture rate as

$$C = \frac{\rho_\chi}{8\pi^2 v_\star m_\chi^2} \text{Erf} \left( \sqrt{\frac{3}{2}} \frac{v_\star}{v_d} \right) \int_0^{R_\star} dr \frac{r^2 \zeta(r)}{\sqrt{B(r)}} \int dt dE_i ds \frac{|\bar{\mathcal{M}}|^2 E_i}{2s\beta(s) - \gamma^2(s)} \frac{s}{\gamma(s)} (3.60) \\ \times f_{\text{FD}}(E_i, r)(1 - f_{\text{FD}}(E'_i, r)).$$

This expression can be used to numerically calculate the single scatter capture rate of DM in compact objects, in the optically thin regime. In general, this must be used for low-mass DM where PB is in effect.

As discussed in Section 3.3.1, PB eventually becomes negligible for DM with masses  $\gtrsim \mu_{F,i}$ . Hence, between this mass and the point where multiple scattering becomes important, PB can be neglected and a simplified capture rate be obtained. For nucleon targets, this range is between  $1 \text{ GeV} \lesssim m_\chi \lesssim 10^6 \text{ GeV}$ , which we call the intermediate mass range.

The resulting simplified capture rate differs slightly depending on whether the matrix element depends only on  $t$ , or if it has explicit  $s$  dependence. We present the full derivations of these results in Appendix A.4 First, for  $|\bar{\mathcal{M}}|^2 = at^n$ , the previous expression can be simplified to

$$C \sim C_{\text{approx}} = \frac{4\pi}{v_\star} \frac{\rho_\chi}{m_\chi} \text{Erf} \left( \sqrt{\frac{3}{2}} \frac{v_\star}{v_d} \right) \int_0^{R_\star} r^2 dr n_i(r) \frac{1 - B(r)}{B(r)} \langle \sigma(r) \rangle, (3.61)$$

$$\langle \sigma(r) \rangle = \left\langle \int dt \frac{d\sigma}{dt} \right\rangle_s = \frac{a}{16\pi m_\chi^2} \frac{1}{n+1} \left( \frac{4(1 - B(r))m_\chi^2}{B(r)(1 + \mu^2)} \right)^n. (3.62)$$

For  $s$ -dependent matrix elements the result is very similar, with the only difference being that the cross-section is not averaged over  $s$ , and instead  $s$  is fixed to a

particular value as detailed in Appendix A.4. Writing the matrix element as  $|\bar{\mathcal{M}}|^2 \propto \bar{g}(s)t^n$ , for with  $g$  some function of  $s$ , we arrive at the result

$$C \sim C_{\text{approx},s} = \frac{4\pi}{v_\star} \frac{\rho_\chi}{m_\chi} \text{Erf} \left( \sqrt{\frac{3}{2}} \frac{v_\star}{v_d} \right) \int_0^{R_\star} r^2 dr n_i(r) \frac{1 - B(r)}{B(r)} \sigma(r), \quad (3.63)$$

$$\begin{aligned} \sigma(r) &= \int dt \frac{d\sigma}{dt} = \frac{1}{16\pi \left( m_i^2 m_\chi^2 + 2m_i m_\chi / \sqrt{B(r)} \right)} \frac{\bar{g}(s_0)}{(n+1)} \\ &\quad \times \left[ \frac{4(1 - B(r))m_\chi^2}{B(r)(1 + \mu^2) + 2\sqrt{B(r)}\mu} \right]^n, \end{aligned} \quad (3.64)$$

$$s_0 = m_i^2 + m_\chi^2 + 2 \frac{E_i m_\chi}{\sqrt{B(r)}}. \quad (3.65)$$

As with the differential interaction rates, it is the  $t$ -dependence of the matrix elements that dictate the key features of the capture rate.

In Fig. 3.6, we show the capture rate as a function of the DM mass for matrix elements proportional to  $t^n$ , for  $n = 0, 1, 2$  and the NS benchmark model BSk24-2. Numerical results obtained using Eq. 3.60 are shown in solid red; results using the same equation but removing the theta function that enforces Pauli blocking are depicted in light blue; and the approximation for intermediate DM masses, Eq. 3.61, in yellow. We show the geometric limit, Eq. 3.27, in blue for comparison. The capture rates were all normalised to the geometric limit at large DM mass where PB is negligible. In the same plots, we also show in brown the result obtained from using a modified version of Eq. 3.61 to include Pauli blocking. This is achieved by including the ratio between the differential the interaction rate,  $\Gamma^-$ , calculated with and without Pauli blocking. This comparison was done in Section 3.3.1 for various values of  $B$  and  $\varepsilon_{F,n}$ .

From Fig. 3.6, we can see that Eq. 3.61 is indeed a good approximation to the numerical results obtained without Pauli blocking, and can be safely used for DM masses from a few GeV up to  $m_\chi \sim 10^6$  GeV, where multiple scattering becomes relevant. On the other hand, for  $m_\chi \lesssim 100$  MeV the brown line is no longer a good approximation to the numerical result with Pauli blocking, as it always overestimates the capture rate by nearly an order of magnitude. Therefore, to accurately account for the effects of PB for low mass DM, the complete expression for the capture rate, Eq. 3.60 must be used and evaluated numerically.

We now compare our full numerical capture rate calculation, Eq. 3.60, with that of Ref. [116], in Fig. 3.7. The capture rates calculated in Ref. [116] correctly include the stellar structure and Pauli blocking, however, they do not account for general relativistic corrections, and the authors only considered the case of a constant cross-section,  $\sigma = 10^{-45} \text{ cm}^2$ . To make the comparison as fair as possible, we have

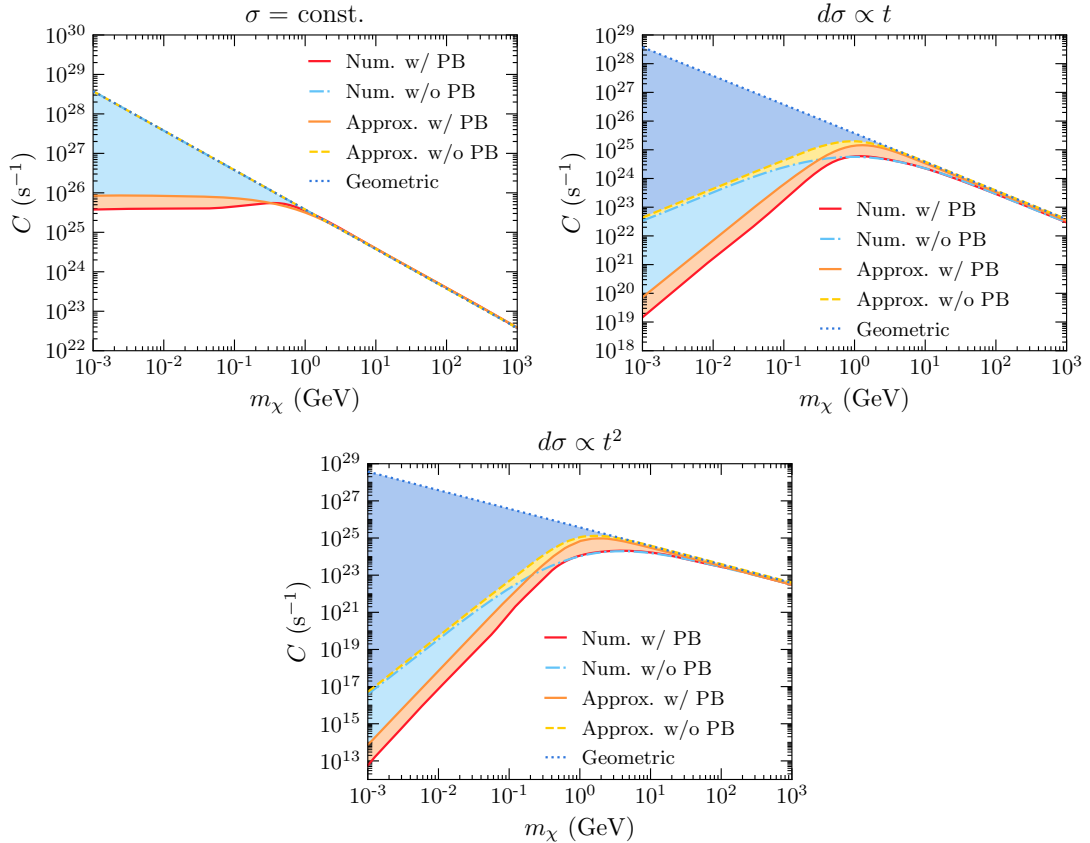


**Figure 3.6:** Capture rate as a function of the DM mass with cross-sections normalised to  $\sigma = \sigma_{\text{ref}} \sim 1.7 \times 10^{-45} \text{ cm}^2$ , for EoS BSk24-2, calculated with and without Pauli blocking. Top left: constant cross-section. Top right:  $d\sigma \propto t$ , bottom:  $d\sigma \propto t^2$ , where  $t$  is the Mandelstam variable. All rates are normalised to the geometric limit at large DM mass.

selected NS configurations that match those of Figs. 1 and 14 of Ref. [116], namely their Model A (BSk20-1):  $M_\star \simeq 1.52M_\odot$ ,  $R_\star \simeq 11.6$  km and Model D (BSk21-2):  $M_\star \simeq 2.11M_\odot$  and  $R_\star \simeq 12.0$  km. We denote these new benchmark models as BSk26-1 (left panel of Fig. 3.7) and BSk24-5 (right panel). Note that we were not able to use the BSk20 and BSk21 functionals, since there are no publicly available fits for the chemical potentials and particle abundances for those EoS families. However, as discussed earlier in section 2.3.2, BSk26 (BSk24) yields configurations that are almost indistinguishable from those obtained with BSk20 (BSk21) [221].

We can see in the left panel of Fig. 3.7 that in the non-Pauli suppressed region,  $m_\chi \gtrsim 1$  GeV, our capture rate calculation in the optical thin limit (solid magenta) exceeds that of Ref. [116] (dot-dashed blue) by a factor of  $\sim 4$ . When Pauli blocking is active, our capture rate calculation is about one order of magnitude higher than the classical calculation. Recall that Ref. [116] accounts for neither gravitational focusing nor relativistic kinematics. We also show in dashed light blue the approximation given in Ref. [16], which accounts for Pauli blocking with a suppression factor that depends on the neutron Fermi momentum  $\sim m_\chi v_{esc}/p_{F,n}$  for  $m_\chi < m_n$ . Though this approximation fails to reproduce the capture rate shape due to Pauli blocking in the DM mass range [0.1 GeV, 10 GeV], it underestimates the capture rate by only a factor of 2 when the DM mass is below 0.1 GeV. Finally, we compare the geometric limit of Eq. 3.27 (solid orange) that incorporates GR effects [132] with the non-relativistic expression in Ref. [116] (dot-dashed brown). We observe that the former is  $\sim 67\%$  greater than the latter, mostly due to the  $1/B(R_\star)$  GR correction [237, 238]. Similar conclusions are obtained when comparing capture rate calculations for Model D of Ref. [116] (their Fig. 14) with our approach, as illustrated in the right panel of Fig. 3.7.

### 3.4.2 Large Mass Regime: Multiple Scattering

The capture rate expressions obtained in the previous section assume that the cross-section is small enough that the star is in the “optically thin” regime, and that a single scatter is sufficient to capture the DM. These assumptions break down if the DM-target cross-section is  $\gtrsim \mathcal{O}(\sigma_{th})$ , or if the DM mass exceeds  $m_\chi \sim 10^6$  GeV, respectively. In this section, we focus on addressing the latter concern as we work in the optically thin regime for the remainder of this work<sup>4</sup>. To that end, we now explain how to modify our previous capture rate expressions to account for multiple scattering in a degenerate media<sup>5</sup>.

In deriving Eq. 3.59 we had assumed that the DM velocity at infinity,  $u_\chi$ , can

<sup>4</sup>The discussion on the effect of the NS opacity in  $\sigma \sim \sigma_{th}$  regime can be found in Ref. [235].

<sup>5</sup>For a recent discussion on multiple scattering within non-relativistic stars, or with ions in WDs, see Ref. [240].

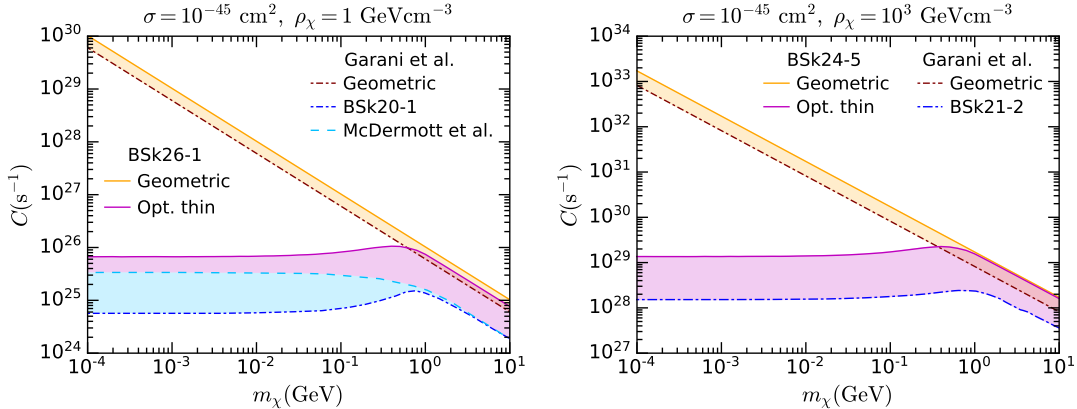


**Figure 3.7:** Left: Capture rate in the optically thin (magenta) and geometric (orange) limits as a function of the DM mass for constant cross-section  $\sigma = 10^{-45} \text{ cm}^2$ ,  $\rho_\chi = 1 \text{ GeV cm}^{-3}$  and BSk26 functional for  $M_\star \simeq 1.52M_\odot$  and  $R_\star \simeq 11.6 \text{ km}$  denoted as BSk26-1. Capture rate calculations from Ref. [116] for a NS configuration with EoS BSk20-1 [216] equivalent to BSk26-1, are shown for comparison. Right: Same as left but for  $\rho_\chi = 10^3 \text{ GeV cm}^{-3}$  and the benchmark model BSk24-5 equivalent to BSk21-2 in Ref. [116]:  $M_\star \simeq 2.11M_\odot$  and  $R_\star \simeq 12.0 \text{ km}$ .

be neglected, such that any interaction where the DM loses energy resulted in its capture. If we instead keep the leading order  $u_\chi$  contribution to the total DM energy, the DM energy at infinity is

$$E_\chi^\infty \sim m_\chi \left( 1 + \frac{1}{2} u_\chi^2 \right), \quad (3.66)$$

and at a distance  $r$  from the star, it gets boosted to

$$E_\chi(r) = \frac{m_\chi}{\sqrt{B(r)}} \left( 1 + \frac{1}{2} u_\chi^2 \right). \quad (3.67)$$

Therefore, the amount of energy that the DM must lose to be captured is

$$E_\chi^C(r) = \frac{1}{2} u_\chi^2 \frac{m_\chi}{\sqrt{B(r)}}. \quad (3.68)$$

$$\sim 0.6 \text{ GeV} \left( \frac{u_\chi}{270 \text{ km s}^{-1}} \right)^2 \left( \frac{m_\chi}{10^6 \text{ GeV}} \right) \left( \frac{0.5}{B(r)} \right)^{1/2}. \quad (3.69)$$

Hence, DM with a mass of  $10^6 \text{ GeV}$  with an initial velocity  $u_\chi = 270 \text{ km s}^{-1}$ , must lose 0.6 GeV of energy for it to be captured. This is of the same order as the

maximum amount of energy that can be lost in a single scatter as seen in Fig. 3.2. Given that  $q_0^{\text{MAX}}$  plates for  $m_\chi \gg m_i$ , it will be highly improbable that DM heavier than  $\sim 10^6$  GeV loses enough energy in a single scatter to be captured. Single scatter capture is still possible as the DM velocity at infinity is not a fixed value, rather it follows by some distribution function. Therefore, the heavy DM could have a velocity close to zero at infinity, significantly reducing the amount of energy it needs to lose.

To account for this effect, we assume that the DM particles have a speed  $u_\chi \ll 1$  at infinity that follows a Maxwell-Boltzmann (MB) distribution, Eq. 3.18. We can then define the probability density function (PDF) of the energy lost by the DM using the differential interaction rate through

$$\xi(q_0, E_\chi, \varepsilon_{F,i}) = \frac{1}{\Gamma^-(E_\chi)} \frac{d\Gamma^-}{dq_0}(q_0, E_\chi, \varepsilon_{F,i}), \quad (3.70)$$

where  $\frac{d\Gamma}{dq_0}$  is the DM differential interaction rate, calculated in Appendix 3.3. The function  $\xi$  is defined for any  $q_0 \geq 0$ , however, kinematics dictates that the function is non-zero only for  $q_0 \leq q_0^{\text{MAX}}$ . Additionally, note that  $\xi$  depends on  $B(r)$  through the ratio  $E_\chi/m_\chi$ , and for brevity we will simply write  $\xi(q_0)$ .

We can define the probability of losing at least an amount of energy  $q_0 = \delta q_0$  in a single collision as

$$P_1(\delta q_0) = \int_{\delta q_0}^{\infty} dx \xi(x). \quad (3.71)$$

The probability of losing at least the same amount of energy after 2 collisions will then be

$$P_2(\delta q_0) = \int_{\delta q_0}^{\infty} dy \int_0^{\infty} dx \xi(x) \xi(y-x) \quad (3.72)$$

$$= P_1(\delta q_0) + \int_{\delta q_0}^{\infty} dy \int_0^y dx \xi(x) \xi(y-x) \quad (3.73)$$

$$= P_1(\delta q_0) + \int_0^{\delta q_0} dz P_1(\delta q_0 - z) \xi(z). \quad (3.74)$$

From this, we obtain the following recursive relation for the probabilities,  $P_N$ , of losing at least  $q_0 = \delta q_0$  in  $N$  scatters,

$$P_{N+1}(\delta q_0) = P_N(\delta q_0) + \int_0^{\delta q_0} dz P_N(\delta q_0 - z) \xi(z). \quad (3.75)$$

In Fig. 3.8 we show how the probability functions  $P_1, \dots, P_5$  changes based on the  $t$  dependence of the differential cross-section. We show results for  $\sigma = \text{const.}$  (top

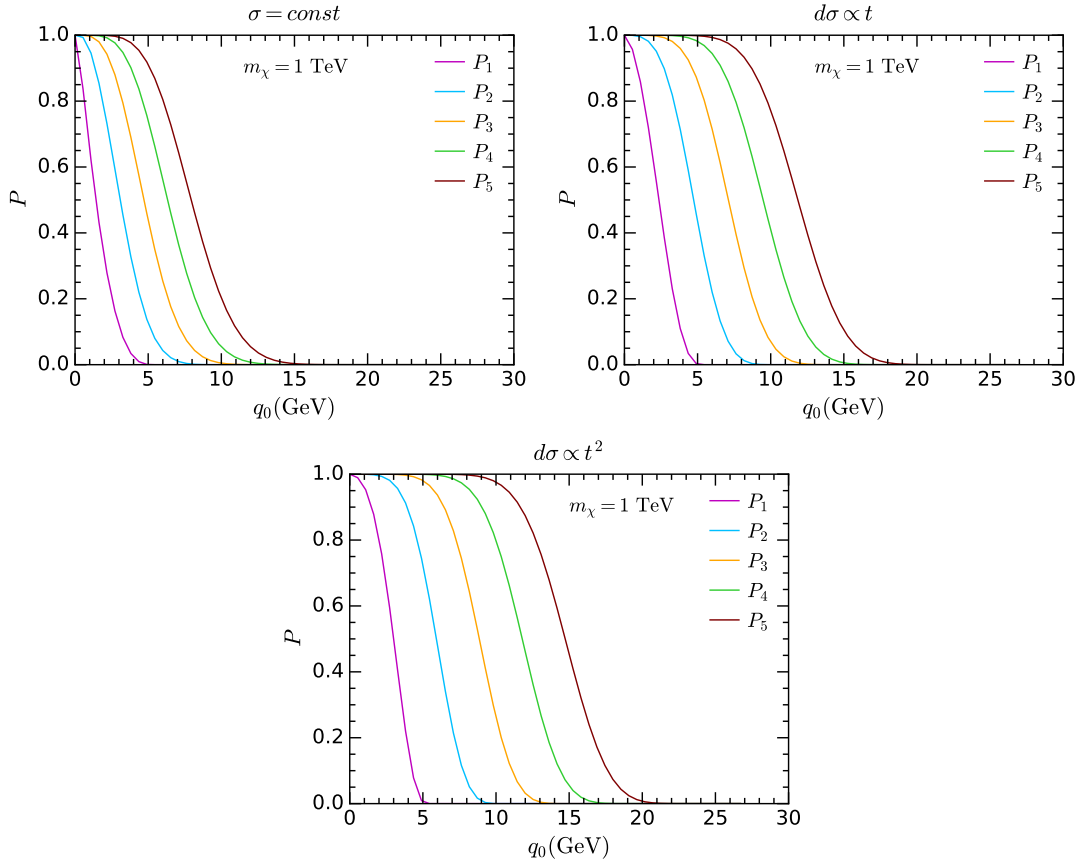


**Figure 3.8:** Probabilities to lose at least an amount of energy  $\delta q_0$  after  $1, \dots, 5$  scatterings,  $P_1, \dots, P_5$ , as a function of the energy loss  $q_0$ , assuming  $B = 0.5$  and  $\varepsilon_{F,n} = 400$  MeV. Results are shown for different dependence on the cross-section on the Mandelstam variable  $t$ : constant DM-neutron cross-section (top left),  $d\sigma \propto t$  (top right) and  $d\sigma \propto t^2$  (bottom).

left),  $d\sigma \propto t$  (top right) and  $d\sigma \propto t^2$  (bottom), for fixed values of  $B = 0.5$ ,  $\varepsilon_{F,n} = 400$  MeV.

To connect this back to the capture probability, we define the probability for a DM particle to be captured after exactly  $N$  interactions,  $c_N$ , to be  $P_N(E_\chi^C) - P_{N-1}(E_\chi^C)$  averaged over the MB distribution of the initial velocity,

$$c_N(r) = \frac{1}{\int_0^\infty \frac{f_{MB}(u_\chi)}{u_\chi} du_\chi} \int_0^\infty \frac{f_{MB}(u_\chi)}{u_\chi} du_\chi \left[ P_N \left( \frac{1}{2} \frac{m_\chi u_\chi^2}{\sqrt{B(r)}} \right) - P_{N-1} \left( \frac{1}{2} \frac{m_\chi u_\chi^2}{\sqrt{B(r)}} \right) \right], \quad (3.76)$$

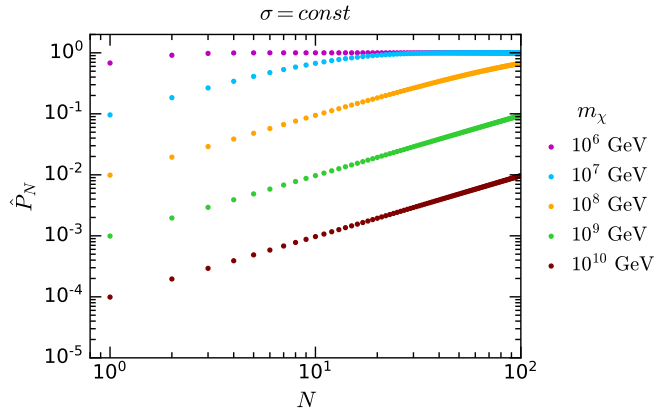


**Figure 3.9:** Cumulative probability  $\hat{P}_N$  for  $B = 0.5$ ,  $\varepsilon_{F,n} = 400$  MeV and for  $\sigma = \text{const.}$  as a function of the number of scatterings  $N$  for several DM masses.

where  $c_N$  depends on  $r$  through the dependence of  $P_N$  on  $B(r)$  and  $\varepsilon_{F,n}(r)$ . Note that although our results will assume a Maxwell-Boltzmann velocity distribution, it is straightforward to generalise the results to any other DM velocity distribution. The cumulative probability  $\hat{P}_N$  that a DM particle is captured after  $N$  interactions with a total energy loss  $\delta q_0 = E_\chi^C$  is then

$$\hat{P}_N(r) = \sum_{i=1}^N c_i = \frac{1}{\int_0^\infty \frac{f_{\text{MB}}(u_\chi)}{u_\chi} du_\chi} \int_0^\infty \frac{f_{\text{MB}}(u_\chi)}{u_\chi} du_\chi P_N \left( \frac{1}{2} \frac{m_\chi}{\sqrt{B(r)}} u_\chi^2 \right). \quad (3.77)$$

The resulting cumulative probability is shown as a function of the number of scatterings  $N$  in Fig. 3.9, for constant cross-section and several DM masses.

The cumulative probability  $\hat{P}_N$  for the above values of  $B, \varepsilon_{F,n}$  is well approximated by the function<sup>6</sup>

$$\hat{P}_N \sim 1 - e^{-\frac{Nm_i^*}{m_\chi}}. \quad (3.78)$$

In particular, the probability that the DM is captured in a single scatter is

$$c_1 = \hat{P}_1 \sim 1 - e^{-\frac{m_i^*}{m_\chi}}. \quad (3.79)$$

From this, we see that  $c_1$  will begin to significantly fall below unity for  $m_\chi \gtrsim m_i^*$ , and hence multiple scattering will only significantly reduce the capture rate for DM masses above  $m_i^*$ .

---

<sup>6</sup>Further discussion of the multi-scattering regime, and justification of this fitting function, can be found in Appendix C of Ref. [235].

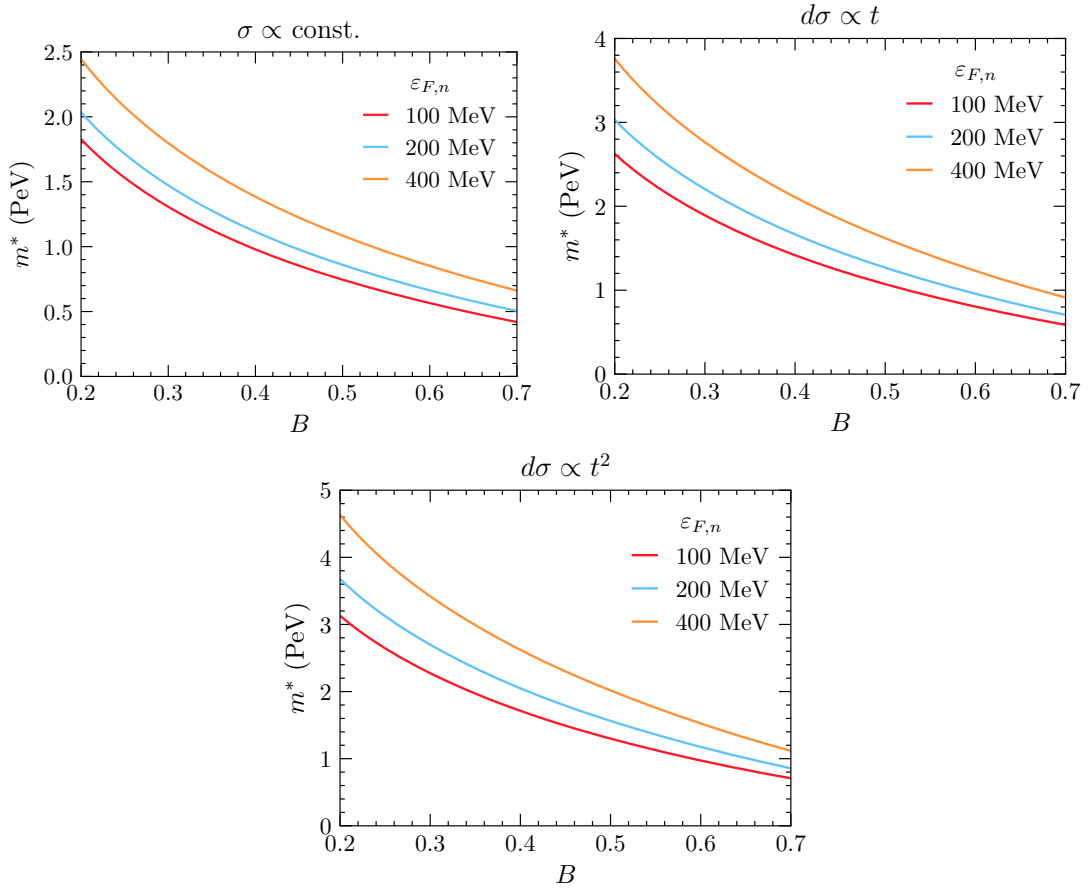


**Figure 3.10:** Value of  $m_n^*$  as a function of  $B$  for different values of  $\varepsilon_{F,n}$ ,  $\sigma = \text{const.}$  (top left),  $d\sigma \propto t$  (top right) and  $d\sigma \propto t^2$  (bottom).

To give an idea for how large the value of  $m_i^*$  will be, for neutron targets and the values  $B = 0.5$  and  $\varepsilon_{F,n} = 400$  MeV, we find

$$m^* = 1.08 \times 10^6 \text{ GeV}, \quad |\bar{\mathcal{M}}|^2 \propto t^0, \quad (3.80)$$

$$m^* = 1.62 \times 10^6 \text{ GeV}, \quad |\bar{\mathcal{M}}|^2 \propto t^1, \quad (3.81)$$

$$m^* = 2.01 \times 10^6 \text{ GeV}, \quad |\bar{\mathcal{M}}|^2 \propto t^2. \quad (3.82)$$

We illustrate how  $m_n^*$  varies with  $B$  and  $\varepsilon_{F,n}$  in Fig. 3.10.

When the cross-section is small,  $\sigma \ll \sigma_{\text{th}}$ , such that we are in the optically thin regime, if the DM does not get captured in its initial scatter, then it will leave the star without interacting again. To account for this, the factor of  $c_1$  should be included in the capture rate calculation, Eq. 3.26. However, as we have just seen,  $c_1 \ll 1$  only for  $m_\chi \gtrsim m_i^*$ , which will always be significantly larger than the target mass and chemical potential. Therefore, multiple scattering is only important in

the regime where PB is negligible, and so a suitable approximation for the capture rate in this regime is

$$C_{\text{approx}}^* = \frac{4\pi}{v_*} \frac{\rho_\chi}{m_\chi} \text{Erf} \left( \sqrt{\frac{3}{2}} \frac{v_*}{v_d} \right) \int r^2 dr \frac{\sqrt{1 - B(r)}}{B(r)} \Omega^-(r) c_1(r), \quad (3.83)$$

with  $\Omega^-(r)$  calculated as outlined in sections 3.4.1

## 3.5 Results

In this section, we present our results for the capture rate of fermionic DM scattering from neutrons within a NS in the zero temperature approximation. We calculate the capture rate only for scalar/pseudoscalar-scalar/pseudoscalar interactions between DM and neutrons, i.e. effective operators D1-D4 in Table 1.1, whose differential cross-sections depend only on the Mandelstam variable  $t$  and not on  $s$ . We use realistic radial profiles for the neutron number density, chemical potential, and relativistic corrections encoded in  $B(r)$  as explained in Section 2.3.2, obtained from the BSk24 EoS for the configurations in Table 2.2.

To estimate the NS EoS impact on the DM capture rate computation, we numerically calculate  $C$  using the exact expression in the optically thin limit, Eq. 3.60, that properly accounts for gravitational focusing and Pauli blocking. In the optically thin regime that we are working in, the capture rate is proportional to the differential DM-neutron cross-section. Fig. 3.11 shows how this rate varies with the NS EoS for operators D1-D4 and the EoS configurations given in Table 2.2, and in turn with the NS mass and radius. The cross-section is normalised such that the capture rate in the intermediate mass range, which is unaffected by PB and multiple scattering, is equal to the geometric limit. It is worth remarking that cross-sections larger than the threshold cross-section should not be used in the optically thin limit, as this would result in capture rates larger than the geometric limit. To account for such large cross-sections, the optical depth of the NS must be accounted for as prescribed in Ref. [235]. Depending on the operator considered, going from the lightest to the heaviest NS can change the capture rate by a minimum of one order of magnitude, such as in the case of operators D1, D2 and D3 (at low DM mass), and up to 2 orders of magnitude, as in the case of operators D2 for large DM mass, and D4 in general.

At large DM mass, all operators show the same scaling with the DM mass. At  $m_\chi \lesssim 1 \text{ GeV}$ , a different picture arises as Pauli blocking leads to different suppressions of the capture rate for the different operators. However, we observe that the four operators give very similar results to those of Fig. 3.6, where we analysed the dependence of the capture rate on the momentum transfer  $t$ . We note that operator

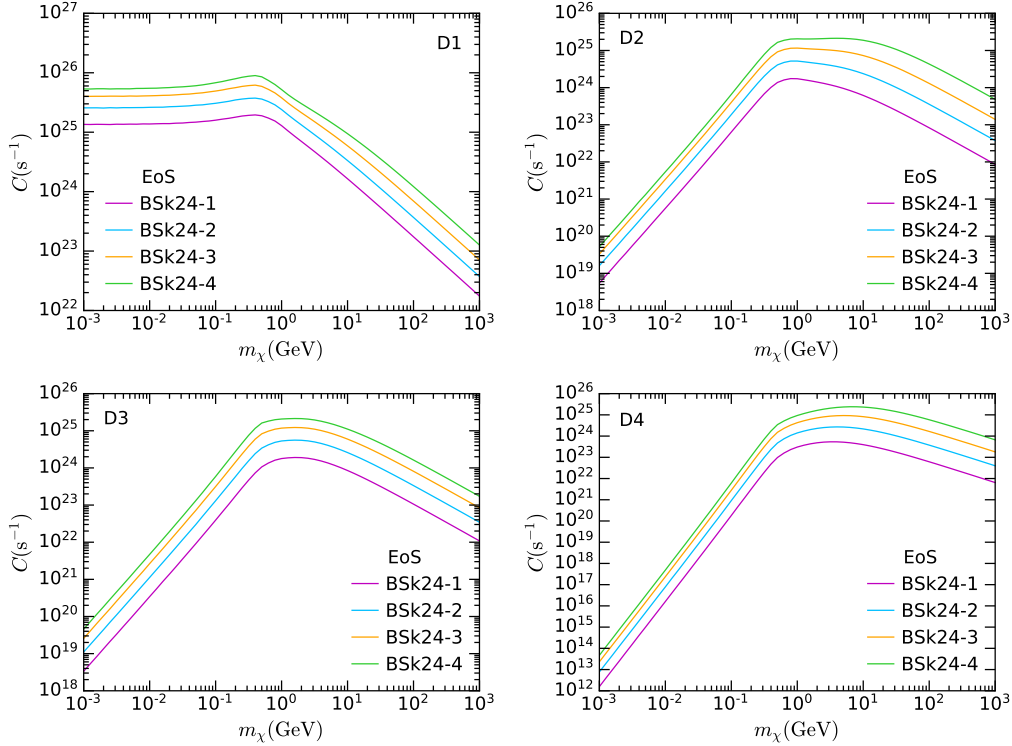


**Figure 3.11:** Capture rate in the optically thin limit as a function of the DM mass for  $\sigma = \sigma_{\text{ref}} \sim 1.7 \times 10^{-45} \text{ cm}^2$  and the configurations of the EoS BSk24 given in Table 2.2. Rate calculated using the 4-dimensional integral in Eq. 3.60, that includes Pauli blocking but neglects the NS opacity and multiple scattering. Results are shown for the EFT operators D1 (top left), D2 (top right), D3 (bottom left) and D4 (bottom right) in Table 1.1.

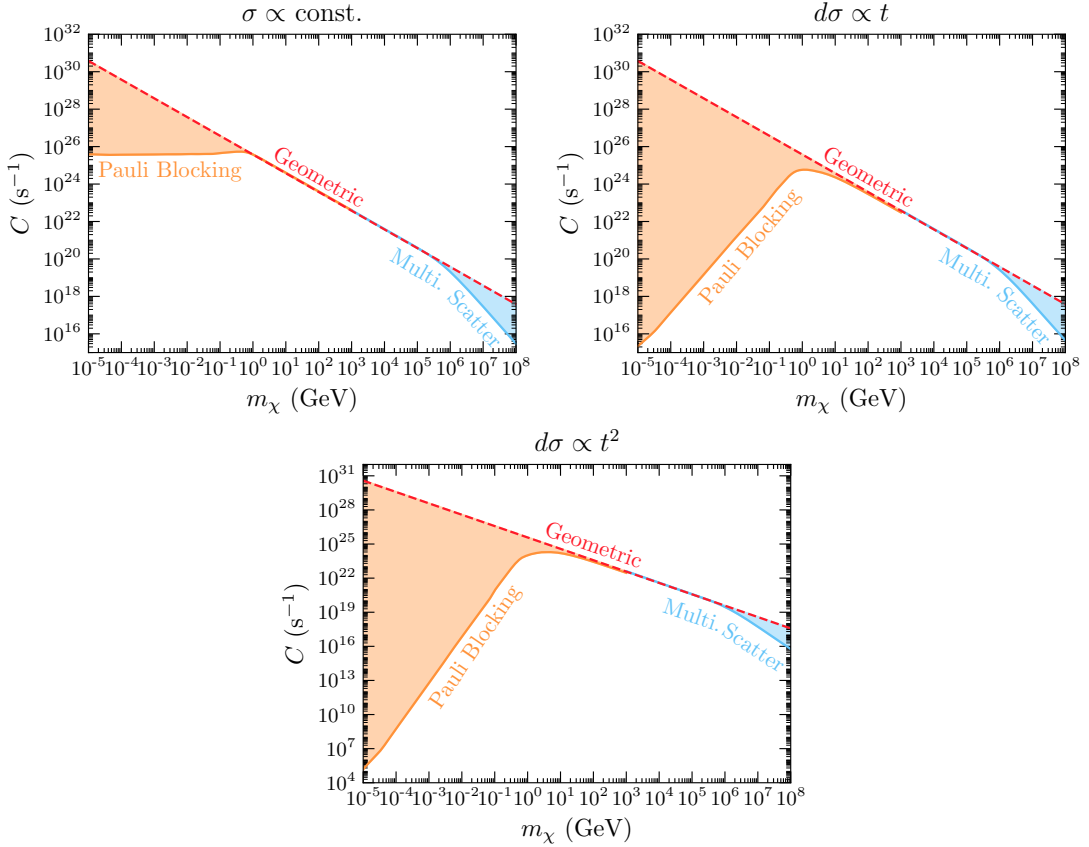


**Figure 3.12:** Capture rate for constant cross-section (top left),  $d\sigma \propto t$  (top right) and  $d\sigma \propto t^2$  (bottom), for  $\sigma = \sigma_{\text{ref}} \sim 1.7 \times 10^{-45} \text{ cm}^2$  and NS EoS configuration BSk24-2. These plots extent the mass range of those in Fig. 3.6 to large DM masses.

D1, which contains in its squared matrix element a term independent of  $t$ , gives a result that is very similar to that of  $\sigma = \text{const.}$  Operators D2 and D3, for which  $|\bar{\mathcal{M}}|^2$  does not include terms independent of  $t$ , but rather terms proportional to  $t$  and  $t^2$ , yield very similar results to that of  $d\sigma \propto t$ . Overall, we conclude that the lowest power of the transferred momentum determines the mass scaling of the capture rate at low DM mass. This result holds true for matrix elements that depend also on  $s$ .

In Fig. 3.12, we show the capture rate for a broad DM mass range, spanning 13 orders of magnitude from  $m_\chi = 10 \text{ keV}$  to  $m_\chi = 10^8 \text{ GeV}$ , including all three of the mass regimes we have discussed in the previous sections, for  $d\sigma \propto \text{const.}$  (first row),  $t^1$  (second row) and  $t^2$  (third row). The orange line indicates the capture rate calculated in the optically thin limit using the 4-dimensional integration in Eq. 3.59 that accounts for Pauli blocking. At large DM masses, Pauli suppression plays no

role and the capture rate approaches the geometric limit (dashed red line). We also show in Fig. 3.12 the effect of the inclusion of multiple scattering in the light blue line, which becomes relevant at  $m_\chi \sim 10^6$  GeV. At  $m_\chi \sim 10^5$  GeV that line matches the geometric limit as expected from the chosen value of the cross-section  $\sigma = \sigma_{\text{ref}}$ . At larger DM masses,  $m_\chi \gtrsim 10^6$  GeV, multiple scatterings are required for the DM to be captured, hence an additional suppression factor of  $1/m_\chi$  arises, as given in Eq. 3.83. Therefore, the capture rate becomes increasingly smaller than  $C_{\text{geom}}$  (light blue shaded area).

Comparing the plots for different  $t^n$  dependence, we can see that increasing the power of  $n$  has a small effect on the mass scale where the various suppressions become relevant. For example, comparing the light blue lines between the three figures, we see that the change of slope from the onset of multiple scattering moves slightly further to the right for larger  $n$ . This is a consequence of the fact that larger powers of  $n$  result in larger energy transfer (see, for example, Fig. A.2), leading to a larger capture probability  $c_1$  and hence a larger  $m_i^*$ . However, the qualitative behaviour is the same for all choices of  $d\sigma$ : the suppression of the capture rate is primarily due to Pauli blocking at low mass and multiple scattering effects (i.e. a low capture probability) at large masses.

## 3.6 Summary

In this chapter, we have improved and extended the existing framework used to calculate the DM capture rate in the Sun to be compatible with compact objects, relaxing the simplifying assumptions that have previously been made. Specifically, we have derived exact expressions for the capture rate that correctly incorporate relativistic kinematics, gravitational focusing, Pauli blocking, and multiple-scattering effects. We also properly incorporate the internal structure of the star, consistently calculating the radial profiles of the EoS-dependent parameters and the general relativistic corrections, by solving the Tolman-Oppenheimer-Volkoff equations.

This new formalism was applied to neutron stars to highlight the features of the formalism mentioned above. Neutron stars (and compact objects in general) are composed of strongly degenerate matter, resulting in significant Pauli blocking of scattering interactions when the dark matter is light,  $m_\chi \lesssim m_i$ , suppressing the capture rate by several orders of magnitude. By including the radial dependence of the chemical potential in our calculations, we correctly account for Pauli suppression at any point in the star. However, note that the chemical potential is dependent on the EoS assumption.

For very large DM masses,  $m_\chi \gtrsim 10^6$  GeV, the energy lost in a single collision will be insufficient for it to be captured. Hence, the DM must scatter multiple

times within an orbit to be captured, or else it simply leaves the star. To correctly compute the DM capture probability due to multiple scattering, we have derived, for the first time, an exact equation for the DM interaction rate in degenerate matter, and used that result to compute the differential capture rate as a function of the DM energy loss. This enables us to compute the cumulative probability that a DM particle is captured after multiple interactions, by averaging over the initial DM velocity distribution.

Although we have framed our results in terms of the scattering of DM from neutron targets in neutron star, it is straightforward to obtain the capture rate for DM scattering from any other degenerate species in compact objects. In the next chapter, we apply this formalism to DM scattering off the leptonic components of NSs, as well as the degenerate electrons within WDs.

# 4

## Dark Matter Capture from Baryonic Matter in Neutron Stars

*This chapter is based on the papers [224, 241], where we incorporate two important effects that are important when considering dark matter capture from baryons in neutron stars. As the momentum transfers involved in the scattering events leading to capture are large, one must account for the internal structure of the baryon. In addition, the high densities of neutron star matter require us to take into account the strong interactions experienced amongst the baryons. We discuss how to properly incorporate both of these effects into the capture formalism presented in this thesis in a self-consistent manner, and discuss their effects on the capture and interaction rates as well as on the threshold cross-sections that a future NS observation would be sensitive to.*

### 4.1 Baryon Structure and Strong Interactions

#### 4.1.1 Baryon Strong Interactions and Effective Masses

At the extremely high densities found in the interiors of neutron stars, the strong interactions amongst the baryons render the free Fermi gas approximation used in Chapter 3 to model the scattering targets invalid. To account for these interactions in a self-consistent way, they should be included in the Lagrangian used to model the nucleon-rich matter. This is often achieved by including effective Skyrme forces, or through a relativistic mean field theory.

The QMC EoS, described in Section 2.3.2, adopts the latter approach. The forces mediated by the Lorentz scalars induce an effective mass for the baryons

different from their vacuum value, such that  $m_i^{\text{eff}} \leq m_i$ . In this model, the single particle energy for a baryon with momentum  $\vec{p}_i$  can be expressed as

$$E_i(p_i) = \sqrt{p_i^2 + [m_i^{\text{eff}}(n_b)]^2} + U_i(n_b), \quad (4.1)$$

where  $U_i(n_b)$  is the potential induced by the Lorentz vector forces, which depends on the baryon number density. This expression resembles the dispersion relation for a particle of mass  $m_i^{\text{eff}}$  under the influence of an external force with corresponding potential  $U_i$ . Hence, the single-particle energy spectrum of the interacting baryons must be expressed in terms of  $m_i^{\text{eff}}$  rather than the mass in vacuum, and it is this mass that will enter into the kinematics of the scattering processes.

Accounting for the strong interactions in this way leads to several modifications to the results obtained in Chapter 3. Firstly, all appearances of the bare mass  $m_i$  are replaced by  $m_i^{\text{eff}}$  in all the results. This will lead to non-trivial modifications of the capture and interaction rates throughout the star as the mass of the target will decrease deeper into the star (see right panels of Fig. 2.5).

In addition, the Fermi energies,  $\varepsilon_{F,i} = \mu_{F,i} - m_i$ , are now calculated according to

$$\varepsilon_{F,i}(r) = \sqrt{[p_{F,i}(n_i)]^2 + [m_i^{\text{eff}}(r)]^2} - m_i^{\text{eff}}(r), \quad (4.2)$$

where  $p_{F,i}$  is the Fermi momentum of species  $i$ . This becomes the input to the Fermi-Dirac distributions for the capture and interaction rates. In doing this, the number density evaluated in the free Fermi gas approximation, Eq. 3.38, becomes equal to the true number density,  $n_i(r)$ , provided by solving the EoS alongside the TOV equations. To see this, substitute Eq. 4.2 into Eq. 3.38 and make the replacement  $m_i \rightarrow m_i^{\text{eff}}$  to get

$$n_{\text{free}}(\varepsilon_{F,i}(r), m_i^{\text{eff}}(r)) = \frac{1}{3\pi^2} [\varepsilon_{F,i}(r)(2m_i^{\text{eff}} + \varepsilon_{F,i}(r))]^{3/2} \quad (4.3)$$

$$= \frac{(p_{F,i}(r)^2 + [m_i^{\text{eff}}]^2)^{3/2}}{3\pi^2} \quad (4.4)$$

$$= \frac{p_{F,i}^3}{3\pi^2} \quad (4.5)$$

$$= n_i(r) \quad (4.6)$$

for a Fermi gas, interacting or otherwise. As such, the correction factor used to correct for usign realistic profiles for the target is now  $\zeta(r) = 1$ .

In Fig. 4.1 we show the values of the Fermi energies for neutrons (left panel) and protons (right panel). The dashed lines are the radial profiles used in the free Fermi gas approximation and the solid lines correspond to the calculation outlined above for the effective mass approach. We immediately notice that the profiles for

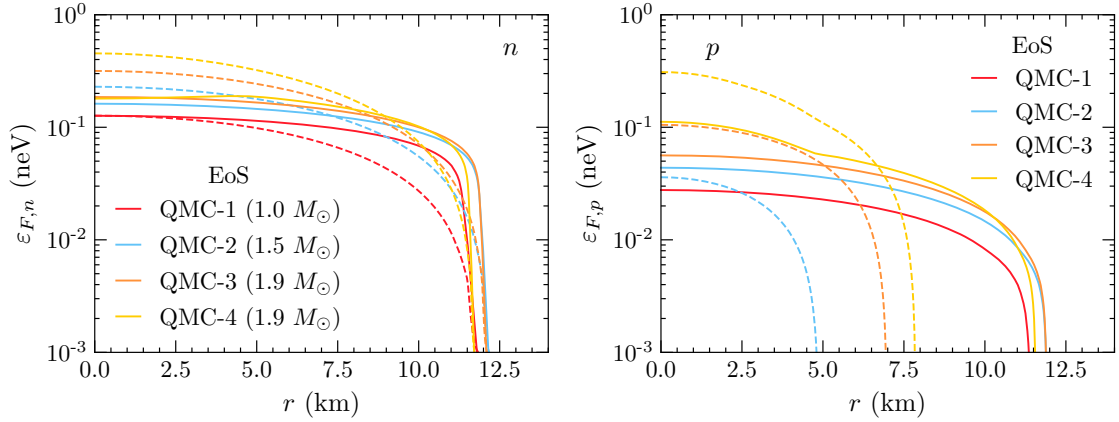


**Figure 4.1:** Radial profiles of the Fermi energy for neutrons (left) and protons (right). Results are shown for the free Fermi gas (dashed) and interacting baryon (solid) approaches, for the benchmark NS configurations of Table 2.3.

the free Fermi gas approximation are steeper, having larger values in the core and decreasing more rapidly towards the surface, while those obtained with the effective mass approach are quite flat, especially in the core, and go to zero only very close to the surface.

The difference between these two calculations is significantly more prominent for protons. Specifically, in the free Fermi gas approach, we find that protons are non-degenerate in the outer regions of the core and, for light NS configurations such as QMC-1, are non-degenerate throughout the whole star.<sup>1</sup> In contrast, protons are degenerate throughout the entire star in the interacting baryon treatment. As we shall see, these different Fermi energies will have important consequences when calculating DM capture and interaction rates, especially for proton targets.

### 4.1.2 Momentum Dependence of Hadronic Form Factors

In the preceding chapters, we had regarded the target as a point-like particle that the DM scattered off, which is perfectly valid for the leptonic species. Baryons on the other hand are composite particles, being composed of three valence quarks and hence having a finite size. When the momentum transfer exceeds the inverse Compton wavelength of the baryon,  $\sim 1/\lambda_B \sim m_B$ , the internal structure begins to be probed, and we must account for their finite size.

As discussed in Section 1.2.4, this is achieved by reintroducing the momentum

<sup>1</sup>Not shown in Fig. 4.1 because of the logarithmic scale.

dependence in the hadronic form factors,

$$c_{\mathcal{B}}^I(t) = c_{\mathcal{B}}^I(0)F^2(t), \quad I \in \{S, P, V, A, T\}, \quad (4.7)$$

$$F(t) = \frac{1}{(1-t/Q_0^2)^2}, \quad (4.8)$$

where  $t$  is the Mandelstam variable,  $Q_0$  is an energy scale taken to be 0.9 GeV, and  $c_{\mathcal{B}}^I(0)$  are the form factors evaluated at zero momentum transfer, with their values given in Appendix B. This factor is included in the matrix elements of the operators in Table 1.1, and as such modifies the analytic result for the interaction rate derived in Section 3.3 for matrix elements  $|\overline{\mathcal{M}}|^2 \propto t^n s^m$  to become

$$\begin{aligned} \Gamma^-(E_\chi) \propto & \frac{(-1)^n}{128\pi^3 E_\chi k} \int_0^{E_\chi - m_\chi} dq_0 \int dt_E \frac{t_E^n}{(t_E + q_0^2)^{m+\frac{1}{2}}} \frac{1}{(1 + t_E/Q_0^2)^4} \\ & \times \sum_{r=0}^m \mathcal{V}_{m,r} \sum_{j=0}^r \binom{r}{j} \varepsilon_{F,i}^{r-j} \frac{(-1)^j q_0^{j+1}}{j+1} h_j \left( \frac{E_i^{t^-} - \varepsilon_{F,i}}{q_0} \right), \end{aligned} \quad (4.9)$$

where  $E_i^{t^-}$  and  $h_j(x)$  are given in Eqs. 3.55 and 3.56 respectively.

The main effect of these form factors is the suppression of high momentum transfer interactions. This will also increase the DM mass range over which Pauli blocking is expected to be active. We can see these effects by examining the kinematically allowed regions of phase space together with the differential interaction rate profiles.

In Fig. 4.2, we show how Pauli blocking affects the integration domain of Eq. 4.9, which is controlled by the smoothed step function  $h_0(x)$ , for some representative choices of DM mass and the benchmark values  $\varepsilon_{F,n} = 0.4$  GeV and  $B = 0.5$ . The region where  $h_0(x) = 0$  is not kinematically allowed and hence not shown in Fig. 4.2. The light blue area represents the region that is not affected by Pauli blocking (PB), i.e.  $h_0(x) = -x$ , while the dark blue shaded area indicates the PB region, where  $h_0(x) = 1$ . We observe that for light DM masses such as  $m_\chi = 0.1$  GeV (top left panel), the whole domain lies in the PB region. For  $m_\chi = 1$  GeV (top right panel), there is a tiny slice of the domain that is not Pauli suppressed. The picture changes dramatically when the DM mass is increased to  $m_\chi = 10$  GeV (bottom left panel), where almost the whole integration domain is unaffected by PB. Increasing the DM mass even further, e.g., up to  $m_\chi = 1$  TeV (bottom right panel) does not result in much further change to the shape of the domain, demonstrating that the transition between the PB and non-PB regimes occurs between  $m_\chi \sim 1$  GeV and  $m_\chi \sim 10$  GeV.

In Fig. 4.3 we show the normalised differential interaction rates for operators D1-D4 as a function of the energy loss  $q_0$ , calculated with (orange) and without (light blue) momentum dependent couplings, for neutron targets and  $m_\chi = 1$  TeV. In all

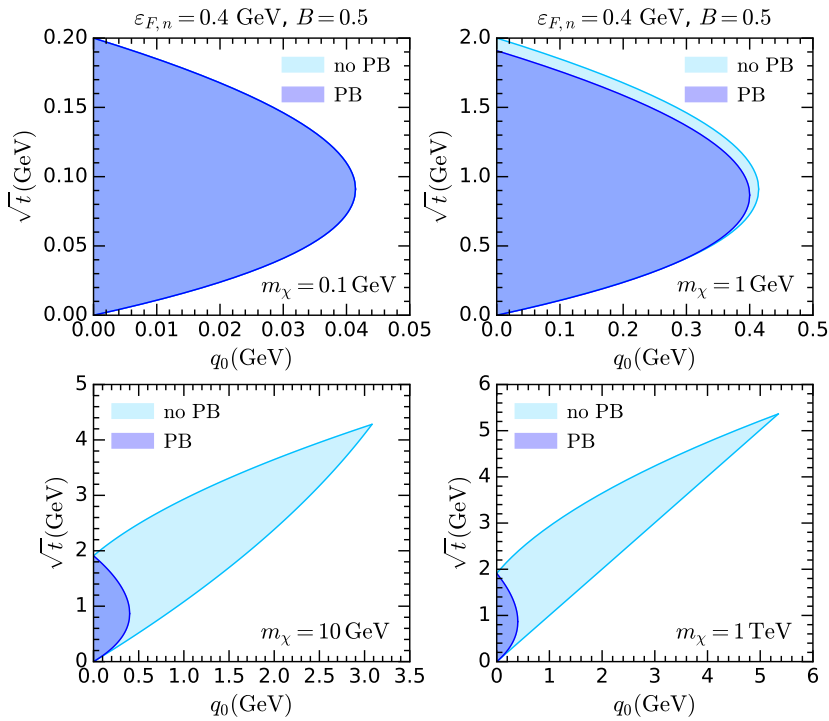


**Figure 4.2:** Integration domain for the interaction rate, for different choices of DM mass, assuming  $B = 0.5$  and  $\varepsilon_{F,n} = 0.4 \text{ GeV}$ . The kinematically allowed region is shaded in light blue and the Pauli suppressed region (PB) in dark blue.

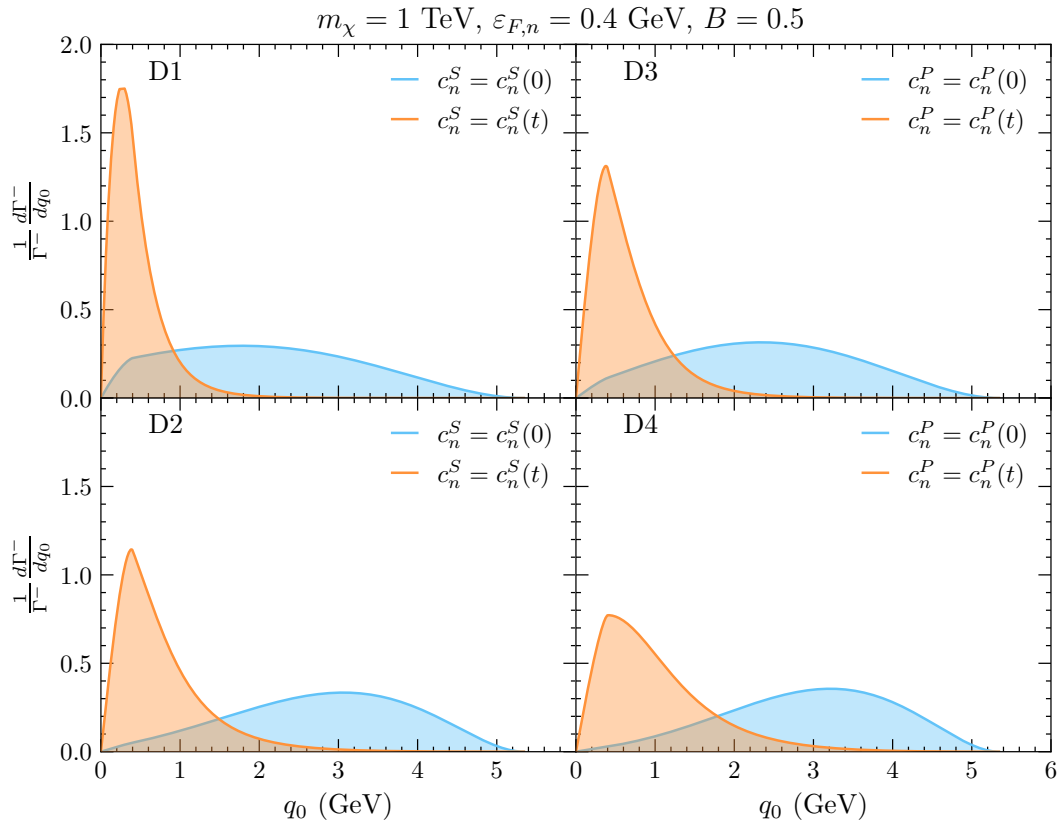


**Figure 4.3:** Normalised differential DM-neutron interaction rate as a function of the DM energy loss,  $q_0$ , for the operators D1 (top left), D3 (top right), D2 (bottom left) and D4 (bottom right). The light blue lines denote the interaction rate calculated using constant neutron form factors  $c_n^S(0)$ ,  $c_n^P(0)$ , while the orange lines correspond to that for momentum-dependent couplings  $c_n^S(t)$ ,  $c_n^P(t)$ . We have set  $m_\chi = 1 \text{ TeV}$ ,  $B = 0.5$ ,  $\varepsilon_{F,n} = 0.4 \text{ GeV}$ .

cases, we observe that the inclusion of  $t$ -dependent hadronic matrix elements shifts the peak of the spectrum towards lower energy transfers,  $q_0$ . Thus, the inclusion of  $c_i^I(t)$  in Eq. 4.9 suppresses DM-neutron interactions at large momentum transfers. Replacing the target mass with the corresponding effective mass  $m_i^{\text{eff}} \leq m_i$  also shifts the average energy transfer to lower energies. When both effects are present, a lighter target mass reduces the suppression arising from  $t$ -dependent form factors.

### Asside: Deep Inelastic Scattering

Given that the momentum transfer in the DM-nucleon scattering process is sufficiently large that we cannot treat the nucleons as point particles (up to  $\sim 10$  GeV in the cores of the heaviest NSs), one may wonder if there are sizable contributions from Deep Inelastic Scattering (DIS). To that end, we examine the contribution from DIS to the total DM-neutron scattering cross-section.

The kinematics of DIS of dark matter in NSs is not similar to any case that has previously been treated in the literature, at least not to our knowledge. In contrast to DIS of neutrinos and boosted DM, we are interested in much larger DM masses and relatively lower energies. Specifically,  $E_\chi/m_\chi = 1/\sqrt{B}$ , where  $B$  is the time component of the Schwarzschild metric, which falls in the range  $[\sim 0.2, \sim 0.75]$ . Therefore, we have  $E_\chi \lesssim 2m_\chi$ . Following ref. [242], we derive the DIS cross-section in NSs for the operators in Table 1.1.

The parton level differential cross-section is given by

$$\frac{d\hat{\sigma}}{d\hat{t}} = \frac{\hat{s}}{8\pi\hat{\gamma}^2} \frac{\hat{s} - (m_\chi^2 + x^2 m_n^2)}{\hat{s}^2 - (m_\chi^2 - x^2 m_n^2)^2} |\overline{\mathcal{M}}(\hat{s}, \hat{t}, m_i = xm_n)|^2, \quad (4.10)$$

where  $\hat{\gamma} = \gamma(\hat{s}, m_\chi, xm_n)$ ,  $\hat{t} = -Q^2$  is the squared 4-momentum transfer,  $\hat{s} = (1-x)(m_\chi^2 - xm_n^2) + xs$ ,  $|\overline{\mathcal{M}}|^2$  is defined at the parton level with couplings  $g_i = g_q$ , and  $x$  is the fraction of the nucleon momentum ( $P$ ) carried by the parton,  $p = xP$ . We define  $y$ , the fractional energy lost by the DM in the nucleon rest frame [242]

$$y = \frac{2q \cdot P}{2k \cdot P} = \frac{-\hat{t}}{\hat{s} - m_\chi^2 - x^2 m_n^2}, \quad (4.11)$$

and obtain

$$dQ^2 = (\hat{s} - m_\chi^2 - x^2 m_n^2) dy = x(s - m_\chi^2 - m_n^2) dy. \quad (4.12)$$

We then use the parton distribution functions (PDFs),  $f_i$ , to obtain the nucleon level differential DIS cross-section

$$\frac{d^2\sigma}{dx dy} = (\hat{s} - m_\chi^2 - x^2 m_n^2) \frac{\hat{s}}{8\pi\hat{\gamma}^2} \frac{\hat{s} - (m_\chi^2 + x^2 m_n^2)}{\hat{s}^2 - (m_\chi^2 - x^2 m_n^2)^2} \sum_i f_i(x, Q^2) |\overline{\mathcal{M}}(\hat{s}, \hat{t}, xm_n)|^2. \quad (4.13)$$

The integration bounds for the DIS cross-section are generically  $0 < x < 1$  and  $0 < y < y_{max}$ , where  $y_{max}$  is set by imposing  $\cos \theta \leq 1$ , and in general  $y_{max} \neq 1$  [242]. The value of  $y_{max}$  is set by

$$y_{max} = \frac{-\hat{t}_{min}}{\hat{s} - m_\chi^2 - x^2 m_n^2} = \frac{(\hat{s} - m_\chi^2 - x^2 m_n^2)^2 - 4x^2 m_\chi^2 m_n^2}{\hat{s}(\hat{s} - m_\chi^2 - x^2 m_n^2)}. \quad (4.14)$$

The capture rate requires integrating the differential cross-section over  $\hat{s}$ , which must be done at the parton level, i.e., before integrating over  $x$ . We perform this integration over the centre of mass energy by following the same procedure performed for capture in the intermediate mass regime outlined in Section 3.4.1. The differential capture rate will then scale as

$$\frac{dC}{dr} \propto \int_0^1 dx \int_{\hat{s}_0 - \delta\hat{s}}^{\hat{s}_0 + \delta\hat{s}} d\hat{s} \int_0^{y_{max}} dy \frac{d^2\sigma}{dx dy} \Theta(Q^2 - 1 \text{ GeV}^2), \quad (4.15)$$

where the step function enforces the momentum transfer to be above the 1 GeV threshold where the PDFs are reliable, and

$$\hat{s}_0 = m_\chi^2 + 2xE_n E_\chi, \quad (4.16)$$

$$\delta\hat{s} = 2xm_\chi \sqrt{E_n^2 - m_n^2} \sqrt{\frac{1 - B(r)}{B(r)}}, \quad (4.17)$$

$$E_n \simeq m_n + \mu_{F,n}. \quad (4.18)$$

We numerically evaluate the DIS cross-section using the MSTW2008 NLO PDFs [243].

In Fig. 4.4, we show the ratios of the elastic (EL) and deep inelastic scattering (DIS) cross-sections to the total cross-section (TOT=DIS+EL), as a function of the radial coordinate  $r$  for the NS QMC-4, neutron targets and  $m_\chi = 10^6$  GeV. We consider two scenarios: the free Fermi gas approach and the interactive baryon approach characterised by  $m_n^{\text{eff}}$ . The radial coordinate determines the value of  $B$ , the Fermi energy of the target, and  $m_n^{\text{eff}}$ .

In both the  $m_n^{\text{eff}}$  and free Fermi gas approaches, the DIS contribution (light blue and green lines, respectively) increases towards the centre of the star, where  $B$  takes lower values and hence the DM kinetic energy is higher. The ratio  $\sigma^{\text{DIS}}/\sigma^{\text{TOT}}$  is smaller in the  $m_n^{\text{eff}}$  approach, compared to the free Fermi gas approach, due to a smaller neutron effective mass. In the correct interactive baryon approach, the ratio of the DIS contribution (light blue lines) to the total cross-section is at most  $\mathcal{O}(40\%)$  at the centre of the star for D8,  $\mathcal{O}(20\%)$  for D7, D9-D10, and much lower for the remaining operators.

As a result, for most operators, the elastic cross-section provides a very good approximation to the total cross-section (compare magenta with dashed blue lines). Note that these cross-sections are weighted by  $r^2 dr$  in the capture rate calculation

of Eq. ?? (i.e. weighted by volume) which further reduces the importance of the DIS contribution.

It is worth noting that we have neglected the effect of Pauli blocking on the DIS cross-section. In deep inelastic scattering, one must have a baryon in the final state and with a nucleon target this is almost always a nucleon. As shown in both theoretical calculations [244] and direct experimental studies [245], this nucleon has low momentum in the laboratory frame, typically 300 MeV or less. Such nucleons will be totally Pauli blocked in the core of a NS, and hence the deep inelastic cross-section drastically reduced. As a result, the contribution of the deep inelastic process to the capture rate will have a negligible effect on our conclusions.

We performed a similar calculation for hyperon targets and found that as for neutrons, the DIS contribution to the total cross-section is more important for operators D7-D10 in the absence of Pauli blocking of the fragmented baryonic final states. For D8 and  $\Xi^-$  targets, the DIS cross-section can even surpass the elastic scattering contribution (including form factors) and reach  $\sim 60\%$  of the total cross-section at the centre of the star.  $\Xi^-$  provides the largest hyperonic contribution to the capture rate, however, this (elastic scattering) contribution is already more than one order of magnitude lower than that of neutrons for D7-D10. Even if Pauli blocking does not suppress the DIS final states, the contribution of the deep inelastic process to the capture of DM is negligible, since it would enhance the capture rate by scattering on  $\Xi^-$  at most by a factor of  $\sim 2$ .

In addition to DIS, there may, in principle, be a contribution from the excitation of baryon resonances. However, the resonance excitation cross-section is also expected to be suppressed. In NSs, the mass of the  $\Delta$  baryon, which gives the largest contribution to this cross-section, increases with the baryon number density by between  $\sim 100$  and 300 MeV [246]. This will suppress the resonance excitation cross-section significantly. Therefore, we consider only elastic collisions.

## 4.2 Results from Capture on Baryons

## 4.3 Threshold Cross-Sections for Nucleon Scattering

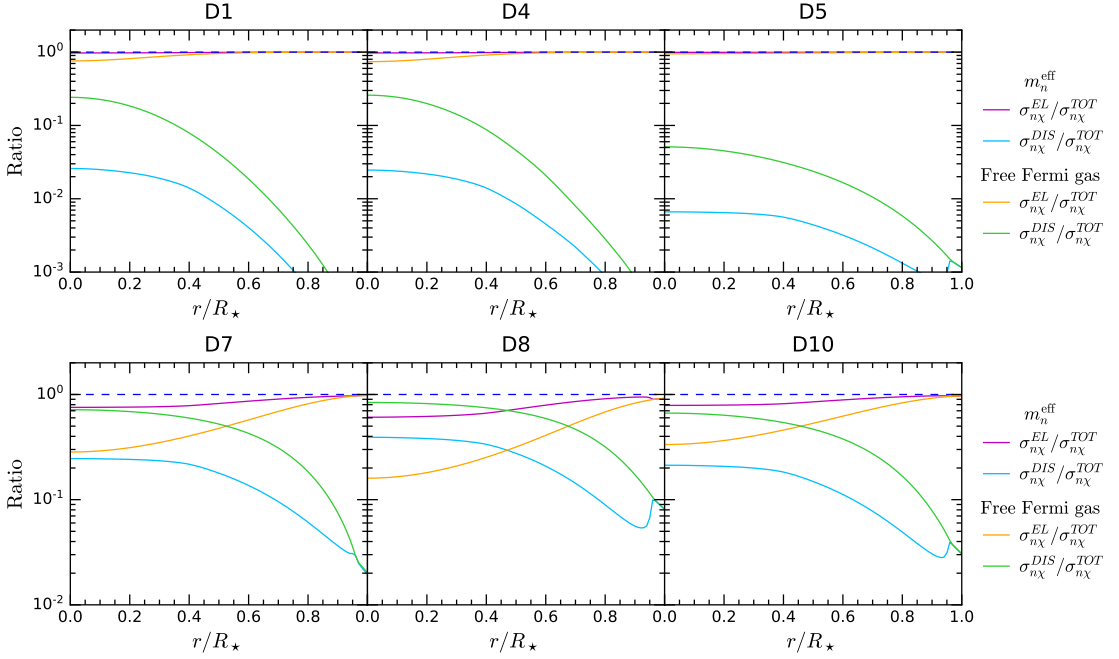


**Figure 4.4:** Ratios of the elastic (EL) and deep inelastic scattering (DIS) cross-sections to the total cross-section ( $\text{TOT} = \text{EL} + \text{DIS}$ ) as a function of the NS radius, for neutron targets in the NS QMC-4 and six of the dimension-6 EFT operators. We have taken  $m_\chi = 10^6 \text{ GeV}$ , and shown the comparison for both the interacting baryon and free Fermi gas approaches. Momentum-dependent form factors have been included in the elastic calculations.

# A

## Dark Matter Interaction Rates

### A.1 General Interaction Rates for Scattering within a Degenerate Media

The most general form of the interaction rate, following Ref. [118], can be written in terms of the spin-averaged squared matrix element,  $|\bar{\mathcal{M}}|^2$ , as

$$\Gamma = \int \frac{d^3 k'}{(2\pi)^3} \frac{1}{(2E_\chi)(2E'_\chi)(2m_i)(2m_i)} \Theta(E'_\chi - m_\chi) \Theta(\pm q_0) S(q_0, q), \quad (\text{A.1})$$

$$S(q_0, q) = 2 \int \frac{d^3 p}{(2\pi)^3} \int \frac{d^3 p'}{(2\pi)^3} \frac{m_i^2}{E_i E'_i} |\bar{\mathcal{M}}|^2 (2\pi)^4 \delta^4(k_\mu + p_\mu - k'_\mu - p'_\mu) \\ \times f_{\text{FD}}(E_i)(1 - f_{\text{FD}}(E'_i)) \Theta(E_i - m_i) \Theta(E'_i - m_i), \quad (\text{A.2})$$

where  $S(q_0, q)$  is the target response function that depends on the energy and momentum transfers,  $q_0$  and  $q$  respectively.  $E_\chi$  and  $E_i$  are the DM and target initial energies, with  $k$  and  $p$  their respective momenta. Primed variables represent final state quantities.

The  $\delta$ -function can be used to perform the  $d^3 p'$  integrations, leaving

$$S(q_0, q) = \frac{1}{2\pi^2} \int d^3 p \frac{m_i^2}{E_i E'_i} |\bar{\mathcal{M}}|^2 \delta(q_0 + E_i - E'_i) f_{\text{FD}}(E_i)(1 - f_{\text{FD}}(E'_i)) \\ \times \Theta(E_i - m_i) \Theta(E'_i - m_i). \quad (\text{A.3})$$

After this, the final state target energy is fixed to

$$E'_i(E_i, q, \theta) = \sqrt{m_i^2 + (\vec{p} + \vec{q})^2} \quad (\text{A.4})$$

$$= \sqrt{E_i^2 + q^2 + 2qp \cos \theta} > m_i, \quad \forall p, q, \theta, |\cos \theta| < 1, \quad (\text{A.5})$$

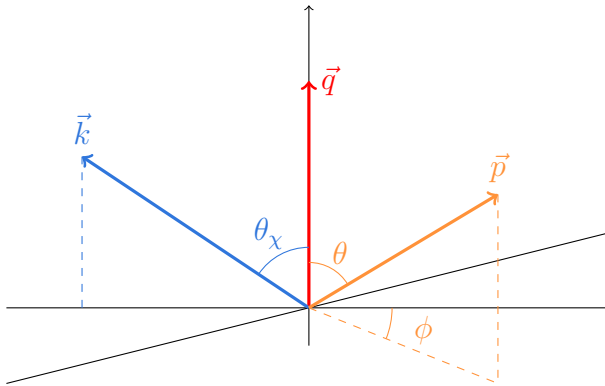


**Figure A.1:** Schematic of kinematics for dark matter interacting with a target in the frame of the star. We set the momentum transfer to lie along the  $z$ -axis with the initial momenta defined relative to it.

where  $\theta$  is the angle between the target initial momentum and the transferred momentum,  $\vec{q}$ , that is defined below. To perform the remaining integrals, we write  $d^3p = pE_idE_i d\cos\theta d\phi$ . The kinematics of this interaction are depicted in Fig. A.1, where the incoming momenta are defined relative to the momentum transfer that is set to lie along the  $z$ -axis. In doing so, we must account for the fact that in this frame we cannot assume all three of the vectors are coplanar, and assign the additional azimuthal angle  $\phi$  to the target momentum.

In general, the squared matrix elements we are interested in can be expressed as polynomials in the Mandelstam variables  $s$  and  $t$ , such that

$$|\overline{\mathcal{M}}|^2 = \sum_{n,m} \alpha_{n,m} t^n s^m. \quad (\text{A.6})$$

Writing  $s = m_\chi^2 + m_i^2 + 2E_\chi E_i - 2\vec{p} \cdot \vec{k}$ , the quantity  $\vec{k} \cdot \vec{p}$  is obtained by analysing the kinematics of the interaction. From the diagram in Fig. A.1, we can write the initial momenta as

$$\vec{k} = (k \sin \theta_\chi, 0, k \cos \theta_\chi), \quad (\text{A.7})$$

$$\vec{p} = (p \sin \theta \cos \phi, p \sin \theta \sin \phi, p \cos \theta). \quad (\text{A.8})$$

The angles can then be expressed in terms of the other kinematic quantities by

noting that

$$E'_\chi = \sqrt{m_\chi^2 + (\vec{k} - \vec{q})}, \quad (\text{A.9})$$

$$\implies (E_\chi - q_0)^2 = m_\chi^2 + (k^2 + q^2 - 2kq \cos \theta_\chi) \quad (\text{A.10})$$

$$\implies \cos \theta_\chi = \frac{q^2 - q_0^2 + 2E_\chi q_0}{2q \sqrt{E_\chi^2 - m_\chi^2}}, \quad (\text{A.11})$$

$$E'_i = \sqrt{m_i^2 + (\vec{p} + \vec{q})}, \quad (\text{A.12})$$

$$(\text{A.13})$$

for the dark matter angle, and

$$\implies (E_i + q_0)^2 = m_i^2 + (p^2 + q^2 + 2pq \cos \theta) \quad (\text{A.14})$$

$$\implies \cos \theta = \frac{q_0^2 - q^2 + 2E_i q_0}{2q \sqrt{E_i^2 - m_i^2}} \quad (\text{A.15})$$

for the target angle. These result in

$$\vec{k} \cdot \vec{p} = kp \sin \theta_\chi \sin \theta \cos \phi + kp \cos \theta_\chi \cos \theta \quad (\text{A.16})$$

$$\begin{aligned} &= kp \left[ \sqrt{1 - \frac{(q^2 - q_0^2 + 2E_\chi q_0)^2}{4q^2(E_\chi^2 - m_\chi^2)}} \sqrt{1 - \frac{(q_0^2 - q^2 + 2E_i q_0)^2}{4q^2(E_i^2 - m_i^2)}} \cos \phi \right. \\ &\quad \left. + \frac{(q^2 - q_0^2 + 2E_\chi q_0)(q_0^2 - q^2 + 2E_i q_0)}{4q^2 \sqrt{E_\chi^2 - m_\chi^2} \sqrt{E_i^2 - m_i^2}} \right] \end{aligned} \quad (\text{A.17})$$

$$\begin{aligned} &= \frac{(q^2 - q_0^2 + 2E_\chi q_0)(q_0^2 - q^2 + 2E_i q_0)}{4q^2} \\ &\quad + \sqrt{E_\chi^2 - m_\chi^2 - \frac{(q^2 - q_0^2 + 2E_\chi q_0)^2}{4q^2}} \sqrt{E_i^2 - m_i^2 - \frac{(q_0^2 - q^2 + 2E_i q_0)^2}{4q^2}} \cos \phi. \end{aligned} \quad (\text{A.18})$$

This makes explicit that  $s$  is now a function of the azimuthal angle  $\phi$ .

We then use the remaining delta function to integrate over  $\theta$ , giving rise to a step function  $\Theta(1 - \cos^2 \theta(q, q_0, E_i))$ , leaving the

$$S(q_0, q) = \alpha t^n \frac{m_i^2}{2\pi^2 q} \int dE_i d\phi s^m f_{\text{FD}}(E_i) (1 - f_{\text{FD}}(E_i + q_0)) \Theta(E_i) \Theta(1 - \cos^2 \theta). \quad (\text{A.19})$$

It will be more convenient to work with the kinetic energies of the targets rather than their total energies, as we are only interested in elastic scattering. From here on out,  $E_i$  will refer to the kinetic energy of the target, i.e.  $E_i \rightarrow E_i + m_i$ .

This is compensated by using the Fermi kinetic energy in the FD distributions,  $\varepsilon_{F,i} = \mu_{F,i} - m_i$ .

The  $\phi$  integrals can be easily computed for a given power of  $s$ , in general resulting in a messy function of the kinematic variables. However, we know that they will always be a polynomial of degree  $m$ , and so to make this explicit while keeping things as tidy as possible, we define the polynomials  $\mathcal{U}_m(q^2, q_0, E_\chi, E_i)$  as

$$\mathcal{U}_m = \frac{q^{2m}}{2\pi} \int_0^{2\pi} d\phi s^m = \sum_r \mathcal{V}_{m,r} E_i^r \quad (\text{A.20})$$

where the coefficients of the polynomial,  $\mathcal{V}_{m,r}$ , are functions of  $q^2, q_0$ , and  $E_\chi$ . The response function is then

$$S(q_0, q) = \alpha t^n \frac{m_i^2}{\pi q} \int dE_i f_{\text{FD}}(E_i) (1 - f_{\text{FD}}(E_i + q_0)) \frac{\mathcal{U}_m}{q^{2m}} \Theta(E_i) \Theta(1 - \cos^2 \theta). \quad (\text{A.21})$$

Therefore, the integrals we are interested in computing are over the FD distributions, which we call

$$\mathcal{F}_r(E_i, q_0) = \int dE_i E_i^r f_{\text{FD}}(E_i) (1 - f_{\text{FD}}(E_i + q_0)). \quad (\text{A.22})$$

To proceed, make the change to the dimensionless variables

$$x = \frac{E_i - \varepsilon_{F,i}}{T_\star}, \quad z = \frac{q_0}{T_\star}, \quad (\text{A.23})$$

which we can use to write

$$\mathcal{F}_r(E_i, q_0) = T_\star \int dx (\varepsilon_{F,i} + T_\star x)^r f_{\text{FD}}(x) f_{\text{FD}}(-x - z) \quad (\text{A.24})$$

$$= T_\star \int dx \sum_{j=0}^r \binom{r}{j} T_\star^j x^j \varepsilon_{F,i}^{r-j} f_{\text{FD}}(x) f_{\text{FD}}(-x - z) \quad (\text{A.25})$$

$$= \sum_{j=0}^r T_\star^{j+1} \binom{r}{j} \varepsilon_{F,i}^{r-j} \int dx x^j f_{\text{FD}}(x) f_{\text{FD}}(-x - z) \quad (\text{A.26})$$

$$= \sum_{j=0}^r \binom{r}{j} \varepsilon_{F,i}^{r-j} \int dE_i (E_i - \varepsilon_{F,i})^j f_{\text{FD}}(E_i) f_{\text{FD}}(-E_i - q_0) \quad (\text{A.27})$$

$$= \sum_{j=0}^r \binom{r}{j} \varepsilon_{F,i}^{r-j} (-1)^j \frac{q_0^{j+1}}{j+1} g_j \left( \frac{E_i - \varepsilon_{F,i}}{q_0} \right), \quad \text{for } T_\star \rightarrow 0, \quad (\text{A.28})$$

where the final line holds in the zero-temperature approximation in which the FD distributions become  $\Theta$ -functions, allowing the integrals to be expressed in terms of the function

$$g_j(x) = \begin{cases} 1, & x > 0 \\ 1 - (-x)^{j+1}, & -1 < x < 0 \\ 0, & x < -1 \end{cases} \quad (\text{A.29})$$

The integration range for  $E_i$  is obtained from the two  $\Theta$ -functions. There are two cases to be considered,  $t < 0$  and  $t > 0$ . In the former case, the range become  $E_i^{t^-} < E_i < \infty$  and for the latter  $0 < E_i < E_i^{t^+}$ . These integration bounds are obtained from Eq. A.15, by settting  $\cos \theta = 1$ , and are given by

$$E_i^{t^-} = -\left(m_i + \frac{q_0}{2}\right) + \sqrt{\left(m_i + \frac{q_0}{2}\right)^2 + \left(\frac{\sqrt{q^2 - q_0^2}}{2} - \frac{m_i q_0}{\sqrt{q^2 - q_0^2}}\right)^2} \quad (\text{A.30})$$

$$E_i^{t^+} = -\left(m_i + \frac{q_0}{2}\right) + \sqrt{\left(m_i + \frac{q_0}{2}\right)^2 - \left(\frac{\sqrt{q_0^2 - q^2}}{2} + \frac{m_i q_0}{\sqrt{q_0^2 - q^2}}\right)^2}. \quad (\text{A.31})$$

These are both the same root of Eq. A.15, but with an interchange of  $t \leftrightarrow -t$ . We denote the response function for  $t < 0$  as  $S^-$  and for  $t > 0$  as  $S^+$ . For  $S^-$  we have

$$S_m^- = \alpha t^n \frac{m_i^2}{\pi q^{2m+1}} \sum_{r=0}^m \mathcal{V}_{m,r} \int_{E_i^{t^-}}^{\infty} dE_i E_i^r f_{\text{FD}}(E_i) (1 - f_{\text{FD}}(E_i + q_0)) \quad (\text{A.32})$$

$$= \alpha t^n \frac{m_i^2}{\pi q^{2m+1}} \sum_{r=0}^m \mathcal{V}_{m,r} \sum_{j=0}^r \binom{r}{j} \varepsilon_{F,i}^{r-j} \int_{E_i^{t^-}}^{\infty} dE_i (E_i - \varepsilon_{F,i})^j f_{\text{FD}}(E_i) f_{\text{FD}}(-E_i - q_0) \quad (\text{A.33})$$

$$= \alpha t^n \frac{m_i^2}{\pi q^{2m+1}} \sum_{r=0}^m \mathcal{V}_{m,r} \sum_{j=0}^r \binom{r}{j} \varepsilon_{F,i}^{r-j} \frac{(-1)^j q_0^{j+1}}{j+1} \left[ 1 - g_j \left( \frac{E_i^{t^-} - \varepsilon_{F,i}}{q_0} \right) \right] \quad (\text{A.34})$$

$$= \alpha t^n \frac{m_i^2}{\pi q^{2m+1}} \sum_{r=0}^m \mathcal{V}_{m,r} \sum_{j=0}^r \binom{r}{j} \varepsilon_{F,i}^{r-j} \frac{(-1)^j q_0^{j+1}}{j+1} h_j \left( \frac{E_i^{t^-} - \varepsilon_{F,i}}{q_0} \right), \quad (\text{A.35})$$

while for  $S^+$  the logic is

$$S_m^+ = \alpha t^n \frac{m_i^2}{\pi q^{2m+1}} \sum_{r=0}^m \mathcal{V}_{m,r} \int_0^{E_i^{t^+}} dE_i E_i^r f_{\text{FD}}(E_i) (1 - f_{\text{FD}}(E_i + q_0)) \quad (\text{A.36})$$

$$= \alpha t^n \frac{m_i^2}{\pi q^{2m+1}} \sum_{r=0}^m \mathcal{V}_{m,r} \sum_{j=0}^r \binom{r}{j} \varepsilon_{F,i}^{r-j} \int_0^{E_i^{t^+}} dE_i (E_i - \varepsilon_{F,i})^j f_{\text{FD}}(E_i) f_{\text{FD}}(-E_i - q_0) \quad (\text{A.37})$$

$$= \alpha t^n \frac{m_i^2}{\pi q^{2m+1}} \sum_{r=0}^m \mathcal{V}_{m,r} \sum_{j=0}^r \binom{r}{j} \varepsilon_{F,i}^{r-j} \frac{(-1)^j q_0^{j+1}}{j+1} \left[ g_j \left( \frac{E_i^{t^+} - \varepsilon_{F,i}}{q_0} \right) - g_j \left( \frac{-\varepsilon_{F,i}}{q_0} \right) \right] \quad (\text{A.38})$$

$$= -\alpha t^n \frac{m_i^2}{\pi q^{2m+1}} \sum_{r=0}^m \mathcal{V}_{m,r} \sum_{j=0}^r \binom{r}{j} \varepsilon_{F,i}^{r-j} \frac{(-1)^j q_0^{j+1}}{j+1} h_j \left( \frac{E_i^{t^+} - \varepsilon_{F,i}}{q_0} \right) \quad \text{for } q_0 < 0, \quad (\text{A.39})$$

with

$$h_j(x) = \begin{cases} 0, & x > 0 \\ (-x)^{j+1}, & -1 < x < 0 \\ 1, & x < -1 \end{cases} \quad (\text{A.40})$$

The final step of the  $S^+$  calculation holds only for up-scattering of the DM, i.e.  $q_0 < 0$ .

For matrix elements that are polynomials in  $s$  and  $t$ , the full response function is simply the sum of the  $n$  and  $m$ , giving

$$S^- = \sum_{n,m} \alpha_{n,m} t^n \frac{m_i^2}{\pi q^{2m+1}} \sum_{r=0}^m \mathcal{V}_{m,r} \sum_{j=0}^r \binom{r}{j} \varepsilon_{F,i}^{r-j} \frac{(-1)^j q_0^{j+1}}{j+1} h_j \left( \frac{E_i^{t^-} - \varepsilon_{F,i}}{q_0} \right) \quad (\text{A.41})$$

$$S^+ = - \sum_{n,m} \alpha_{n,m} t^n \frac{m_i^2}{\pi q^{2m+1}} \sum_{r=0}^m \mathcal{V}_{m,r} \sum_{j=0}^r \binom{r}{j} \varepsilon_{F,i}^{r-j} \frac{(-1)^j q_0^{j+1}}{j+1} h_j \left( \frac{E_i^{t^+} - \varepsilon_{F,i}}{q_0} \right) \quad (\text{A.42})$$

## A.2 Elsatic Scattering

### A.2.1 Down-scattering Rate

Returning to the scattering rate, we first look at the case of down-scattering, where the DM loses energy,  $q_0 > 0$ . In this case, the interaction rate is given by

$$\begin{aligned} \Gamma^-(E_\chi) = & \int \frac{d \cos \theta_\chi k'^2 dk'}{64\pi^3 E_\chi E'_\chi} \Theta(E_\chi - q_0 - m_\chi) \Theta(q_0) \sum_{n,m} \frac{\alpha_{n,m} t^n}{q^{2m+1}} \\ & \times \sum_{r=0}^m \mathcal{V}_{m,r} \sum_{j=0}^r \binom{r}{j} \varepsilon_{F,i}^{r-j} \frac{(-1)^j q_0^{j+1}}{j+1} h_j \left( \frac{E_i^{t^-} - \varepsilon_{F,i}}{q_0} \right) \end{aligned} \quad (\text{A.43})$$

Change variables to  $q_0$  and  $q$  through

$$q_0 = E_\chi - \sqrt{k'^2 + m_\chi^2}, \quad (\text{A.44})$$

$$q^2 = k^2 + k'^2 - 2kk' \cos \theta_\chi, \quad (\text{A.45})$$

$$\implies dk' d \cos \theta_\chi = \frac{E'_\chi q}{kk'^2} dq_0 dq \quad (\text{A.46})$$

To further simplify the notation we introduce  $t_E = -t = q^2 - q_0^2$ ,  $dq = dt_E/(2q)$ , and exchange the  $q$ -integral for

$$\implies dk' d \cos \theta_\chi = \frac{E'_\chi}{2kk'^2} dq_0 dt_E, \quad (\text{A.47})$$

giving the interaction rate as

$$\begin{aligned} \Gamma^-(E_\chi) = & \frac{1}{128\pi^3 E_\chi k} \int_0^{E_\chi - m_\chi} dq_0 \int dt_E \sum_{n,m} \frac{\alpha_{n,m} (-1)^n t_E^n}{(t_E + q_0^2)^{m+\frac{1}{2}}} \\ & \times \sum_{r=0}^m \mathcal{V}_{m,r} \sum_{j=0}^r \binom{r}{j} \varepsilon_{F,i}^{r-j} \frac{(-1)^j q_0^{j+1}}{j+1} h_j \left( \frac{E_i^{t^-} - \varepsilon_{F,i}}{q_0} \right) \end{aligned} \quad (\text{A.48})$$

$$\begin{aligned} = & \sum_{n,m} \frac{(-1)^n \alpha_{n,m}}{128\pi^3 E_\chi k} \int_0^{E_\chi - m_\chi} dq_0 \int \frac{dt_E t_E^n}{(t_E + q_0^2)^{m+\frac{1}{2}}} \\ & \times \sum_{r=0}^m \mathcal{V}_{m,r} \sum_{j=0}^r \binom{r}{j} \varepsilon_{F,i}^{r-j} \frac{(-1)^j q_0^{j+1}}{j+1} h_j \left( \frac{E_i^{t^-} - \varepsilon_{F,i}}{q_0} \right). \end{aligned} \quad (\text{A.49})$$

There are then two main cases to consider; when  $h_j(x)$  is unity or when it is not. We denote the  $t_E$  integrand in the former case as  $f_1$  and  $f_2$  for the latter, given explicitly as

$$f_1^{(m,n)}(t_E) = \frac{t_E^n}{(t_E + q_0^2)^{m+\frac{1}{2}}} \sum_{r=0}^m \mathcal{V}_{m,r} \sum_{j=0}^r \binom{r}{j} \varepsilon_{F,i}^{r-j} \frac{(-1)^j q_0^{j+1}}{j+1}, \quad (\text{A.50})$$

$$f_2^{(m,n)}(t_E) = \frac{-t_E^n}{(t_E + q_0^2)^{m+\frac{1}{2}}} \sum_{r=0}^m \mathcal{V}_{m,r} \sum_{j=0}^r \binom{r}{j} \varepsilon_{F,i}^{r-j} \frac{1}{j+1} \left( E_i^{t^-} - \varepsilon_{F,i} \right)^{j+1}, \quad (\text{A.51})$$

where we suppress the explicit dependence on the other variables for brevity. We encode the integrals over  $t_E$  within an operator

$$\begin{aligned} \mathcal{I}_{n,m}(f^{(m,n)}(t), t_1^+, t_2^+, t_1^-, t_2^-) &= \sum_{i=1,2} \sum_{j=1,2} \left( F^{(m,n)}(t_i^+) - F^{(m,n)}(t_j^-) \right) \\ &\quad \times \Theta(t_{3-i}^+ - t_i^+) \Theta(t_i^+ - t_j^-) \Theta(t_j^- - t_{3-j}^-), \end{aligned} \quad (\text{A.52})$$

$$F^{(m,n)}(t) = \int dt f^{(m,n)}(t). \quad (\text{A.53})$$

The full interaction rate is then written as

$$\begin{aligned} \Gamma^-(E_\chi) &= \sum_{n,m} \frac{(-1)^n \alpha_{n,m}}{128\pi^3 E_\chi k} \int_0^{E_\chi - m_\chi} dq_0 \\ &\quad \times \left[ \mathcal{I}_{n,m} \left( f_1^{(m,n)}(t), t_E^+, t_{\mu^-}^+, t_E^-, t_{\mu^-}^- \right) \Theta(\varepsilon_{F,i} - q_0) \right. \\ &\quad + \mathcal{I}_{n,m} \left( f_2^{(m,n)}(t), t_E^+, t_{\mu^+}^+, t_E^-, t_{\mu^+}^- \right) \Theta(\varepsilon_{F,i} - q_0) \\ &\quad + \mathcal{I}_{n,m} \left( f_2^{(m,n)}(t), t_E^+, t_{\mu^-}^-, t_E^-, t_{\mu^+}^- \right) \Theta(\varepsilon_{F,i} - q_0) \\ &\quad \left. + \mathcal{I}_{n,m} \left( f_2^{(m,n)}(t), t_E^+, t_{\mu^+}^+, t_E^-, t_{\mu^+}^- \right) \Theta(q_0 - \varepsilon_{F,i}) \right], \end{aligned} \quad (\text{A.54})$$

where the  $t_E$  integration limits are

$$t_E^\pm = 2 \left[ E_\chi(E_\chi - q_0) - m_\chi^2 \pm k \sqrt{(E_\chi - q_0)^2 - m_\chi^2} \right], \quad (\text{A.55})$$

$$\begin{aligned} t_{\mu^+}^\pm &= 2 [\varepsilon_{F,i}(\varepsilon_{F,i} + q_0) + m_i(2\varepsilon_{F,i} + q_0) \\ &\quad \pm \sqrt{(\varepsilon_{F,i}(\varepsilon_{F,i} + q_0) + m_i(2\varepsilon_{F,i} + q_0))^2 - m_i^2 q_0^2}], \end{aligned} \quad (\text{A.56})$$

$$\begin{aligned} t_{\mu^-}^\pm &= 2 [\varepsilon_{F,i}(\varepsilon_{F,i} - q_0) + m_i(2\varepsilon_{F,i} - q_0) \\ &\quad \pm \sqrt{(\varepsilon_{F,i}(\varepsilon_{F,i} - q_0) + m_i(2\varepsilon_{F,i} - q_0))^2 - m_i^2 q_0^2}], \end{aligned} \quad (\text{A.57})$$

All interaction rate spectra will have an endpoint at  $q_0 = q_0^{\text{MAX}}$ , the maximum amount of energy that can be lost in a single interaction. The value of  $q_0^{\text{MAX}}$  is shown in the left panel of Fig. 3.2 as a function of  $B$  in the case of large DM mass ( $m_\chi = 1 \text{ TeV}$ ), for several values of  $\varepsilon_{F,n}$ . The endpoint can be found as the minimum between the DM kinetic energy and the root of one of the following two equations

$$t_E^- = t_{\mu^+}^+, \quad (\text{A.58})$$

$$t_E^+ = t_{\mu^+}^-. \quad (\text{A.59})$$

Only one of these equations will have a positive root for a given choice of  $m_\chi$ ,  $\varepsilon_{F,n}$  and  $E_\chi$ . For  $m_\chi \gg m_i$ , the second equation never has a solution, and the solution of the first equation is always much lower than the kinetic energy. This results in the value of  $q_0^{\text{MAX}}$  becoming independent of  $m_\chi$  in this mass range.

The shape of the differential interaction rate depends very weakly on  $m_\chi$  and  $B$  for  $m_\chi \gg m_i$  and  $m_\chi \ll m_i$ , as seen by plotting it as a function of  $q_0^{\text{norm}} = q_0/q_0^{\text{MAX}}$ . Therefore, we use as a reference  $m_\chi = 1 \text{ TeV}$  (left) and  $m_\chi = 10 \text{ MeV}$  (right),  $B = 0.5$ , and show the normalised differential interaction rates in Fig. A.2 for  $n = 0, 1, 2$ , and neutron targets. We observe in the left panels that for  $n = 0$  interaction rates are flat (or peaked, depending on  $\varepsilon_{F,n}$ ) at low energy and suppressed at high energies, while for  $n = 1, 2$  the profiles become peaked at higher and higher energies. Conversely, for  $m_\chi = 10 \text{ MeV}$  the peak of the spectrum is shifted to lower energies with increasing power of  $t$  ( $d\sigma \propto t^n$ ).

### A.2.2 Up-scattering Rate

We now treat the case of  $q_0 < 0$ , applicable to up scattering and evaporation. Focusing on  $s$ -independent matrix elements for the moment, the response function is

$$S_{\text{up}}^-(q_0, q) = \frac{m_i^2}{\pi q} \int_{E_i^{t-}}^{\infty} f_{\text{FD}}(E_i) (1 - f_{\text{FD}}(E_i - |q_0|)) \quad (\text{A.60})$$

and evaluate the integral, now with  $q_0 < 0$ . If we attempt to take the  $T_* \rightarrow 0$  limit as before, we find that there is no overlap of the FD distributions and the result vanishes. Instead, we keep the leading order thermal corrections, i.e. terms of order  $e^{-|q_0|/T_*}$ . The result is

$$\mathcal{F}_0(E_i, -|q_0|) = \frac{T_* e^{-|q_0|/T_*}}{1 - e^{-|q_0|/T_*}} [\log(1 + e^{(E_i - \varepsilon_{F,i})/T_*}) - \log(1 + e^{(E_i - |q_0| - \varepsilon_{F,i})/T_*})], \quad (\text{A.61})$$

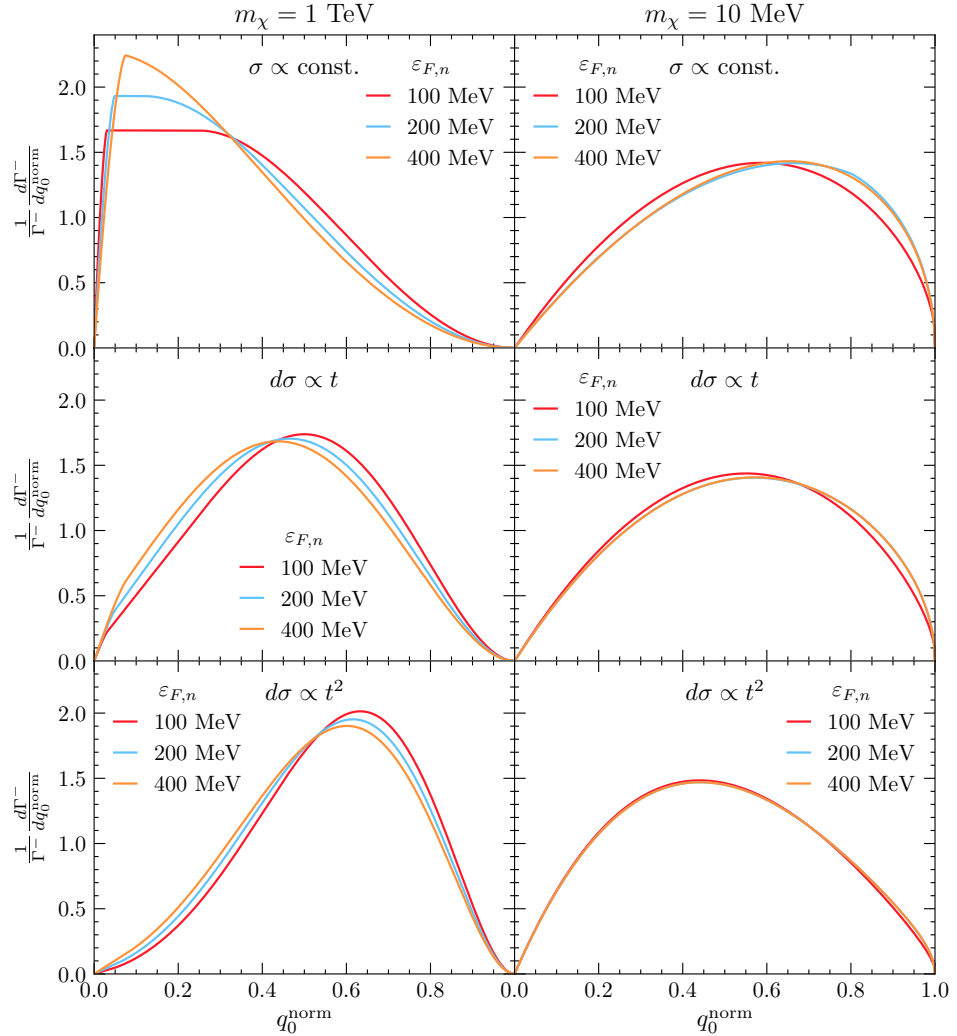


**Figure A.2:** Normalised differential interaction rates,  $\frac{1}{\Gamma} \frac{d\Gamma^-}{dq_0^{\text{norm}}}$ , as a function of  $q_0^{\text{norm}}$  for different values of  $\varepsilon_{F,n}$ , with  $m_\chi = 1 \text{ TeV}$  (left panels)  $m_\chi = 10 \text{ MeV}$  (right panels) and  $B = 0.5$ . Top row:  $n = 0$ , middle row:  $n = 1$ , bottom row:  $n = 2$ .

where after taking  $T_\star \rightarrow 0$  we recognise three regions of interest

$$\lim_{T_\star \rightarrow 0} T_\star \mathcal{F}_0(E_i, -|q_0|) = \begin{cases} \frac{|q_0| e^{-|q_0|/T_\star}}{1 - e^{-|q_0|/T_\star}}, & E_i > \varepsilon_{F,i} + |q_0| \\ \frac{(E_i - \varepsilon_{F,i}) e^{-|q_0|/T_\star}}{1 - e^{-|q_0|/T_\star}}, & \varepsilon_{F,i} + |q_0| > E_i > \varepsilon_{F,i} \\ 0, & \varepsilon_{F,i} > E_i \end{cases}, \quad (\text{A.62})$$

and we can write this as

$$\lim_{T_\star \rightarrow 0} T_\star \mathcal{F}_0(E_i, -|q_0|) = \frac{|q_0| e^{-|q_0|/T_\star}}{1 - e^{-|q_0|/T_\star}} h_0\left(\frac{\varepsilon_{F,i} - E_i}{q_0}\right). \quad (\text{A.63})$$

The response function for upscattering is then

$$S_{\text{up}}^-(q_0, q) = \frac{m_i^2 q_0}{\pi q} \frac{e^{-|q_0|/T_\star}}{e^{-|q_0|/T_\star} - 1} \left[ 1 - h_0\left(\frac{E_i^{t^-} - \varepsilon_{F,i}}{q_0}\right) \right] \quad (\text{A.64})$$

$$= \frac{m_i^2 q_0}{\pi q} \frac{e^{-|q_0|/T_\star}}{e^{-|q_0|/T_\star} - 1} g_0\left(\frac{\varepsilon_{F,i} - E_i^{t^-}}{q_0}\right), \quad (\text{A.65})$$

leading to the corresponding up-scattering rate being

$$\Gamma_{\text{up}}^-(E_\chi) = \int \frac{k'^2 d \cos \theta dk'}{64\pi^2 m_i^2 E_\chi E'_\chi} |\bar{\mathcal{M}}|^2 \Theta(E_\chi + |q_0| - m_\chi) \Theta(q_0) S_{\text{up}}^-(q_0, q) \quad (\text{A.66})$$

$$= \frac{(-1)^n \alpha}{128\pi^3 E_\chi k} \int_{-\infty}^0 dq_0 \frac{q_0 e^{q_0/T_\star}}{e^{q_0/T_\star} - 1} \int dt_E \frac{t_E^n}{\sqrt{t_E - |q_0|^2}} g_0\left(\frac{\varepsilon_{F,i} - E_i^{t^-}}{q_0}\right) \quad (\text{A.67})$$

where we have substituted  $|\bar{\mathcal{M}}|^2 = \alpha t^n$  as the matrix element. Typically, we expect to be in the regime where  $g_0 = 1$ , and so the differential up-scattering rate is related result for down-scattering through

$$\frac{d\Gamma_{\text{up}}^-}{dq_0} = \frac{e^{-|q_0|/T_\star}}{e^{-|q_0|/T_\star} - 1} \frac{d\Gamma_{\text{down}}^-}{dq_0} \quad (\text{A.68})$$

This result applies generally to all matrix elements, not just the ones  $\propto t^n$ . The result can be derived from the principle of detailed balance, and hence is true for all interactions we consider. To calculate the total interaction rate, the  $t_E$  integrations can be performed in the same manner as in the previous section, with the  $q_0$  integration bounds being  $(-\infty, 0)$ .

### A.3 Non-degenerate weak field limit

When setting up the centre of mass energy interval in Section 3.3, we have set the DM energy to 0 at infinity. This means that when taking the classical non-relativistic limit, the interaction rate would approach

$$\Omega^-(r) \rightarrow n_i(r)v_{\text{esc}}(r)\sigma, \quad (\text{A.69})$$

in the simple case of a constant cross-section. Taking Eq. 3.39, one can first strip out the Pauli blocking term  $(1 - f_{\text{FD}})$ , and then the integration in  $t$  and  $s$  can be performed analytically. Taking the limit  $u_i \rightarrow 0$ ,  $E_i = m_i/\sqrt{1 - u_i^2}$ , and then the weak field approximation  $B(r) \rightarrow 1 - v_{\text{esc}}^2(r)$ , for a constant cross-section  $\frac{d\sigma}{d\cos\theta_{\text{cm}}} = \frac{\sigma}{2}$ , we find

$$\Omega^-(r) \rightarrow m_i^2 \frac{\sigma}{2} \frac{2u_i v_{\text{esc}}(r) f_{\text{FD}}(E_i, r)}{\pi^2} dE_i \quad (\text{A.70})$$

$$= m_i^3 \frac{\sigma}{2} \frac{2u_i v_{\text{esc}}(r) f_{\text{FD}}(E_i, r)}{\pi^2} u_i du_i \quad (\text{A.71})$$

$$= m_i^3 \frac{\sigma}{2} \frac{v_{\text{esc}}(r) f_{\text{FD}}(E_i, r)}{2\pi^3} d^3 u_i \quad (\text{A.72})$$

$$= \frac{\sigma}{2} \frac{v_{\text{esc}}(r) f_{\text{FD}}(E_i, r)}{2\pi^3} d^3 p. \quad (\text{A.73})$$

Cases with  $\sigma \propto t^n$  give similar results. Recall that

$$\frac{2f_{\text{FD}}(E_i)}{(2\pi)^3} d^3 p, \quad (\text{A.74})$$

is the number density of neutron states. Then, following expression in 3.31 we substitute it with the classical number density  $n_i(r)$ , to obtain the expected classical limit given by Eq. A.69.

### A.4 Intermediate DM mass range

The interaction rate in Eq. 3.39 can be rewritten in terms of the DM momentum  $p_\chi$ , such that

$$\begin{aligned} \Omega^-(r) &= \frac{\zeta(r)}{32\pi^3} \int dt dE_i ds |\bar{M}|^2 \frac{E_i}{2s\beta(s) - \gamma^2(s)} \frac{1}{p_\chi} \frac{s}{\gamma(s)} \\ &\quad \times f_{\text{FD}}(E_i, r)(1 - f_{\text{FD}}(E'_i, r)), \end{aligned} \quad (\text{A.75})$$

where we have also used Eq. 3.51. We first consider the case where the squared matrix element depends only on  $t$ , i.e.  $|\bar{M}|^2 \propto t^n$ , we can straightforwardly perform the integral over  $t$ ,

$$\Omega^-(r) = \frac{\zeta(r)}{32\pi^3} \int dE_i ds \bar{g}(s) \frac{E_i \gamma(s)}{2s\beta(s) - \gamma^2(s)} \frac{1}{n+1} \frac{1}{p_\chi} \left( \frac{\gamma^2(s)}{s} \right)^n \times f_{\text{FD}}(E_i, r)(1 - f_{\text{FD}}(E'_i, r)). \quad (\text{A.76})$$

We now assume that either  $\mu \gg 1$  or  $\mu \ll 1$ . In both cases, the integration range for  $s$  shrinks to  $[s_0 - \delta s, s_0 + \delta s]$ , with  $\delta s \ll s_0$ , and the following simplifications can be made;

$$s_0 = m_i^2 + m_\chi^2 + 2 \frac{E_i m_\chi}{\sqrt{B(r)}} = m_i^2 + m_\chi^2 + 2 E_i E_\chi, \quad (\text{A.77})$$

$$\delta s = 2 \sqrt{\frac{1 - B(r)}{B(r)}} m_\chi \sqrt{E_i^2 - m_i^2} = 2 p_\chi \sqrt{E_i^2 - m_i^2}, \quad (\text{A.78})$$

$$\frac{\gamma(s)}{2s\beta(s) - \gamma^2(s)} \rightarrow \frac{\sqrt{1 - B(r)}}{2(m_i^2 + m_\chi^2)} = \frac{p_\chi}{2E_\chi(m_i^2 + m_\chi^2)}, \quad (\text{A.79})$$

$$\frac{\gamma^2(s)}{s} \rightarrow \frac{4(1 - B(r))m_\chi^2}{B(r)(1 + \mu^2)} = \frac{4p_\chi^2}{1 + \mu^2}. \quad (\text{A.80})$$

If  $g(s)$  is regular in  $s_0$ , we can estimate the integral in  $s$  to be  $2\delta s$ , approximating the integrand as being constant in that range, which gives

$$\Omega^-(r) \sim \zeta(r) \frac{1}{16\pi^3} \frac{\sqrt{E_\chi^2 - m_\chi^2}}{E_\chi(m_i^2 + m_\chi^2)} \frac{\left[ \frac{4(E_\chi^2 - m_\chi^2)}{1 + \mu^2} \right]^n}{n+1} \int dE_i E_i \sqrt{E_i^2 - m_i^2} \times f_{\text{FD}}(E_i, r)(1 - f_{\text{FD}}(E'_i, r)). \quad (\text{A.81})$$

To perform the integral in  $E_i$ , we have to potentially deal with Pauli blocking. However, for  $\mu \gg 1$ , Pauli blocking is not effective and we can drop the  $1 - f_{\text{FD}}$  term to obtain

$$\int_{m_i}^{m_i + \varepsilon_{F,i}(r)} dE_i E_i \sqrt{E_i^2 - m_i^2} f_{\text{FD}}(E_i, r) = \frac{[\varepsilon_{F,i}(r)(2m_i + \varepsilon_{F,i}(r))]^{3/2}}{3} \quad (\text{A.82})$$

$$= \pi^2 n_{\text{free}}(r). \quad (\text{A.83})$$

This, together with  $\zeta(r)$ , result in an overall factor of  $\pi^2 n_i(r)$ , leaving

$$\Omega^-(r) \sim \frac{n_i(r)}{16\pi} \frac{\sqrt{E_\chi^2 - m_\chi^2}}{m_\chi^2 E_\chi} \frac{1}{n+1} \left[ \frac{4(1 - B(r))m_\chi^2}{B(r)(1 + \mu^2)} \right]^n, \quad (\text{A.84})$$

and the capture rate reads,

$$C \sim \frac{1}{4v_\star} \frac{\rho_\chi}{m_\chi^3} \text{Erf} \left( \sqrt{\frac{3}{2}} \frac{v_\star}{v_d} \right) \int_0^{R_\star} r^2 dr n_i(r) \frac{1 - B(r)}{B(r)} \frac{1}{n+1} \times \left[ \frac{4(1 - B(r))m_\chi^2}{B(r)(1 + \mu^2)} \right]^n. \quad (\text{A.85})$$

We can now rewrite these expressions in terms of the cross-section which has been averaged over  $s$ ,

$$\langle \sigma(r) \rangle = \left\langle \int dt \frac{d\sigma}{dt} \right\rangle_s \quad (\text{A.86})$$

$$= \frac{1}{2\delta s} \int_{s_0 - \delta s}^{s_0 + \delta s} ds \int dt \frac{d\sigma}{dt} \quad (\text{A.87})$$

$$= \frac{1}{64\pi m_i^2 m_\chi^2} \frac{B(r)}{(1 - B(r))} \int dt t^n \quad (\text{A.88})$$

$$= \frac{1}{64\pi m_i^2 m_\chi^2} \frac{B(r)}{(1 - B(r))} \frac{1}{(n+1)} \left[ \frac{4(1 - B(r))m_\chi^2}{B(r)(1 + \mu^2)} \right]^{n+1} \quad (\text{A.89})$$

$$= \frac{1}{16\pi (m_i^2 + m_\chi^2)} \frac{1}{(n+1)} \left[ \frac{4(1 - B(r))m_\chi^2}{B(r)(1 + \mu^2)} \right]^n, \quad (\text{A.90})$$

which leads to,

$$\Omega^-(r) \sim n_i(r) \langle \sigma(r) \rangle \frac{\sqrt{E_\chi^2 - m_\chi^2}}{E_\chi}, \quad (\text{A.91})$$

$$C \sim \frac{4\pi}{v_\star} \frac{\rho_\chi}{m_\chi} \text{Erf} \left( \sqrt{\frac{3}{2}} \frac{v_\star}{v_d} \right) \int_0^{R_\star} r^2 dr n_i(r) \frac{1 - B(r)}{B(r)} \langle \sigma(r) \rangle. \quad (\text{A.92})$$

From Eq. A.92, we can identify the typical  $1/m_\chi$  scaling of the capture rate. This equation also looks very similar to the non-relativistic case, with  $1 - B(r)$  playing the role of the escape velocity,  $v_{\text{esc}}^2(r)$ , and  $1/B(r)$  being a relativistic correction.

Turning to the case of  $s$ -dependent matrix elements,  $|\bar{\mathcal{M}}|^2 = g(s)t^n$  for  $\bar{g}$  some function of  $s$ , the result is fairly similar. The main difference is that we must keep all terms in  $m_i$  and  $m_\chi$ , leading to the new substitutions

$$\frac{\gamma(s)}{s^2 - [m_i^2 - m_\chi^2]^2} \sim \frac{\sqrt{1 - B(r)}}{2 \left( m_i^2 + m_\chi^2 + 2m_i m_\chi / \sqrt{B(r)} \right)}, \quad (\text{A.93})$$

$$\frac{\gamma^2(s)}{s} \rightarrow \frac{4(1 - B(r))m_\chi^2}{B(r)(1 + \mu^2) + 2\sqrt{B(r)}\mu}. \quad (\text{A.94})$$

Now when we take the limit as  $\varepsilon_{F,n} \rightarrow 0$ , the integrand over  $s$  can be approximated as a  $\delta$ -function, resulting in  $s$  being fixed to the value of  $s_0$ . As such, we no longer need to average the cross-section over  $s$ . The results are

$$\Omega^-(r) \sim \frac{n_i(r)}{16\pi} \frac{\sqrt{E_\chi^2 - m_\chi^2}}{E_\chi (m_i^2 + m_\chi^2 + 2m_i E_\chi)} \frac{\bar{g}(s_0)}{n+1} \left[ \frac{4(1-B(r))m_\chi^2}{B(r)(1+\mu^2) + 2\sqrt{B(r)}\mu} \right]^n. \quad (\text{A.95})$$

$$C \sim C_{\text{approx},s} = \frac{4\pi}{v_\star} \frac{\rho_\chi}{m_\chi} \text{Erf} \left( \sqrt{\frac{3}{2}} \frac{v_\star}{v_d} \right) \int_0^{R_\star} r^2 dr n_i(r) \frac{1-B(r)}{B(r)} \sigma(r), \quad (\text{A.96})$$

$$\sigma(r) = \int dt \frac{d\sigma}{dt} = \frac{1}{16\pi (m_i^2 m_\chi^2 + 2m_i m_\chi / \sqrt{B(r)})} \frac{\bar{g}(s_0)}{(n+1)} \times \left[ \frac{4(1-B(r))m_\chi^2}{B(r)(1+\mu^2) + 2\sqrt{B(r)}\mu} \right]^n. \quad (\text{A.97})$$

## A.5 Kinematic phase space for DM-electron scattering

When deriving the interaction rate in the context of DM capture in NSs, we assumed that all the target phase space was available to scatter with DM. This is not necessarily true if the target is highly degenerate or if gravity is not particularly strong, like in NSs. In fact, for the scattering to occur, both the DM and target momenta should be in the inbound direction in the centre of mass frame. This is true in the whole phase space only when the following condition is satisfied

$$\frac{1}{\sqrt{B(r)}} > \frac{\varepsilon_{F,e}}{m_e}. \quad (\text{A.98})$$

To clarify this point, we first derive this constraint using non-relativistic kinematics. The DM particle of mass  $m_\chi$  has an initial speed

$$v_{\text{esc}} = \sqrt{1 - B}, \quad (\text{A.99})$$

while the target has a mass  $m_e$  and an energy

$$E_e = m_e + b\varepsilon_{F,e} = m_e \left( 1 + b \frac{\varepsilon_{F,e}}{m_e} \right), \quad b \in [0, 1]. \quad (\text{A.100})$$

Using non-relativistic kinematics, the speed of the target is

$$v_e = \sqrt{2b \frac{\varepsilon_{F,e}}{m_e}}. \quad (\text{A.101})$$

The centre of mass velocity is defined as

$$\vec{v}_{com} = \frac{1}{m_\chi + m_e} (m_\chi \vec{v}_{esc} + m_e \vec{v}_e), \quad (\text{A.102})$$

so the DM speed in the CoM frame is  $\vec{v}'_\chi = \vec{v}_{esc} - \vec{v}_{com}$ . To ensure that the DM and the target are not moving away from each other, the following condition should hold,  $\vec{v}'_\chi \cdot \vec{v}_{esc} > 0$ , i.e., the component of the DM velocity in the CoM frame is always parallel to the initial speed in the star frame. This condition leads to

$$\cos \theta < \sqrt{\frac{1-B}{2b(\varepsilon_{F,e}/m_e)}}, \quad (\text{A.103})$$

where  $\theta$  is the angle between the DM and the target speed in the star frame. If  $\varepsilon_{F,e}/m_e \gg 1-B$ , the condition reduces to

$$\cos \theta < 0, \quad (\text{A.104})$$

meaning that the collision is head-on only.

Repeating the same exercise with relativistic kinematics, the variable whose parameter space is modified by the above mentioned condition is the centre of mass energy  $s$ ,

$$s = m_\chi^2 + m_e^2 + \frac{2m_e m_\chi}{\sqrt{B}} \left( 1 + b \frac{\varepsilon_{F,e}}{m_e} - a \sqrt{1-B} \sqrt{2b \frac{\varepsilon_{F,e}}{m_e} + b^2 \frac{\varepsilon_{F,e}^2}{m_e^2}} \right), \quad a \in [-1, 1], \quad (\text{A.105})$$

and the new condition becomes

$$a = \frac{s_{\max} + s_{\min} - 2s}{s_{\max} - s_{\min}} < \left( 1 + b \frac{\varepsilon_{F,e}}{m_e} \right) \sqrt{\frac{1-B}{2b \frac{\varepsilon_{F,e}}{m_e} + b^2 \frac{\varepsilon_{F,e}^2}{m_e^2}}} = E_e \sqrt{\frac{1-B}{E_e^2 - m_e^2}}. \quad (\text{A.106})$$

With the exception of the heaviest WDs, we have  $\varepsilon_{F,e}/m_e \lesssim 1$ . Then, with  $1-B \sim 10^{-3}$ , we can check that expanding Eq. A.106 leads to Eq. A.103 and that  $a \lesssim 0$ . This implies that approximately half of the phase space is not available for scattering. (For electrons in NSs we instead have  $\varepsilon_{F,e}/m_e \gg 1$ , and hence this does not occur.)

Taking the ultra-relativistic limit for electrons, Eq. A.106 reduces to

$$a < \sqrt{1-B}. \quad (\text{A.107})$$

This restriction of the available phase space results in variations of the order of  $\mathcal{O}(10\%)$  for both the interaction and capture rates.

## A.6 Interaction Rate for Low Energies

Need to consider the case where  $T_\chi = E_\chi - m_\chi < \mu_F$ , with  $0 < q_0 < T_\chi < \varepsilon_{F,i}$ . Then the  $t_E$  integration limits follow the hierarchy;  $t_{\mu^+}^+ \sim t_{\mu^-}^+ \geq t_{\mu^-}^- \sim t_{\mu^+}^- \gtrsim 0$ , and  $t_{\mu^-}^+ \gg t_E^+ \geq t_E^- \gg t_{\mu^-}^-$ . Then the only term in A.54 that remains is the first term, and only the  $i = j = 1$  term contributes, leaving

$$\Gamma^-(E_\chi) = \sum_{n,m} \frac{(-1)^n \alpha_{n,m}}{128\pi^3 E_\chi k} \int_0^{E_\chi - m_\chi} dq_0 \int_{t_E^-}^{t_E^+} dt_E f_1^{(m,n)}(t_E) \quad (\text{A.108})$$

At first order in  $q_0$  and  $K_\chi$ , we have the following approximations

$$E_\chi \approx m_\chi \quad (\text{A.109})$$

$$k \approx \sqrt{2m_\chi T_\chi} \quad (\text{A.110})$$

$$t_E^\pm \approx 4m_\chi T_\chi \left[ 1 - \frac{q_0}{2K_\chi} \pm \sqrt{1 - \frac{q_0}{K_\chi}} \right] \quad (\text{A.111})$$

$$\Gamma^- \approx \sum_{n,m} \frac{(-1)^n \alpha_{n,m}}{128\sqrt{2}\pi^3 m_\chi^{3/2} K_\chi^{1/2}} \int_0^{K_\chi} dq_0 \int_{t_E^-}^{t_E^+} dt_E f_1^{(m,n)}(t_E) \quad (\text{A.112})$$

For single term matrix elements such that  $|\bar{\mathcal{M}}|^2 = \alpha_{n,m}(-t)^n s^m$ , the corresponding  $\Gamma_{n,m}^-$  are

$$\Gamma_{0,0}^- = \frac{\alpha_{0,0}}{120\pi^3 m_\chi} K_\chi^2 \quad (\text{A.113})$$

$$\Gamma_{1,0}^- = \frac{2\alpha_{1,0}}{105\pi^3} K_\chi^3 \quad (\text{A.114})$$

$$\Gamma_{2,0}^- = \frac{4\alpha_{2,0} m_\chi}{63\pi^3} K_\chi^4 \quad (\text{A.115})$$

$$\Gamma_{0,1}^- = \frac{\alpha_{0,1}((m_i + m_\chi)^2 + 2m_\chi \varepsilon_{F,i})}{120\pi^3} K_\chi^2 \quad (\text{A.116})$$

$$\Gamma_{1,1}^- = \frac{2\alpha_{1,1}((m_i + m_\chi)^2 + 2m_\chi \varepsilon_{F,i})}{105\pi^3} K_\chi^3 \quad (\text{A.117})$$

$$\Gamma_{0,2}^- = \frac{\alpha_{0,2}((m_i + m_\chi)^2 + 2m_\chi \varepsilon_{F,i})^2}{120\pi^3} K_\chi^2 \quad (\text{A.118})$$

The  $\alpha_{n,m}$  can be obtained at some reference point, taken to be the surface of the NS, from the differential cross-section,

$$\frac{d\sigma}{d \cos \theta_{\text{cm}}} = \frac{\alpha_{n,m}(-t)^n s^m}{32\pi(m_i + m_\chi)^2} \quad (\text{A.119})$$

which gives

$$\sigma_{0,0} = \frac{\alpha_{0,0}}{16\pi(m_i + m_\chi)^2} \quad (\text{A.120})$$

$$\sigma_{1,0} = \frac{\alpha_{1,0}}{32\pi(m_i + m_\chi)^2} t_{\max} \quad (\text{A.121})$$

$$\sigma_{2,0} = \frac{1}{3} \frac{\alpha_{2,0}}{16\pi(m_i + m_\chi)^2} t_{\max}^2 \quad (\text{A.122})$$

$$\sigma_{0,1} = \frac{\alpha_{0,1}}{16\pi(m_i + m_\chi)^2} s \quad (\text{A.123})$$

$$\sigma_{1,1} = \frac{\alpha_{1,1}}{32\pi(m_i + m_\chi)^2} t_{\max} s \quad (\text{A.124})$$

$$\sigma_{0,2} = \frac{\alpha_{0,2}}{16\pi(m_i + m_\chi)^2} s^2 \quad (\text{A.125})$$

where I have used

$$t = -\frac{t_{\max}}{2}(1 - \cos \theta_{\text{cm}}) \quad (\text{A.126})$$

$$t_{\max} \sim \frac{4m_i^2 m_\chi^2}{(m_i^2 + m_\chi^2)} \frac{1 - B(R_\star)}{B(R_\star)} \quad (\text{A.127})$$

$$s \sim m_i^2 + m_\chi^2 + \frac{2m_\chi(m_i + \varepsilon_{F,i})}{\sqrt{B(R_\star)}} \quad (\text{A.128})$$

$$\sim (m_i + m_\chi)^2 \quad (\text{A.129})$$

Again introducing the correction

$$\zeta = \frac{n_i}{n_{\text{free}}} \sim \frac{3\pi^2}{(2m_i \varepsilon_{F,i})^{3/2}} n_i \quad (\text{A.130})$$

Then the interaction rates can be expressed with respect to the surface of the star

as

$$\Gamma_{0,0}^-(K_\chi) = \frac{\sqrt{2}}{10} \frac{(1+\mu)^2}{\mu} \frac{m_i}{(m_i \varepsilon_{F,i})^{3/2}} \sigma_{surf} n_i K_\chi^2 \quad (\text{A.131})$$

$$\Gamma_{1,0}^-(K_\chi) = \frac{4\sqrt{2}}{35} \frac{(1+\mu)^2(1+\mu^2)}{\mu^2} \frac{1}{(m_i \varepsilon_{F,i})^{3/2}} \frac{B(R_\star)}{(1-B(R_\star))} \sigma_{surf} n_i K_\chi^3 \quad (\text{A.132})$$

$$\Gamma_{2,0}^-(K_\chi) = \frac{\sqrt{2}}{7} \frac{(1+\mu)^2(1+\mu^2)^2}{\mu^3} \frac{1}{m_i(m_i \varepsilon_{F,i})^{3/2}} \left( \frac{B(R_\star)}{(1-B(R_\star))} \right)^2 \sigma_{surf} n_i K_\chi^4 \quad (\text{A.133})$$

$$\Gamma_{0,1}^-(K_\chi) = \frac{\sqrt{2}}{10} \frac{(m_i(1+\mu)^2 + 2\mu\varepsilon_{F,i})}{\mu(m_i \varepsilon_{F,i})^{3/2}} \sigma_{surf} n_i K_\chi^2 \quad (\text{A.134})$$

$$\Gamma_{1,1}^-(K_\chi) = \frac{4\sqrt{2}}{35} \frac{(m_i(1+\mu)^2 + 2\mu\varepsilon_{F,i})(1+\mu^2)}{\mu^2 m_i(m_i \varepsilon_{F,i})^{3/2}} \frac{B(R_\star)}{(1-B(R_\star))} \sigma_{surf} n_i K_\chi^3 \quad (\text{A.135})$$

$$\Gamma_{0,2}^-(K_\chi) = \frac{\sqrt{2}}{10} \frac{(m_i(\mu+1)^2 + 2\mu\varepsilon_{F,i})^2}{\mu(\mu+1)^2 m_i(m_i \varepsilon_{F,i})^{3/2}} \sigma_{surf} n_i K_\chi^2 \quad (\text{A.136})$$

The average energy loss per collision is given by

$$\langle \Delta T \rangle = \frac{1}{\Gamma^-} \int_0^{K_\chi} dq_0 q_0 \frac{d\Gamma^-}{dq_0} \quad (\text{A.137})$$

which gives the results

$$\langle \Delta T^{0,0} \rangle = \frac{4}{7} K_\chi \sim \langle \Delta T^{0,1} \rangle \sim \langle \Delta T^{0,2} \rangle \quad (\text{A.138})$$

$$\langle \Delta T^{1,0} \rangle = \frac{5}{9} K_\chi \sim \langle \Delta T^{1,1} \rangle \quad (\text{A.139})$$

$$\langle \Delta T^{2,0} \rangle = \frac{28}{55} K_\chi \quad (\text{A.140})$$

The DM will reach thermal equilibrium with the targets when  $K_\chi = T_\star$ . There are two stages to this process; one where the interactions are not affected by Pauli blocking which takes  $N_1$  collisions, and the next  $N_2$  collisions where Pauli blocking is in effect. The time it takes for thermalisation to occur is given by the sum of the average times between collisions

$$t_{\text{therm}} = \sum_{n=0}^{N_2} \frac{1}{\Gamma^-(T_n)} \sim \sum_{n=N_1}^{N_2} \frac{1}{\Gamma^-(T_n)} \quad (\text{A.141})$$

where  $T_n$  is the DM kinetic energy after  $n$  collisions. If Pauli blocking is in effect for the entire process, then  $T_n$  is related to the initial kinetic energy,  $T_0$  through

$$T_n = T_0 \left( 1 - \frac{\Delta T}{T} \right)^n. \quad (\text{A.142})$$

This result implies the following relation;

$$\frac{T_N}{T_0} = \frac{T_{eq}}{T_0} = \left(1 - \frac{\Delta T}{T}\right)^N \quad (\text{A.143})$$

Then for interaction rates which follow  $\Gamma^- \propto (K_\chi)^p$ , we have that

$$t_{\text{therm}} \propto \sum_{n=N_1}^{N_2} (T_n)^{-p} \quad (\text{A.144})$$

$$= \frac{1}{T_{N_1}^p} \sum_{n=N_1}^{N_2} \left( \left(1 - \frac{\Delta T}{T}\right)^{-p} \right)^n \quad (\text{A.145})$$

$$= \frac{1}{T_{N_1}^p} \frac{(1 - \Delta T/T)^{p(1-N_1)} - (1 - \Delta T/T)^{-pN_2}}{-1 + (1 - \Delta T/T)^p} \quad (\text{A.146})$$

$$\sim \frac{1}{T_{N_1}^p} \frac{(1 - \Delta T/T)^{-pN_2}}{1 - (1 - \Delta T/T)^p} \quad \text{for } N_2 > N_1 \quad (\text{A.147})$$

$$= \frac{1}{T_{N_1}^p} \left( \frac{T_{eq}}{T_{N_1}} \right)^{-p} \frac{1}{1 - (1 - \Delta T/T)^p} \quad (\text{A.148})$$

$$= \frac{1}{T_{eq}^p} \frac{1}{1 - (1 - \Delta T/T)^p} \quad (\text{A.149})$$

# B

## Hadronic matrix elements for scattering operators

This appendix provides the hadronic matrix elements required for computing the dark matter-baryon couplings given in Eqs. ??-??, for both nucleons and hyperons.

### B.1 Nucleons

The values of the hadronic matrix elements for neutrons and protons used in this paper are listed in Table ???. The values of  $\Delta_q^{(p)}$  (and similarly for  $\delta_q^{(p)}$ ) are obtained using isospin symmetry:

$$\Delta_u^N = \Delta_d^{N^\star}, \quad \Delta_s^N = \Delta_s^{N^\star}, \quad (\text{B.1})$$

where  $N^\star$  is the nucleon obtained interchanging  $u \iff d$  quarks.

$q$	$f_{T_q}^{(n)}$ [247]	$f_{T_q}^{(p)}$ [247]	$\Delta_q^{(n)}$	$\delta_q^{(n)}$ [247]
$u$	0.0110	0.0153	-0.319 [248]	-0.230
$d$	0.0273	0.0191	0.787 [248]	0.840
$s$	0.0447	0.0447	-0.040 [249]	-0.046

**Table B.1:** Hadronic matrix elements for neutrons and protons.

## B.2 Hyperons

To calculate the  $f_{T_q}^{(\mathcal{B})}$  couplings for hyperons, we use the baryonic sigma terms from ref. [250], listed in Table B.2, in the following way

$$f_{T_{u,d}}^{(\mathcal{B})} = \frac{\sigma_{l\mathcal{B}}}{m_{\mathcal{B}}} \frac{m_{u,d}}{m_u + m_d}, \quad (\text{B.2})$$

$$f_{T_s}^{(\mathcal{B})} = \frac{\sigma_s}{m_{\mathcal{B}}}, \quad (\text{B.3})$$

where the first relation assumes

$$\frac{\sigma_u^{\mathcal{B}}}{m_u} = \frac{\sigma_d^{\mathcal{B}}}{m_d}. \quad (\text{B.4})$$

In addition, we assume

$$\sigma_u^{\mathcal{B}} = \sigma_d^{\mathcal{B}*}, \quad \sigma_s^{\mathcal{B}} = \sigma_s^{\mathcal{B}*}. \quad (\text{B.5})$$

For the dimension 6 operators where  $c_q \propto m_q$ , the nucleon couplings depend only on the following sum of the  $f_{T_q}^{(\mathcal{B})}$  values

$$\sum_{q=u,d,s} f_{T_q}^{(\mathcal{B})} = \frac{\sigma_{l\mathcal{B}} + \sigma_s}{m_{\mathcal{B}}}, \quad (\text{B.6})$$

and hence exact values for the individual  $f_{T_q}^{(\mathcal{B})}$  are unnecessary. The axial vector [250, 251] and tensor [252] couplings are listed in Table B.2.

$\mathcal{B}$	$\sigma_{l\mathcal{B}}$ (MeV)	$\sigma_s$ (MeV)	$\Delta_u$	$\Delta_d$	$\Delta_s$	$\delta_u$	$\delta_d$	$\delta_s$
$\Lambda^0$	$32 \pm 4$	$176 \pm 19$	0	0	0.59	0	0	0.47
$\Xi^0$	$13 \pm 10$	$334 \pm 21$	-0.38	0	1.03	-0.22	0	0.9
$\Xi^-$	$13 \pm 10$	$334 \pm 21$	0	-0.38	1.03	0	-0.22	0.9

**Table B.2:** Sigma commutators for scalar interactions for each hyperon  $\mathcal{B}$  (first and second column). Spin matrix elements for axial vector [250, 251] and tensor interactions are given in the remaining columns. Tensor couplings for  $\Xi$  are taken from ref. [252], while those for  $\Lambda^0$  are our estimates.